博士論文（要約）

Theoretical study on topological edge states unique to nonlinear systems

（非線形系に特有なトポロジカル端状態の理論的研究）

曽根 和樹

Abstract

Since the discovery of the quantum Hall effect, topology of band structures has attracted much interest in condensed matter physics. One of the most important concepts in topological materials is the bulk-boundary correspondence that guarantees one-to-one correspondence between bulk topological invariants and the existence and absence of edge-localized modes. Since the topological invariants are unchanged under the adiabatic deformation of Hamiltonians, associated edge modes are also robust against disorder, which is of applicational interest in topological materials. Recent studies have also revealed the existence of topological edge modes in various media, including fluids, photonic metamaterials, biological systems, and ultracold atoms.

While the conventional studies of topological edge modes are based on the band structure of linear systems, nonlinear dynamics is ubiquitous in nature. Recent studies have also found edge states in such nonlinear systems. In particular, they have shown that the interplay between topological physics and nonlinear physics can lead to nonlinear modification of edge modes, such as topological solitons. However, most of the previous studies have focused on conservative systems, and thus the role of topology in dissipative nonlinear systems has been largely unexplored. Another problem is that there are only a few studies on the topological invariants that characterize the topology of nonlinear systems, and thus the bulk-boundary correspondence in nonlinear systems has been unelucidated.

In this thesis, we reveal topological edge modes and their bulk-boundary correspondence unique to nonlinear systems. Specifically, we investigate topological edge modes in both conservative and dissipative systems and show that edge modes can ubiquitously appear in nonlinear systems. We also propose the topological invariants that characterize nonlinear topology and discuss in what range of strength of nonlinearity the bulk-boundary correspondence is guaranteed in nonlinear systems.

In the first part, we investigate the role of topology in nonlinear oscillators and find the topological synchronized state where the edge oscillators are synchronized, while the bulk ones are chaotic. This is a nonlinear counterpart of topological insulators, which are insulating in the bulk and metallic at the edge. One can realize such topological synchronized states by introducing topological linear couplings to periodically aligned nonlinear oscillators. We construct and analyze toy models and numerically demonstrate the existence of the topological synchronization. Since the toy models are constructed from different topological linear couplings, such as those of an exceptional edge mode, a non-Hermitian Chern insulator, and a Hermitian topological insulator, the topological synchronization is ubiquitous in nonlinear oscillators with topological linear couplings. To show the chaos in the bulk oscillators, we also conduct the Lyapunov analysis of the models and find the edge-localized Lyapunov vectors, which resemble topological edge modes in linear systems. The topological synchronized state is also useful to robustly control the synchronization of oscillators. Specifically, we demonstrate that one can arrange synchronized oscillators in a desired pattern by using the topological synchronization. We also propose the electrical-circuit realization of the topological synchronized state. These results clarify the existence of topological edge modes in dissipative nonlinear systems and thus indicate the ubiquity of topological edge modes in nature.

In the second part, we propose a nonlinear Chern number that characterizes the topology of two-dimensional nonlinear systems and analyze its bulk-boundary correspondence. To define the nonlinear Chern number, we consider the extension of an eigenvalue problem to nonlinear

systems. Then, assuming the plane-wave ansatz that we name the Bloch ansatz, we derive the wavenumber-space description of the eigenvalue problem and construct an analogy to a band structure. Finally, from the nonlinear eigenvectors, we construct the nonlinear extension of the Chern number. To discuss the bulk-boundary correspondence of the nonlinear Chern number, we analyze a minimal model of a nonlinear Chern insulator. The bulk-boundary correspondence is shown both numerically and analytically in weakly nonlinear systems. Surprisingly, we find that stronger nonlinear effects induce anti-localized zero modes, which have no counterparts in linear systems. The bulk-boundary correspondence under stronger nonlinearity is specified as the nonzero topological invariant indicates the existence of edge-localized gapless modes, while the zero topological invariant indicates the absence of gapless modes or the existence of anti-localized zero modes. We analytically show such bulk-boundary correspondence in the continuous limit of the minimal model and numerically confirm the bulk-boundary correspondence in the finite lattice system. It is noteworthy that the nonlinear Chern number depends on the amplitude of the Bloch wave and thus the existence and absence of associated localized modes can be tuned by the amplitude, which is termed the nonlinearity-induced topological phase transition. Therefore, the nonlinear Chern number describes inherently nonlinear topological phases.

In the third part, we reveal the transition from topological edge modes to chaotic zero modes in nonlinear topological insulators. Such transition to chaos can be a mechanism of the breakdown of the bulk-boundary correspondence under strong nonlinearity. Therefore, the result provides the guiding principle to study nonlinear topology by clarifying the limitation of the strength of nonlinearity where the bulk-boundary correspondence is valid in the sense discussed in the second part. Specifically, we analyze a minimal model of one-dimensional nonlinear topological insulators and derive the dynamical system describing the spatial distribution of its zero modes. Then, we show that the dynamical system exhibits the period-doubling bifurcation to chaos. The bifurcation point provides the upper bound of the parameter where the bulk-boundary correspondence holds. We also propose the meaning of the absolute value of a nonlinear topological invariant; it corresponds to the dimension of the stable manifold of the dynamical system describing the spatial distribution of zero modes. We show such correspondence in an extended model of one-dimensional nonlinear topological insulators whose topological invariant can be two or more depending on the parameter. Even in such higher-invariant cases, the bifurcation to chaos can occur and induce the breakdown of the bulk-boundary correspondence. Therefore, the bifurcation to chaos can be a ubiquitous mechanism of the breakdown of the bulk-boundary correspondence in nonlinear topological insulators.

These results clarify the existence of topological edge modes in a variety of nonlinear systems and the bulk-boundary correspondence and its breakdown. Since the technique used in our study can be applied to other dimensions and symmetries, our proposals should form the basis to study the role of topology and the bulk-boundary correspondence in a broad range of nonlinear systems.

List of publication

This thesis is based on the following papers:

1. Kazuki Sone, Yuto Ashida, and Takahiro Sagawa, "Topological synchronization of coupled nonlinear oscillators" Physical Review Research **4,** 023211 (2022).

2. Kazuki Sone, Motohiko Ezawa, Yuto Ashida, Nobuyuki Yoshioka, and Takahiro Sagawa, "Nonlinearity-induced topological phase transition characterized by the nonlinear Chern number" arXiv:2307.16827 (2023).

3. Kazuki Sone, Motohiko Ezawa, Zongping Gong, Taro Sawada, Nobuyuki Yoshioka, and Takahiro Sagawa "Transition from Topological to Chaos in the Nonlinear Su-Schrieffer-Heeger Model" in preparation.

The Appendix A is based on the following paper:

4. Kazuki Sone, Yuto Ashida, and Takahiro Sagawa, "Exceptional mode topological surface laser" Physical Review B **105,** 235426 (2022).

I have also published the following papers which are not directly related to this thesis:

5. Kazuki Sone and Yuto Ashida, "Anomalous Topological Active Matter" Physical Review Letters **123,** 205502 (2019).

6. Kazuki Sone, Yuto Ashida, and Takahiro Sagawa, "Exceptional non-Hermitian topological edge mode and its application to active matter" Nature Communications **11,** 5745 (2020).

7. Taro Sawada, Kazuki Sone, Ryusuke Hamazaki, Yuto Ashida, and Takahiro Sagawa, "Role of Topology in Relaxation of One-dimensional Stochastic Processes" Physical Review Letters **132,** 046602 (2024).

Contents

Chapter 1

Introduction

1.1 Overall introduction of this thesis

Topology is a field of mathematics that discusses the geometrical properties unchanged under continuous deformations. A typical example of the topological properties of manifolds is a genus, i.e., the number of holes. Since a genus is a topological invariant that is unchanged under continuous deformations, one cannot transform a donut into a ball by continuous deformations of the manifold. The notion of topology is also of practical interest in recent studies of condensed matter physics because of the discovery of topological materials [1–3]. In topological materials, we consider the topology of band structures, which are defined in the wavenumber space. Then, the band structure is characterized by topological invariants such as the Chern number calculated from the associated eigenvectors. The key principle of topological materials is the bulk-boundary correspondence which guarantees one-to-one correspondence between nonzero topological invariants and the existence of gapless boundary modes. Since the topological invariants are unchanged under the adiabatic deformations that do not close band gaps, topological boundary modes are also robust against disorders, which leads to unique functionalities of topological materials such as backscattering-free current. While the pioneering works of band topology [4,5] investigated the quantum Hall effect in two-dimensional semiconductors under the broken time-reversal symmetry, topological boundary modes can appear in various setups including three-dimensional systems [6] and time-reversal symmetric systems [7,8].

While conventional studies on topology have focused on the electronic band structures, one can make analogies between the dispersion relations of classical and quantum systems and thus can discuss the topological properties in a wider range of systems. For example, recent studies have revealed the existence of topological edge modes in photonics [9–11], fluid [12,13], ultracold atoms [14,15], electrical circuits [16,17], and mechanical lattices [18–20]. Unlike the conventional Schrödinger equation, the general linear dynamics can be described by the non-Hermitian Hamiltonians [21] in classical and open quantum systems. As a direct result of the complex eigenvalues of the non-Hermitian Hamiltonians, one can realize the amplification of edge modes, which can be utilized as topological lasers [22,23]. Furthermore, the complex eigenvalues enrich the topological phases of non-Hermitian Hamiltonians, which is known as the point-gap topology [24]. Another non-Hermitian topological feature is the existence of exceptional points [25,26], and they can even protect the gapless edge modes in a different way from the conventional topological insulators [27].

On another front, nonlinear dynamics play important roles in various fields of science. A typical example of a nonlinear system is a nonlinear oscillator [235, 249], which oscillates in the balance of the injection and dissipation of energy. The collective motion of such nonlinear oscillators that is termed synchronization plays crucial roles in, e.g., biology [30–33] and engineering [34–36]. Another example of nonlinear dynamics is found in photonics, where the Kerr nonlinearity enriches the behaviors of photonic metamaterials [37–39]. The self-focusing effect by the Kerr nonlinearity can induce solitary waves of light, which cannot spontaneously appear in linear systems. The nonlinearity is also found in quantum bosonic systems by considering the mean-field theory [40,41].

Among nonlinear phenomena, chaos is one of the most important concepts in nonlinear systems. The defining feature of chaos is the sensitivity to the initial condition [249]. Such sensitivity is measured by so-called Lyapunov exponents, and by numerically calculating them various studies have investigated chaos in nonlinear dynamical systems. Chaos can be found from small to large systems. If we consider discrete dynamical systems, even one-dimensional nonlinear systems can exhibit chaos, which is exemplified by the logistic map [42]. On the other hand, chaos can appear in the dynamics of, e.g., atmosphere, and thus studies of chaos are of both mathematical and practical interest.

As the counterparts of topological materials are found in classical and non-Hermitian systems, there have been attempts to extend the notion of topology to nonlinear systems [38, 39, 43]. Previous studies have revealed nontrivial interplays between topological edge modes and nonlinear phenomena, such as topological edge solitons [44, 45]. Furthermore, the nonlinearity can induce the amplitude dependence of topological phases, i.e., the nonlinearity-induced topological phase transitions [46–48]. However, despite these discoveries of nonlinear topological edge modes, the bulk-boundary correspondence in nonlinear systems is unelucidated. In addition, the role of topology in dissipative nonlinear systems [49] is much less understood than that in conservative nonlinear systems. In particular, interplays between topological edge modes and nonlinear phenomena such as synchronization and chaos have been largely unexplored.

In this thesis, we first explore the role of topology in nonlinear oscillators, which are typical dissipative nonlinear systems. We here find the topological synchronized state, where the edge oscillators are synchronized and the bulk oscillators are desynchronized. One can realize such topological synchronization by introducing topological linear couplings to nonlinear oscillators. We also conduct the Lyapunov analysis on the models of the topological synchronized state and reveal the chaos of the bulk oscillators and the existence of edge-localized Lyapunov vectors. We also propose applications such as on-demand pattern designing. These results reveal the nontrivial connection between the physics of topological materials and synchronization and chaos.

We next investigate the bulk-boundary correspondence in nonlinear systems. Specifically, we propose the extension of topological invariants via the nonlinear eigenvalue problem [47, 48]. By analyzing the minimal model of nonlinear topological insulators, we reveal the bulk-boundary correspondence of such nonlinear topological invariants under moderate nonlinearity. In particular, we can analytically show the bulk-boundary correspondence in weakly nonlinear or continuum systems. Meanwhile, strong nonlinearity can alter the bulk-boundary correspondence in nonlinear systems. In fact, by analyzing zero modes in one-dimensional nonlinear systems, we find that strong nonlinearity can induce the transition from topological edge modes to chaotic zero modes and thus can break the bulk-boundary correspondence. We also discuss the bulk-boundary correspondence between the absolute values of the topological invariants and the dimension of the stable manifold. Such bulk-boundary correspondence can also be broken by the chaos transition. These findings should provide the guiding principle to investigate the bulk-boundary correspondence in nonlinear systems and thus can lead to a complete understanding of the nonlinear topology in the future.

1.2 Structure of this thesis

This thesis is organized as follows. In Chapters 2 and 3, we will review the related studies and basic concepts in topological insulators and nonlinear physics. Specifically, in Chapter 2, we will introduce the history of studies on topological materials and recent extensions to nonequilibrium systems and classical systems. We will also discuss the topological properties in minimal models of topological insulators by using techniques that are also utilized in our study on the nonlinear topology. In Chapter 3, we will introduce examples of nonlinear systems and phenomena. We will also review previous studies on the nonlinear topology.

The subsequent chapters are the result part of this thesis. In Chapter 4, we will discuss the role of topology in nonlinear oscillators. In this study, we find the topological synchronization where

the bulk oscillators are chaotic and the edge ones are synchronized. In Chapter 5, we will extend the Chern number, a topological invariant characterizing two-dimensional systems, to nonlinear systems. We will also discuss its bulk-boundary correspondence in particular to the nonlinearity-induced topological phases. In Chapter 6, we will discuss the transition from topological edge modes to chaotic zero modes in one-dimensional models. Such chaos transitions can induce the breakdown of the bulk-boundary correspondence in nonlinear systems. In Chapter 7, we will summarize the thesis and discuss future perspectives of studies on nonlinear topology.

Chapter 2

Topological insulators

In this section, we review basic concepts and recent progress in studies of topological materials.

2.1 Topological materials in condensed matter

Since the quantum Hall effect was experimentally found and a theoretical study revealed its topological feature, the topology has attracted much interest in condensed matter physics [1–3]. We here review the history of studies on topological materials from such discovery of the quantum Hall effect to the recent studies in interacting many-body systems and periodically driven systems.

2.1.1 Quantum Hall effect

The quantum Hall effect is the quantization of the Hall conductivity $\sigma_{xy} = j_x/E_y$, where j_x represents the Hall current in the x direction and E_y is the electrical field in the y direction inducing the Hall current. Klitzing *et al.* [4] first observed the quantum Hall effect in a metal-oxide-semiconductor field-effect transistor under a strong magnetic field and a low temperature (cf. Fig. 2.1(a)). After this experimental discovery, Thouless, Kohmoto, Nightingale, and den Nijs [5] conducted the perturbative calculation of the Hall conductance and found that the quantized Hall conductivity is proportional to a topological invariant called the TKNN number, which is named after the initials of the authors' names. Specifically, they obtained the formula

$$\sigma_{xy} = \frac{e^2}{h} C, \tag{2.1}$$

$$C = \sum_{n:E_n<E_F} C_n, \tag{2.2}$$

$$C_n = \frac{i}{2\pi} \int_{\mathrm{BZ}} \nabla_{\mathbf{k}} \times \langle \psi_n(\mathbf{k}) | \nabla_{\mathbf{k}} | \psi_n(\mathbf{k}) \rangle d\mathbf{k}^2, \tag{2.3}$$

where e and h are the electric constant and Planck's constant, respectively. $|\psi_n(\mathbf{k})\rangle$ is the eigenvector of the nth band at the wavenumber $\mathbf{k}$ and the integral is calculated in the Brillouin zone. C_n is the TKNN number, which is equivalent to the Chern number, and C is the sum of C_n for n's whose corresponding bands are located below the Fermi energy E_F.

Other theoretical studies [50] revealed that the quantization of the Hall conductivity is related to the existence of gapless edge modes that support chiral edge currents. Such correspondence between the bulk topology characterized by the Chern number and the existence of gapless edge modes is known as the bulk-boundary correspondence, which is a central principle in topological materials. Such bulk-boundary correspondence is shown by using, e.g., the transfer matrix of the Hamiltonian of topological insulators [51, 52].

Since the quantization of the Hall conductivity is related to the nonzero Chern number, it does not require external magnetic fields. Haldane [53] theoretically proposed that the quantum Hall effect can be seen in a honeycomb lattice with internal fluxes where the net magnetic field is

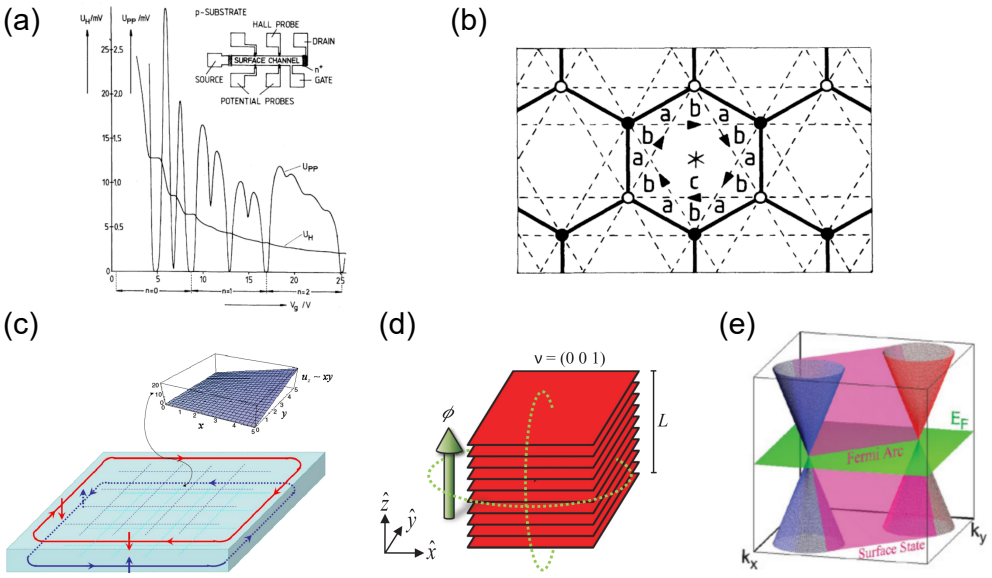

Figure 2.1: Examples of topological systems. (a) The first experiment of the quantum Hall effect. This figure is adapted from K. v. Klitzing, G. Dorda, and M. Pepper, New Method for High-Accuracy Determination of the Fine-Structure Constant Based on Quantized Hall Resistance. Phys. Rev. Lett. **45,** 494 (1980). [4]. Copyright 1980 by the American Physical Society. (b) Haldane model of the quantum anomalous Hall effect. Arrows represent the direction of the gauge field. This figure is adapted from F. D. M. Haldane, Model for a Quantum Hall Effect without Landau Levels: Condensed-Matter Realization of the "Parity Anomaly". Phys. Rev. Lett. **61,** 2015 (1988). [53]. Copyright 1988 by the American Physical Society. (c) Schematic of the quantum spin Hall effect. The directions of the edge flows depend on the spins. This figure is adapted from B. A. Bernevig and S. C. Zhang, Quantum Spin Hall Effect. Phys. Rev. Lett. **96,** 106802 (2006) [59]. Copyright 2006 by the American Physical Society. (d) Schematic of a weak topological insulator. Each layer corresponds to a two-dimensional topological insulator. This figure is adapted from Z. Ringel, Y. E. Kraus, and A. Stern, Strong side of weak topological insulators. Phys. Rev. B **86,** 045102 (2012) [69]. Copyright 2012 by the American Physical Society. (e) Surface band structure of a Weyl semimetal. There are a pair of gapless points (Weyl points) and the gapless modes appear between them. This figure is adapted from X. Wan, A. M. Turner, A. Vishwanath, and S. Y. Savrasov, Topological semimetal and Fermi-arc surface states in the electronic structure of pyrochlore iridates. Phys. Rev. B **83,** 205101 (2011) [70]. Copyright 2011 by the American Physical Society.

zero. Such quantum Hall effect without external magnetic fields is called the quantum anomalous Hall effect. The local flux considered by Haldane breaks the time-reversal symmetry and thus enables the nonzero Hall current, which also breaks the time-reversal symmetry. However, the magnetic fields generated by the local flux have alternate signs and thus cancel each other. The quantum anomalous Hall effect has also experimentally been observed in a thin film of a magnetic topological insulator [54].

While the TKNN number relies on the wavenumber-space description of the eigenvectors, which is possible only in periodic systems, realistic quantum Hall systems include disorders. In fact, the bulk-boundary correspondence is extended to such disordered systems. The early study by Laughlin [50] considered the insertion of the magnetic field in a cylindrical system and showed that it induces the spatial shift of the delocalized mode that exists at the center of the Landau level. In this discussion, the Anderson localization by disorders plays a crucial role in the quantization of the Hall current. The first study to extend the Chern number and the TKNN formula to nonperiodic systems [55] considered the twisted boundary condition instead of the wavenumber and introduced the phase factor. Then, one can define the topological invariant by substituting

the wavenumber with the phase factor in the definition of the Chern number. Furthermore, one can define the noncommutative Chern number [56–58] that only uses the real-space description of eigenstates. By using mathematical techniques in noncommutative geometry, the previous studies have also proved the bulk-boundary correspondence of the noncommutative Chern number and the quantized Hall conductivity.

2.1.2 Symmetry-protected topological phases

While the quantum Hall effect requires the breakdown of the time-reversal symmetry, nonmagnetic insulators without external magnetic fields preserve the time-reversal symmetry. One can apply the notion of topology to even such time-reversal symmetric systems. In fact, the time-reversal symmetric two-dimensional systems can exhibit the quantum spin Hall effect [7,8,59,60], which is the emergence of helical edge states. The basic strategy to construct the quantum spin Hall system is combining a layer of a Chern insulator and its time-reversal counterpart without breaking the time-reversal symmetry (Fig. 2.1(b)). Kane and Mele [7, 8] first proposed the quantum spin Hall effect in graphene, where the spin-orbit interaction can induce next-nearest neighbor couplings with nonzero phase factors that are introduced in the Haldane model. Since the phase factors have different signs depending on the spin, the whole system still preserves the time-reversal symmetry, and the up and down spin sectors can be regarded as a Chern insulator and its time-reversal counterpart. Time-reversal symmetric topological insulators are also extended to three-dimesnional systems [6], which we term topological insulators in a narrow sense.

The quantum spin Hall system is an example of symmetry-protected topological phases. In general, symmetries can alter the classification of topological phases. For example, the quantum spin Hall system is characterized by a $\mathbb{Z}_2$ topological invariant that corresponds to the parity of the number of gapless edge modes at each spin sector. Seminal studies [61,62] on the classification of topological phases established the classification table based on the Altland-Zirnbauer (AZ) symmetry classes [63]. The AZ classes consider three types of $\mathbb{Z}_2$ symmetries, the time-reversal, particle-hole, and chiral symmetries defined as

$$TH(\mathbf{k})T^{-1} = H^*(-\mathbf{k}) \quad \text{(time-reversal symmetry)}, \tag{2.4}$$

$$CH(\mathbf{k})C^{-1} = -H^T(-\mathbf{k}) \quad \text{(particle-hole symmetry)}, \tag{2.5}$$

$$\Gamma H(\mathbf{k})\Gamma^{-1} = -H(\mathbf{k}) \quad \text{(chiral symmetry)}, \tag{2.6}$$

where $H(\mathbf{k})$ is the Bloch Hamiltonian and T, C, and Γ are unitary matrices. TT^* and CC^* can be ± 1 and the symmetry classes also depend on their signs. Finally, we obtain the ten AZ classes and the classification table identifies possible topological invariants ($\mathbb{Z}$, $\mathbb{Z}_2$, or only trivial) in each symmetry class and dimension.

The classification table tells us the possible topological phases and thus is helpful to search for unexplored topological phases. We here raise two important topological phases that we can find from the classification. The first one is the $\mathbb{Z}$ phase in one-dimensional systems with chiral symmetries. As we will see in Sec. 2.2.2, such one-dimensional systems can exhibit the simplest setup of topological insulators. Secondly, if we focus on one-dimensional systems with the particle-hole symmetry, we can find the $\mathbb{Z}_2$ classification. This phase is an example of topological superconductors whose edge excitation can be considered as a Majorana fermion and thus may open up a way to topological quantum computation [64, 65].

While we have focused on the AZ symmetry classes above, one can extend the symmetry classification by considering spatial symmetries such as crystalline symmetries [66, 67]. Adding spatial symmetry, one can find new topological phases that cannot be protected without spatial symmetries (cf. one-dimensional systems with inversion and time-reversal symmetries). Furthermore, spatial symmetries can modify the definition of the topological invariants, which one can calculate from eigenvectors only at highly symmetric points in the wavenumber space, such as $k = 0$ and $k = \pi$ [6, 68]. Therefore, spatial symmetries are also of practical use to identify the topological phases of materials.

2.1.3 Weak topological insulators

In two or more dimensions, the emergence of topological boundary modes can depend on the direction of the boundary. Topological insulators with such boundary dependence of gapless boundary modes are called weak topological insulators [6, 69] because the topological boundary modes were considered to be more fragile than those in conventional (strong) topological insulators. However, weak topological insulators are also "strong" in the sense that they are topologically protected under the existence of the translational symmetry [69]. Furthermore, topological boundary modes in weak topological insulators often remain even under the existence of disorders.

A typical construction strategy of weak topological insulators is to accumulate low-dimensional topological insulators. Then, boundaries parallel to the direction of the accumulation exhibit gapless boundary modes obtained from the low-dimensional topological insulators [*1]. We can also calculate the topological invariants from the low-dimensional counterparts, which are well-defined under the existence of the translational symmetry in the direction of the accumulation. Therefore, the weak topological insulator is topologically protected.

2.1.4 Topological phases of gapless Hamiltonians

While topological insulators are topological phases of gapped Hamiltonians, the notion of topology has also been extended to gapless Hamiltonians [70,71]. A typical example of a gapless topological phase is a Weyl semimetal in three-dimensional systems, where gapless points called Weyl points are protected by the topology of the band structures around them. One can calculate the Chern number on the surface encircles a Weyl point and thus can confirm its topological protection characterized by nonzero topological invariants. In addition, topological gapless modes can appear on the surface of the Weyl semimetals, and their gapless dispersion connects a pair of Weyl points, which is called the Fermi arc. While the Weyl point can robustly exist against disorders without symmetries, other topological gapless points can be protected by symmetries, such as the time-reversal and inversion symmetries at the Dirac points [71]. The classification table of topology has also been obtained in gapless Hamiltonians [72]. If the gapless structure has a d-dimensional structure, the classification of the n-dimensional gapless Hamiltonian is related to that of a $(n-d-1)$-dimensional gapped Hamiltonian.

2.1.5 Topological phases in interacting systems

While the early studies of topological insulators have focused on noninteracting or one-body Hamiltonians, we cannot ignore the many-body interaction in experiments. Topological phases of matter have been extended to even such interacting systems, while the full understanding of many-body topology still remains unelucidated. We here review the previous studies on topological phases in interacting systems and the current understanding.

The topological phases of interacting systems are classified based on the topology of the ground state. Since the ground state of noninteracting fermions is the Slater determinant of the occupied states, its topological invariant becomes equivalent to the sum of topological invariants of occupied bands calculated from the one-body Hamiltonian. The extension of the topological invariant to interacting systems has been largely explored. For example, the early attempt by Niu, Thouless, and Wu [55] (we also mentioned in Sec. 2.1.1) considered the many-body ground state under the twisted boundary condition and calculated its TKNN formula. Green functions have also been utilized to define the topological invariants [73–75]. However, these attempts are just simple extensions of topological invariants in noninteracting systems and do not capture topological phases unique to interacting systems.

[*1] To obtain gapless boundary modes, we do not need to consider the boundary parallel to the direction of accumulation. In fact, the directions of boundaries where we cannot find gapless boundary modes are very restricted (e.g., the direction perpendicular to that of accumulation), and we find gapless boundary modes in almost all the directions [69].

The seminal study on topology in interacting systems by Fidkowski and Kitaev [76,77] showed that the interaction can change the topological classification of symmetry-protected topological phases in one-dimensional fermionic systems from $\mathbb{Z}$ to $\mathbb{Z}_8$ classification. Haldane [78] also investigated spin systems (interacting bosonic systems) and found that the gapless excitation is determined by the nontrivial topology of the bulk, which is the reason why Haldane won the Nobel prize.

Stimulated by these findings of topological phases unique to interacting systems, recent studies have tried to establish the topological classification table of interacting systems. In particular, if we focus on symmetry-protected topological phases of gapped Hamiltonians (i.e., Hamiltonians with unique ground states), the early studies concluded that such symmetry-protected topological phases are understood from the group cohomology [79, 80]. However, the following studies found topological phases that cannot be seen in the classification table obtained from the group cohomology [81]. In current understanding, symmetry-protected topological phases correspond to the (co)bordism of the classifying space of the symmetry group [82–84].

We note that nonlinear systems considered in our studies can be regarded as mean-field theories [40,41] or Kohn-Sham equations [85,86] of interacting systems. Therefore, the nonlinear topology may open up a new way to investigate quantum many-body systems.

2.1.6 Topological phases in driven systems

While conventional studies on topological materials have focused on the equilibrium state of condensed matter, recent studies have also explored topological phases in nonequilibrium systems. Specifically, Floquet systems, i.e., periodically-driven systems can be realized by applying lasers to materials [*2], and Floquet topological insulators have been proposed [88,89]. By applying lasers, one can realize high-frequency driving. Such a high-frequency modification of the Hamiltonian can be theoretically treated by the Floquet-Magnus expansion [87], which expands the Fourier-transformed Hamiltonian by the inverse of the frequency. Then, the periodic driving can open a gap at a Dirac point. A previous study [89] proposed that by applying a laser to a honeycomb lattice, one can realize the Floquet counterpart of the Haldane model [53].

Another strategy to construct Floquet topological insulators utilizes slow drivings. The topology of such slowly driven Floquet systems is understood from their unitary time-evolution operators. We here describe the time evolution from t to $t+T$ (T: the period of the driving) by $U(t+T;t)$. Then, one can define the effective Hamiltonian $H_{\rm eff}$ by $U(t+T;t) = \exp(iTH_{\rm eff})$. We note that the eigenvalues of $H_{\rm eff}$ can be equated modulo 2π and thus are called quasi-energy. Then, one can calculate the Chern number of such an effective Hamiltonian. However, there are anomalous topological phases that cannot be captured by the Chern number. A pioneering study [90] on such anomalous Floquet topological insulators has investigated a square lattice model exhibiting two bands. Since the eigenvalues can be equated modulo 2π, one can consider the gaps at $E=0$ and $E=\pi$ between two bands. Then, anomalous topological phases exhibit gapless edge modes in both the bulk gaps. The previous study also proposed a topological invariant that captures the anomalous Floquet topological insulator.

Other studies have considered the external drivings as non-Hermitian effects. We will review such non-Hermitian topology in Sec. 2.3.

2.2 Bulk-boundary correspondence in minimal models

In this section, we analytically discuss the bulk-boundary correspondence in minimal models. We also introduce some analytic techniques to analyze the topological edge modes, which are utilized in our studies. To analyze the bulk-boundary correspondence, we start from the minimal

[*2] Since the laser is an electromagnetic wave, one can describe the Hamiltonian by using periodically oscillating electric and magnetic fields.

one-dimensional model, the Su-Schrieffer-Heeger (SSH) model. Then, as its extension to two-dimensional systems, we introduce the Qi-Wu-Zhang (QWZ) model. We note that there is a lecture note [91] of topological insulators that explains the topological origin of edge modes starting from the SSH model.

2.2.1 Bloch's theorem and band structure

Before we discuss the bulk-boundary correspondence in minimal models, we first introduce the basic concepts in condensed matter physics: Bloch's theorem and band structures. We will also see that the analogies to these concepts can be found in classical systems.

In condensed matter physics, one often considers the Schrödinger equation with a periodic potential $U(\mathbf{r})$,

$$E\Psi(\mathbf{r}) = [-\nabla^2 + U(\mathbf{r})]\Psi(\mathbf{r}). \tag{2.7}$$

We introduce the lattice vectors $\mathbf{a}_j$ ($j = 1, 2, \cdots, d$ with d being the spatial dimension) that represents the periodicity of the potential, $U(\mathbf{r} + \mathbf{a}_j) = U(\mathbf{r})$. Then, Bloch's theorem states that the eigenvector must be described as

$$\Psi(\mathbf{r}) = e^{i\mathbf{k}\cdot\mathbf{r}}u(\mathbf{r}), \tag{2.8}$$

where $u(\mathbf{r})$ is a periodic function satisfying $u(\mathbf{r}+\mathbf{a}_j) = u(\mathbf{r})$. $\mathbf{k}$ represents the wavenumber of this eigenstate. One can also show that the eigenvectors in periodic lattice systems are also described by using a periodic function. In particular, if $\mathbf{r}$ denotes the representative point of each lattice point, we obtain $\Psi(\mathbf{r}) = e^{i\mathbf{k}\cdot\mathbf{r}}\psi(\mathbf{k})$, where $\psi(\mathbf{k})$ is a vector depending on the wavenumber $\mathbf{k}$ whose dimension is equal to the number of the internal degree of freedom such as sublattices and spins.

By using Bloch's theorem, one can introduce the notion of the wavenumber space, where band structures are discussed. If one considers the primitive reciprocal lattice vectors $\mathbf{b}_l$ that satisfy $\mathbf{a}_j \cdot \mathbf{b}_l = 2\pi\delta_{jl}$, the change of the eigenvector at the wavenumber $\mathbf{k} + \mathbf{b}_l$ can be identified that at the wavenumber $\mathbf{k}$ by rewriting $e^{i\mathbf{b}_l\cdot\mathbf{r}}u(\mathbf{r}) \to u(\mathbf{r})$. Therefore, the wavenumber space can be regarded as a periodic space, and thus we only consider a partial space of $\mathbb{R}^d$ wavenumber space which is called the Brillouin zone.

The eigenvalues of the eigenvectors at the wavenumber $\mathbf{k}$ (2.8) form the band structure of the Hamiltonian. To calculate the band structure, one should consider the block diagonalization of the Hamiltonian by using the Bloch waves as a basis. Then, each block is called the Bloch Hamiltonian, and by diagonalizing it, one can obtain the eigenvalues and eigenvectors at each wavenumber. In particular the eigenvalues $E(\mathbf{k})$ as functions of the wavenumber $\mathbf{k}$ are called band structures.

While the concepts discussed above are developed in condensed matter physics, one can find classical counterparts by considering the dispersion relations of periodic systems. For example, if we consider a mass-spring system [18] where masses are periodically aligned and combined with their neighbors by springs, the dispersion relation of waves in such a classical system can be calculated via the Fourier transformation. Such a calculation procedure is similar to that to calculate the band structure. Furthermore, the normal modes and their natural frequencies correspond to the eigenvectors and eigenvalues of a Hamiltonian, respectively. One can also consider continuum periodic systems, such as fluids [12] and optics [92], whose dispersion relations also make analogies to band structures. Therefore, one can extend the notion of band topology to various classical systems.

2.2.2 Su-Schrieffer-Heeger (SSH) model

While the SSH model [93] was first introduced to investigate the electronic properties of polyacetylene, studies of topological insulators have utilized it as a minimal model of a one-dimensional topological insulator. The Hamiltonian of the SSH model is described as

$$H = \sum_x (a|x, B\rangle\langle x, A| + b|x, B\rangle\langle x+1, A|) + \text{H.c.}, \tag{2.9}$$

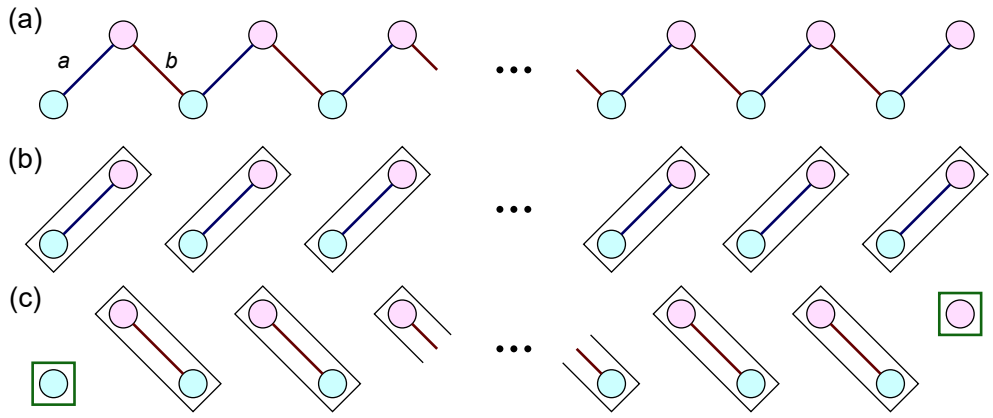

Figure 2.2: Su-Schrieffer-Heeger (SSH) model. (a) Schematic of the SSH model. The model has two sublattices (the red and blue filled circles) and staggered hoppings. (b,c) Fully polarized cases. We consider (b) $b = 0$ and (c) $a = 0$, respectively. In panel (b), the model is in the trivial phase without topological edge modes. In contrast, in panel (c), the model is in the topological phase. In this case, the edge sites (encircled by the green squares) are isolated from the others and thus the localized modes appear and exhibit different eigenvalues from the others.

where $|x, A\rangle$ and $|x, B\rangle$ represents the components of the eigenvector at the A or B sublattice of the x site, and H.c. represents the Hermitian conjugate of the previous term. This model has a chain-like structure where each sublattice is connected to its nearest neighbor sites with staggered couplings (cf. Fig. 2.2(a)).

To calculate the topological invariant, one should consider the Bloch Hamiltonian of this model,

$$H(k) = (a + be^{ik})|k, B\rangle\langle k, A| + \text{H.c.}, \tag{2.10}$$

with $|k, A\rangle$ and $|k, B\rangle$ being the component of Bloch eigenvectors at the A and B sublattice at the wavenumber k. Then, since the SSH model has the sublattice symmetry, one can define the winding number of this model as

$$\nu = \frac{1}{2\pi i}\int_0^{2\pi} dk \frac{d}{dk}\log(a + be^{ik}). \tag{2.11}$$

This winding number becomes $\nu = 1$ (resp. $\nu = 0$) at $|a| < |b|$ (resp. $|a| > |b|$) and is changed at the gapless point at $|a| = |b|$.

To understand the bulk-boundary correspondence in the finite chain of the SSH model, it is useful to consider the fully polarized case, $a = 0$ or $b = 0$. If we consider $b = 0$, the SSH model is split into pairs of coupled sites (cf. Fig. 2.2(b)). In contrast, at $a = 0$, the edge sites are isolated from the others, and thus we can obtain perfectly localized zero modes at the edge sites (cf. Fig. 2.2(c)). The absence and emergence of localized zero modes correspond to the winding number; we obtain $\nu = 0$ in the case of $b = 0$ and $\nu = 1$ in the case of $a = 0$. Since the addition of small couplings $|a| \ll |b|$ can be regarded as perturbations, the existence of localized zero modes remains at $0 < |a| \ll |b|$. We note that such a perturbative effect becomes negligibly small in the thermodynamic limit, and thus we can obtain exact zero modes at $|a| < |b|$ in the thermodynamic limit. Meanwhile, if we consider the finite system, the perturbation can lift a small gap and thus the eigenvalues of topological edge modes are not exactly zero but still small compared to the bulk gaps.

Furthermore, one can analytically show the bulk-boundary correspondence in the semi-infinite system of the SSH model. Here, we consider the right semi-infinite system with an open boundary at $x = 1$ and exact zero modes $|\Psi\rangle$ whose eigenvalue is $E = 0$. Then, Equation (2.10) yields the recurrence relations of $\langle x, A|\Psi\rangle$ and $\langle x, B|\Psi\rangle$. Solving the recurrence relations, one can show that all the B sublattice components are zero $\langle x, B|\Psi\rangle = 0$ and obtain the recurrence relation only for

$\langle x, A|\Psi\rangle$,

$$\langle x+1, A|\Psi\rangle = -\frac{a}{b}\langle x, A|\Psi\rangle. \tag{2.12}$$

From this recursion relation, the amplitudes at the A sublattices become smaller as x becomes larger in the case of $|a| < |b|$, where the winding number is $\nu = 1$. In contrast, if we consider $|a| > |b|$, the solution of the recursion relation diverges. Since such a divergent solution cannot be renormalized, one cannot obtain zero modes at $|a| > |b|$. Therefore, the winding number predicts the existence or absence of localized zero modes in the semi-infinite system, which is the bulk-boundary correspondence.

2.2.3 Qi-Wu-Zhang (QWZ) model

We next discuss the bulk-boundary correspondence in two-dimensional topological insulators. Specifically, we consider the QWZ model [94], which is a square-lattice model of a two-dimensional topological insulator. The Hamiltonian of the QWZ model is described in the real space as

$$\begin{aligned} H &= \sum_{x,y}\left(|x+1,y\rangle\langle x,y| \otimes \frac{\sigma_z + i\sigma_x}{2} + \text{H.c.}\right) \\ &\quad + \sum_{x,y}\left(|x,y+1\rangle\langle x,y| \otimes \frac{\sigma_z + i\sigma_y}{2} + \text{H.c.}\right) + u\sum_{x,y}|x,y\rangle\langle x,y| \otimes \sigma_z, \end{aligned} \tag{2.13}$$

where σ_j is the jth component of the Pauli matrix acting on the degrees of freedom of sublattices. The Bloch Hamiltonian of this model becomes

$$H(\mathbf{k}) = \sin k_x \sigma_x + \sin k_y \sigma_y + (u + \cos k_x + \cos k_y)\sigma_z. \tag{2.14}$$

We note that if we focus on the wavenumber $k_y = 0, \pi$, we can identify the Bloch Hamiltonian of the QWZ model to that of the SSH model under a proper unitary transformation. Therefore, one can predict the existence and absence of localized zero modes at $k_y = 0, \pi$ from the values of parameters. If we focus on $k_y = 0$ (resp. $k_y = \pi$), we obtain zero modes in the case of $-2 < u < 0$ (resp. $0 < u < 2$). We can also calculate the Chern number of this model and obtain

$$C = \begin{cases} 1 & (0 < u < 2) \\ -1 & (-2 < u < 0) \\ 0 & (\text{otherwise}) \end{cases}. \tag{2.15}$$

We note that the parameter regions where we obtain the nonzero Chern number match those where we obtain zero modes at $k_y = 0$ or $k_y = \pi$, which indicates the bulk-boundary correspondence in the QWZ model.

If one considers a cylindrical system of topological insulators that is periodic in the y direction and thus the wavenumber k_y in the y direction is still a good quantum number, one can obtain gapless bands of topological edge modes connecting bulk bands. The emergence of the gapless bands is explained in the QWZ model as follows; under the proper unitary transformation, the QWZ model at $k_y \neq 0, \pi$ is identified with the SSH model plus on-site terms

$$H = \sum_x (a(k)|x,B\rangle\langle x,A| + b(k)|x,B\rangle\langle x+1,A|) + \text{H.c.} + v(k)(|x,A\rangle\langle x,A| - |x,B\rangle\langle x,B|). \tag{2.16}$$

As expected from the fully polarized case, localized modes still appear, while their eigenvalues are nonzero $E \sim \pm v$. Since we can describe $v(k) = \sin k$, the eigenvalues of localized modes reach those of the bulk bands at $k = \pm\pi/2$. Therefore, one can observe the gapless band of topological edge modes. We note that the Hamiltonian (2.16) is known as the Rice-Mele model [95] if we assume k as the time t, which is a minimal model of the Thouless pump. Thus, the physics of two-dimensional topological insulators is basically the same as that of the Thouless pump in one-dimensional systems.

2.2.4 Dirac Hamiltonian as the continuum limit

One can also understand the bulk-boundary correspondence of the lattice models of topological insulators from their continuum limits, which are obtained from the low-energy expansions around the bulk gapless points. For example, if we consider the SSH model, it becomes gapless at $k = 0$ and $a = -b$ or $k = \pi$ and $a = b$ [*3]. Then, by considering the leading order term around $k \sim 0$ and $a \sim -b$, we obtain the following continuum Hamiltonian,

$$H = \begin{pmatrix} 0 & m + \partial_x \\ m - \partial_x & 0 \end{pmatrix}, \tag{2.17}$$

which is the one-dimensional Dirac Hamiltonian. We use the notation $m = a + b$. We can also obtain a similar Dirac Hamiltonian by expanding around $k \sim \pi$ and $a \sim b$. We also note that the Dirac Hamiltonian appears from the low-energy expansions of various lattice models of topological insulators including the QWZ model. Therefore, the bulk-boundary correspondence in the Dirac Hamiltonian implies the universality of the bulk-boundary correspondence.

To confirm the bulk-boundary correspondence, we here calculate the zero mode of the Dirac Hamiltonian. To obtain the zero mode, we assume the Jackiw-Rebbi solutions [96] described by

$$\begin{pmatrix} \Psi_1(x) \\ \Psi_2(x) \end{pmatrix} = \begin{pmatrix} \phi(x) \\ 0 \end{pmatrix}. \tag{2.18}$$

Substituting this assumption with Eq. (2.17), one obtains the differential equation that determines the spatial distribution of the zero mode,

$$\partial_x \phi(x) = m\phi(x). \tag{2.19}$$

One can analytically solve this equation and obtain $\phi(x) = e^{mx}\phi(0)$. If we consider the right semi-infinite system and $m < 0$, $\phi(x)$ can be normalized and thus we obtain a zero mode of the Dirac Hamiltonian. In contrast, in the case of $m > 0$, we obtain no zero modes in the right semi-infinite systems. The existence or absence of zero modes corresponds to the sign of the Chern number,

$$C = \begin{cases} \frac{1}{2} & (m > 0) \\ -\frac{1}{2} & (m < 0) \end{cases}, \tag{2.20}$$

and thus we confirm the bulk-boundary correspondence in the Dirac Hamiltonian.

2.3 Non-Hermitian topology

While closed quantum systems are described by the Schrödinger equation whose Hamiltonian is Hermitian, linear dynamics with non-Hermitian Hamiltonians have also been studied as effective descriptions of various open systems [21]. The non-Hermiticity of the Hamiltonian implies that the energy is not a physical observable in the sense that it can be changed under time evolution. Such a change of total energy in a non-Hermitian system is induced by the dissipation and injection of energy in the open system.

Recent studies have extended the notion of topology to the non-Hermitian Hamiltonians [24, 97–105, 107–112, 159]. In particular, they have revealed the complex eigenvalues of non-Hermitian Hamiltonians can induce unique topological phases and associated topological phenomena. In this section, we review previous studies on the non-Hermitian topology. Such a non-Hermitian topology is utilized in our study in Chapter 4. It is also noteworthy that the non-Hermitian system is a linear dissipative system and thus its nonlinear counterpart, i.e., a nonlinear dissipative system can show non-Hermitian-like topological phenomena, which remains intriguing future issues.

[*3] If we consider complex a and b, the SSH model becomes gapless at different k from both $k = 0$ and $k = \pi$.

2.3.1 Examples of non-Hermitian systems

Non-Hermitian Hamiltonians first attracted much interest in photonics. Photonic systems are described by the Maxwell equations, which are linear in the electrical field and the magnetic field. By assuming the set of operators in the Maxwell equations as an effective Hamiltonian, one can make an analogy to the Schrödinger equation. In addition, if we consider the dissipation of energy of light, the effective Hamiltonian of photonic systems can be non-Hermitian [113–116]. Such a non-Hermitian effect is experimentally realized by using semiconductor amplifiers or acoustic modulators.

To flexibly implement non-Hermitian Hamiltonians in experimental setups, electrical circuits [117,118] are useful due to their easiness of tuning the parameters. The dynamics of an electrical circuit is derived from Kirchhoff's law (see also Sec. 2.4.4). Then, the impedances of inductors and capacitors determine the strengths of Hermitian couplings between nodes, while the resistors realize non-Hermitian couplings. Furthermore, by using e.g., operational amplifiers, one can also realize nonreciprocal couplings [118,119].

Since one can regard any linear dynamics as non-Hermitian Schrödinger equations, recent studies have applied non-Hermitian Hamiltonians to further various classical systems. For example, previous studies have investigated non-Hermitian effects in optomechanical systems [120,121] and phononic metamaterials [122,123]. Non-Hermitian dynamics can also be seen in mesoscopic systems where thermal noises cannot be ignored. Such fluctuating systems are considered as stochastic processes and described by the master equations. Since the master equation is also a linear equation, one can discuss non-Hermitian effects in stochastic processes [124–126].

Non-Hermitian Hamiltonians of open quantum systems

Non-Hermitian Hamiltonians are also utilized to effectively describe open quantum systems, such as ultracold atoms [127,128] and quantum walks using photons [129–132]. There are three ways to derive the non-Hermitian Hamiltonians of such open quantum systems. First, one can derive the non-Hermitian Hamiltonian by tracing out the degrees of freedom of the environment around the open system, which is known as the Feshbach formula [21,133]. Here, we consider the Schrödinger equation of the total system $H|\psi\rangle = E|\psi\rangle$. Then, we consider the projection operators to the system and the environment, P_s and P_e, which satisfies $P_s + P_e = I$ (the identity operator). By acting these projection operators to the both sides of the eigenequation, we obtain

$$P_s H|\psi\rangle = EP_s|\psi\rangle, \tag{2.21}$$
$$P_e H|\psi\rangle = EP_e|\psi\rangle. \tag{2.22}$$

After some algebra, we obtain

$$P_e|\psi\rangle = (E - P_e H P_e)^{-1}(P_e H P_s)P_s|\psi\rangle. \tag{2.23}$$

Finally substituting this into the left-hand side of Eq. (2.21), $P_s H|\psi\rangle = P_s H(P_s|\psi\rangle + P_e|\psi\rangle)$, we obtain the eigenequation of the open system

$$\left[P_s H P_s + (P_s H P_e)(E - P_e H P_e)^{-1}(P_e H P_s)\right] P_s|\psi\rangle = EP_s|\psi\rangle. \tag{2.24}$$

The effective Hamiltonian of this eigenequation is $H_{\rm NH} = P_s H P_s + (P_s H P_e)(E - P_e H P_e)^{-1}(P_e H P_s)$, which is a non-Hermitian operator.

The other derivations of the non-Hermitian dynamics utilize the Gorini-Kossakowski-Sudarshan-Lindblad (GKSL) equation [134,135], which describes the dynamics of the density matrix. The GKSL equation reads

$$\partial_t \rho = -i[H,\rho] + \sum \gamma_j \left(L_j \rho L_j^\dagger - \frac{1}{2}\{L_j^\dagger L_j, \rho\} \right), \tag{2.25}$$

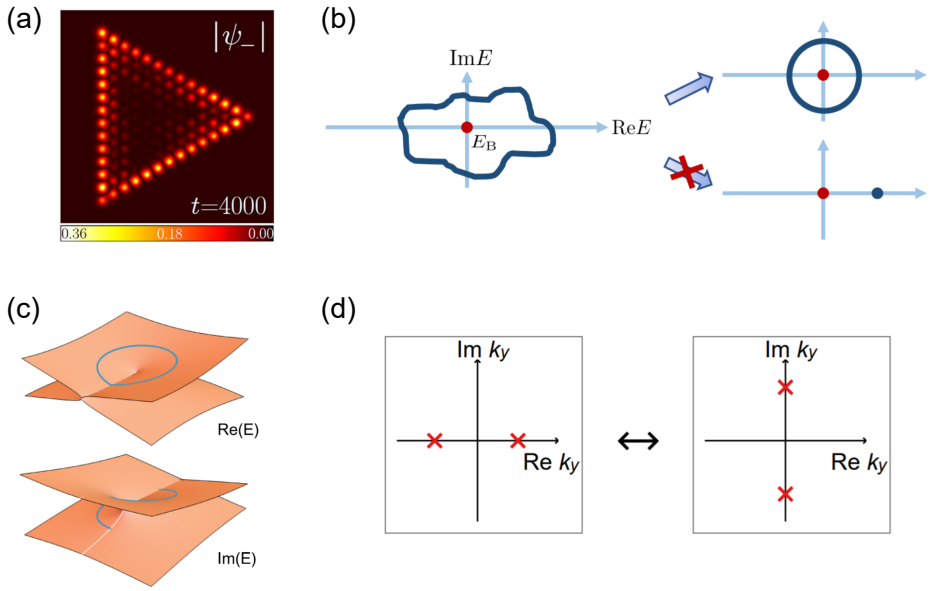

Figure 2.3: Topological phases and edge modes unique to non-Hermitian systems. (a) Amplification of light in a topological laser. Y. V. Kartashov and D. V. Skryabin, Two-Dimensional Topological Polariton Laser. *Phys. Rev. Lett.* **122,** 083902 (2019) [139]. Copyright 2019 by the American Physical Society. (b) Schematic of the point-gap topology. Without crossing the base energy (the red point), the spectrum (the blue circle) encircling the base energy cannot be adiabatically deformed to the point spectrum in the right bottom panel. This figure is adapted from Z. Gong *et al.*, Topological Phases of Non-Hermitian Systems. Phys. Rev. X **8,** 031079 (2018) [24] licenced under a Creative Commons Attribution 4.0 International License (http://creativecommons.org/licenses/by/4.0/). (c) Exceptional point in a two-dimensional band. Exceptional points can be protected by the nontrivial winding of the spectrum around them (cf. the blue curve). This figure is adapted from H. Shen, B. Zhen, and L. Fu, Topological Band Theory for Non-Hermitian Hamiltonians. Phys. Rev. Lett. **120,** 146402 (2018) [101]. Copyright 2018 by the American Physical Society. (d) Typical spectra in the PT-symmetric (left panel) and broken (right panel) phases. These two spectra cannot be transformed into each other under the existence of the PT symmetry of the Hamiltonian until two eigenvalues collide and make an exceptional point. This figure is adapted from K. Sone, Y. Ashida, and T. Sagawa, Exceptional non-Hermitian topological edge mode and its application to active matter. *Nat. Commun.* **11,** 5745 (2020) [27] licensed under a Creative Commons Attribution 4.0 International License (http://creativecommons.org/licenses/by/4.0/).

where ρ is the density matrix and H and L_j are the Hamiltonian and the jump operators, respectively. This equation is linear in the density matrix. Therefore, by rewriting the density matrix into a vector form $\rho = \sum_{ij} c_{ij}|i\rangle\langle j| \to \sum_{ij} c_{ij}|i,j\rangle$, one can assume the superoperator in the GKSL equation as an effective non-Hermitian Hamiltonian. Furthermore, if we ignore the term $L_j \rho L_j^\dagger$ by considering the post-selection, one can assume the GKSL equation as the von Neumann equation with the effective Hamiltonian being $H + i\sum \gamma_j L_j^\dagger L_j$. Therefore, $\tilde{H} = H + i\sum \gamma_j L_j^\dagger L_j$ can be used as the non-Hermitian Hamiltonian that describes the dynamics after the post-selection.

2.3.2 Topological lasers

Unlike Hermitian Hamiltonians, non-Hermitian Hamiltonians can have complex eigenvalues. The imaginary part of an eigenvalue corresponds to the rate of amplification or attenuation of the eigenvector, which is induced by the injection or dissipation of energy. Such amplifications of eigenvectors can be of practical use. Specifically, the amplification of topological edge modes has attracted attention due to its possible applications to photonic devices named topological lasers.

Topological lasers [22, 23, 109, 136–140] are photonic devices that amplify edge sites by using nontrivial bulk topology (see also Sec. 2.4.1 for the way to realize topological effective Hamiltonians in photonic systems). Since topological materials exhibit scattering-free chiral current, topological lasers can transfer the amplified wave packet robustly against disorders, which can be advantageous in the view of energy efficiency. The pioneering works of topological lasers [22, 23] introduced judicious gains only at the edge of the system into the photonic counterpart of topological insulators. Such judicious gains only amplify the topological edge modes and thus can realize the desired properties of topological lasers.

Other proposals of topological lasers utilized symmetry-protected topological edge modes. In one-dimensional systems, the non-Hermitian extension of the SSH model [136, 138] can exhibit amplification of edge modes, which are protected by the chiral symmetries. In two-dimensional systems, recent studies have also proposed topological lasers without propagations of amplified wave packets [109, 140].

As we will discuss in Sec. 2.3.5 and Appendix A, we also proposed symmetry-protected topological lasers that utilize nontrivial topology around exceptional points [27] (see Sec. 2.3.5 for the definition of the exceptional point). Furthermore, we will also show the existence of topological lasers using neither judicious gains nor symmetries in Appendix A. Such symmetry-free topological lasers may broaden possible experimental setups of topological lasers.

2.3.3 Point-gap topology

While we have discussed the applicational advantage of the amplification of edge modes, the complex eigenvalues of non-Hermitian Hamiltonians also play crucial roles in the topological classification of non-Hermitian systems. Specifically, a set of complex eigenvalues can have topological structures such as winding around the origin, which enables us to define topological invariants unique to non-Hermitian systems.

To discuss such topological phases unique to non-Hermitian systems, a previous study [24] proposed two definitions of band gaps in non-Hermitian Hamiltonians. The first one is a line gap, where the complex bands do not cross a line such as the imaginary axis of the complex energy plane. Since one can adiabatically modify a line-gapped non-Hermitian Hamiltonian into a gapped Hermitian Hamiltonian, the topological classification of line-gapped non-Hermitian Hamiltonians becomes equivalent to that of gapped Hermitian Hamiltonians. The other definition of band gaps is a point gap, where the complex bands do not contain a base energy that we determine in advance. If the complex band encircles the base energy, one cannot adiabatically modify the point-gapped Hamiltonian into a Hermitian Hamiltonian. Therefore, the point-gap topology can induce topological phenomena unique to non-Hermitian systems.

We demonstrate the existence of topological phases based on the point gaps in a prototypical model of non-Hermitian systems, which is called the Hatano-Nelson model [141] and was first introduced to investigate the dynamics of magnetic flux in superconductors. The Hamiltonian of the Hatano-Nelson model (without disorders) is defined in the real space as

$$H = \sum_x \left(a|x\rangle\langle x+1| + b|x+1\rangle\langle x| \right). \tag{2.26}$$

The Bloch Hamiltonian of this model is

$$H(k) = ae^{ikx} + be^{-ikx}, \tag{2.27}$$

which is a scalar function of k. In the case of $|a| \neq |b|$, the complex energy band of this Hamiltonian $E(k) = ae^{ikx} + be^{-ikx}$ forms an ellipse and has a point gap around the origin. If we consider $|a| > |b|$ (resp. $|a| < |b|$), the eigenvalues $E(k)$ wind clockwise (resp. counterclockwise) around the origin from $k = 0$ to $k = 2\pi$. To change the direction of the winding, the point gap must be closed at $|a| = |b|$, and thus these two parameter regions $|a| > |b|$ and $|a| < |b|$ are topologically distinguished. One can also define the topological invariant characterizing the point-gap topology

of the Hatano-Nelson model as

$$\nu = \frac{1}{2\pi i}\int dk \frac{d}{dk}\log(ae^{ikx} + be^{-ikx}), \tag{2.28}$$

which becomes $\nu = 1$ (resp. $\nu = -1$) for $|a| > |b|$ (resp. $|a| < |b|$). This winding number also indicates the existence of topological phases based on the point gaps.

In general, the point-gap topology of a one-dimensional non-Hermitian system is characterized by the following winding number:

$$\nu = \frac{1}{2\pi i}\int dk \frac{d}{dk}\log\det(H(k) - E_b I), \tag{2.29}$$

where $H(k)$ is the Bloch hamiltonian of the non-Hermitian system, E_b is the base energy, and I is an identity matrix. By using the identity $\log\det(H(k) - E_b I) = \mathrm{Tr}\log(H(k) - E_b I)$, we can check that this winding number is equal to the sum of the winding numbers of the eigenvalues of $H(k) - E_b I$. Therefore, the winding number ν can take arbitrary integer values, and thus we obtain $\mathbb{Z}$ classification of one-dimensional non-Hermitian systems without symmetries.

As can be seen in the Hatano-Nelson model, the winding number basically corresponds to the nonreciprocity in hoppings to the left and right sites. Such nonreciprocal hoppings can induce the localization. In fact, previous studies [111, 112] have revealed that the nonzero winding number in a one-dimensional non-Hermitian system corresponds to the localization of the bulk modes, which is known as the non-Hermitian skin effect [102–105, 107, 159]. The non-Hermitian skin effect also drastically changes the complex energy spectrum under the open boundary condition from that under the periodic boundary condition. Such drastic changes and the localization of bulk modes lead to the apparent breakdown of the bulk-boundary correspondence in non-Hermitian systems. To recover the bulk-boundary correspondence, previous studies [104, 107, 142] proposed the non-Bloch band theory, which extends the wavenumber to a complex one to describe the localized bulk modes. By using the non-Bloch band theory, one can obtain the eigenvectors corresponding to localized bulk modes and calculate the topological numbers using these localized bulk modes. Then, such topological numbers recover the bulk-boundary correspondence.

One can also generalize the point-gap topology to higher-dimensional systems and symmetry-protected topological phases. To obtain the classification of the point-gap topology, previous studies have used the following fact; the topological classification of the point-gap topology of a non-Hermitian Hamiltonian H is the same as that of a gapped Hermitian Hamiltonian constructed from H as

$$H' = \begin{pmatrix} 0 & H \\ H^\dagger & 0 \end{pmatrix}. \tag{2.30}$$

One can show this fact from the one-to-one correspondence between this chiral-symmetric Hamiltonian and a general non-Hermitian Hamiltonian. Then, the classification of the non-Hermitian topology is calculated from the clasification of the corresponding Hermitian Hamiltonians.

The extensions of the point-gap topology to higher-dimensional systems and symmetry-protected topological phases have revealed topological phenomena beyond the one-sided localization of bulk modes. For example, the point-gap topology protected by the time-reversal symmetry can induce the localization of the bulk modes to both ends of a one-dimensional system (sometimes termed reciprocal non-Hermitian effects) [111,143]. In three-dimensional systems, the nontrivial point-gap topology can realize exceptional topological insulators [144], where the complex bands of localized modes exhibit exceptional points. In addition, the notion of the (nonreciprocal) skin effect can be altered in higher-dimensional systems due to its sensitivity to the boundary geometry [145]. Very recent studies [146, 147] have tried to obtain the non-Bloch band theory in two-dimensional systems, while the comprehensive understanding of the skin effect in two or more dimensions remains a future issue.

2.3.4 Symmetry classification of non-Hermitian topology

Like the quantum spin Hall effect in Hermitian systems [7, 8, 59, 60], the symmetries of non-Hermitian Hamiltonians can alter the topological classification. Since the Hermitian conjugate of a non-Hermitian Hamiltonian can be different from the original one, the unitary and anti-unitary symmetries are more abandunt in non-Hermitian systems than in Hermitian systems. Specifically, we must separately treat the following symmetries,

$$TH(\mathbf{k})T^{-1} = H^*(-\mathbf{k}), \quad T'H(\mathbf{k})T'^{-1} = H^T(-\mathbf{k}) \quad \text{(time-reversal symmetry)}, \tag{2.31}$$

$$CH(\mathbf{k})C^{-1} = -H^T(-\mathbf{k}), \quad C'H(\mathbf{k})C'^{-1} = -H^*(-\mathbf{k}) \quad \text{(charge-conjugation symmetry)}, \tag{2.32}$$

$$\Gamma H(\mathbf{k})\Gamma^{-1} = -H^\dagger(\mathbf{k}), \quad SH(\mathbf{k})S^{-1} = -H(\mathbf{k}) \quad \text{(chiral and sublattice symmetries)}. \tag{2.33}$$

The difference in definitions of the symmetries indeed affects the topological classification of the non-Hermitian system. For example, the point gap topology of the chiral symmetric one-dimensional system is trivial, while that of the sublattice symmetric system is $\mathbb{Z}^2$. These symmetries are not independent because we can construct the chiral and sublattice operators as $\Gamma = TC = T'C'$ and $S = TC' = T'C$, respectively. Therefore, if the system has both the time-reversal and charge-conjugation symmetries, it must have the chiral or sublattice symmetry. Furthermore, by considering the rotation of the phase in the non-Hermitian Hamiltonian $H \to iH$, one can identify some symmetries. Reflecting these facts, one can show that there are 38 symmetry classes that play an important role in the topological classification of the non-Hermitian system, which are termed the Bernard-LeClair (BL) symmetry classes [108, 109, 148, 149]. Based on the BL symmetry classes, previous research proposes the classification table of the non-Hermitian topology [108, 109].

The degrees of freedom of the definition can be seen in other unitary symmetries than the chiral and sublattice symmetries. In particular, previous research [150] discussed the importance of the spatial symmetry with the Hermitian conjugate

$$PH(\mathbf{k})P^{-1} = H^\dagger(\tilde{\mathbf{k}}), \tag{2.34}$$

with $\tilde{\mathbf{k}}$ being the wavevector inverted from $\mathbf{k}$ by the symmetry operation P.

2.3.5 Exceptional points

As in Hermitian systems, gapless Hamiltonians can also have topological properties. The topological gapless structures unique to non-Hermitian systems are known as exceptional points [25]. The exceptional points are defined as the point in the parameter space where the eigenvectors coalesce and thus the non-Hermitian Hamiltonian becomes nondiagonalizable. Since Hermitian matrices are always diagonalizable, the exceptional points are unique to non-Hermitian systems. The exceptional points exhibit branchpoint structures or Riemann-surface structures around them (cf. Fig. 2.3(c)). The topology of such branchpoint structures or Riemann-surface structures plays a crucial role in the robust existence of the exceptional points [26, 101, 151].

In more detail, the topological protection of exceptional points is related to the point-gap topology of non-Hermitian systems. In two-dimensional systems, an exceptional point appears with a Riemann-surface structure. Then, adiabatically changing the wavenumber along a closed path around the exceptional point, we obtain different eigenvalues and eigenvectors at the start and end points [26]. Such exchanges of eigenvalues can occur owing to the winding structure of the Riemann-surface structure. Thus, one can define the winding number that characterizes the topology of the exceptional point

$$\nu = \frac{1}{2\pi i} \oint d\mathbf{k} \cdot \nabla_{\mathbf{k}} \log \det(H(\mathbf{k}) - E_{\mathrm{EP}} I), \tag{2.35}$$

where E_{EP} is the eigenvalue at the exceptional point. The similarity of this winding number to that in Eq. (2.29) is not a coincidence. In fact, the topology of the exceptional points is characterized

by the point-gap topology of non-Hermitian systems whose dimension is one less than the original system [151].

In one-dimensional systems, the topological protection of exceptional points requires proper symmetries. Specifically, one should consider the PT and CP symmetries and the pseudo-Hermiticity [151–154] defined as

$$PTH(\mathbf{k})(PT)^{-1} = H^*(\mathbf{k}) \ \ (PT \text{ symmetry}), \tag{2.36}$$

$$CPH(\mathbf{k})(CP)^{-1} = -H^*(\mathbf{k}) \ \ (CP \text{ symmetry}), \tag{2.37}$$

$$\eta H(\mathbf{k})\eta^{-1} = H^\dagger(\mathbf{k}) \ \ (\text{pseudo-Hermiticity}), \tag{2.38}$$

where $H(k)$ represents the Bloch Hamiltonian. One can also utilize the chiral symmetry in Eq. (2.33) to protect exceptional points. Focusing on the PT symmetry, all the eigenvalues must be real or appear with their complex-conjugate counterparts. Then, one can define the topological invariant [155, 156]

$$\nu = \mathrm{sgn}(\det H(k_0 - \delta)H(k_0 + \delta)), \tag{2.39}$$

where k_0 is the wavevector at the exceptional point, and δ is a small real number. One can show that $\det H(k_0 \pm \delta)$ in this topological invariant must be real, and thus this topological invariant becomes ± 1, which provides $\mathbb{Z}_2$ classification of the exceptional point. If the topological invariant is $\nu = -1$, one can guarantee the topological protection of the exceptional point. Such topologically protected exceptional points are not removed by the continuous deformation of the Hamiltonian until they collide with other exceptional points.

The emergence of the exceptional point in one-dimensional band structures is also related to the spontaneous symmetry breaking of the eigenvectors, which is called the PT symmetry breaking [157]. In fact, around an exceptional point, a complex-conjugate pair of eigenvalues becomes a pair of real eigenvalues. Then, one can show that the eigenvectors $|\Psi_\pm\rangle$ corresponding to the complex-conjugate pair of eigenvalues are swapped $PT|\Psi_\pm\rangle \propto |\Psi_\mp\rangle$, which indicates the breakdown of the PT symmetry in eigenvectors. In contrast, the eigenvector $|\Psi\rangle$ of the real eigenvalue is PT symmetric $PT|\Psi\rangle \propto |\Psi\rangle$. Therefore, the exceptional point is also the PT symmetry breaking point. We note that the emergence of exceptional points is also discussed in the non-Blcoh band theory (cf. Sec. 2.4.3) [158]. Recent research [159, 160] discussed that the emergence of exceptional points in a one-dimensional non-Bloch band can be related to the breakdown of the non-Bloch extension of the PT symmetry.

Studies on non-Hermitian systems have also discussed the applications of exceptional points. In photonic systems, one can observe the coherent absorption [161] where all the injected light is absorbed without reflections. In addition, nonreciprocal media can realize unidirectional invisibility [162] where the reflection rate of the light only in a specific direction becomes zero. One also utilizes the exceptional point to sensor devices by using the square-root dispersion around the exceptional point. Since the slope of the dispersion diverges around the exceptional point, one can amplify the signal by using the exceptional points, which is known as the enhanced sensitivity [163].

In our previous study [27], we discussed the role of exceptional points in topological edge modes and revealed an unconventional mechanism to protect gapless modes. We term such gapless edge modes *exceptional edge modes*. We have also discussed its applications to topological lasers and active matter. Therefore, the interplay between exceptional points and topological edge modes can further enrich the topological phases of non-Hermitian systems. We will review our previous result on exceptional points in Appendix A. In our study, we further reveal the possible application to three-dimensional topological lasers. In Appendix A, we will also discuss such topological lasers using exceptional surface modes.

2.4 Topological insulators beyond solid-state physics

While early studies of band topology focused on the band structure in electronic systems, one can make an analogy between band structures and dispersion relations in other classical and quantum

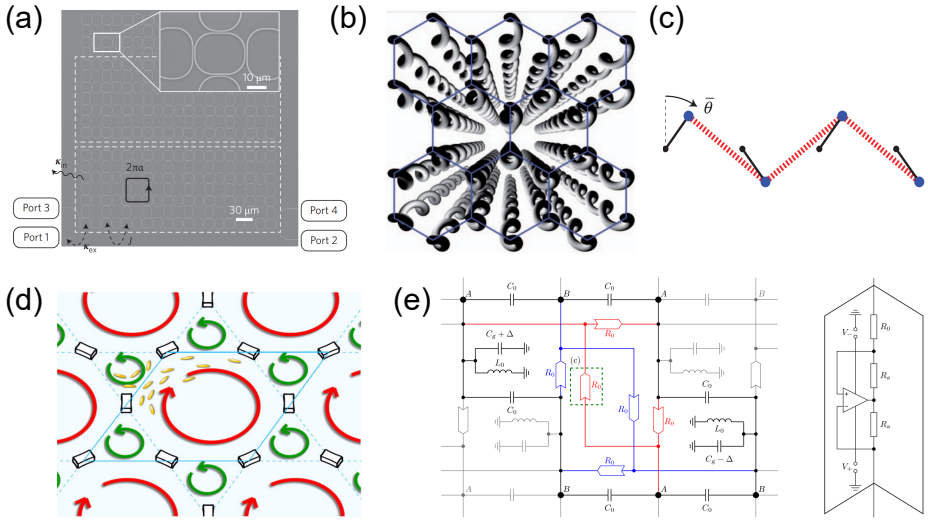

Figure 2.4: Classical counterparts of topological insulators. (a) Photonic topological insulator using a ring-resonator array. This figure is adapted from M. Hafezi, S. Mittal, J. Fan, A. Migdall, and J. M. Taylor, Imaging topological edge states in silicon photonics, Nat. Photonics **7,** 1001 (2013) [165], Springer Nature. Copyright 2013. (b) Photonic Floquet topological insulator using periodically modulated waveguides. The direction parallel to the waveguides effectively plays a role of time. This figure is adapted from M. C. Rechtsman *et al.*, Photonic Floquet topological insulators. Nature **496,** 196-200 (2013) [168], Springer Nature. Copyright 2013. (c) Schematic of a topological mechanical lattice. Each mass is connected to its neighbors by springs as depicted by the red dot lines. This figure is adapted from C. L. Kane and T. C. Lubensky, Topological boundary modes in isostatic lattices. Nat. Phys. **10,** 39-45 (2014). [18], Springer Nature. Copyright 2014. (d) Active-matter counterpart of the quantum anomalous Hall effect. Pillars located at lattice points of a kagome lattice rectify the steady flow depicted by the red and green curved arrows. These flows behave as the effective vector potentials realizing the quantum anomalous Hall effect. This figure is adapted from K. Sone and Y. Ashida, Anomalous Topological Active Matter. Phys. Rev. Lett. **123,** 205502 (2019) [206]. Copyright 2019 by the American Physical Society. (e) Electrical circuit of the quantum anomalous Hall effect. The right panel shows the negative impedance converters with current inversion, which realizes a nonreciprocal coupling and thus breaks the time-reversal symmetry. This figure is adapted from T. Hofmann, T. Helbig, C. H. Lee, M. Greiter, and R. Thomale, Chiral Voltage Propagation and Calibration in a Topolectrical Chern Circuit. Phys. Rev. Lett. **122,** 247702 (2019) [119]. Copyright 2019 by the American Physical Society.

systems. Using such an analogy, recent studies have extended the notion of topology to various systems. In this section, we review such extensions of topological insulators to both classical and quantum systems.

2.4.1 Photonics

Dynamics of photonic systems are basically described by the Maxwell equations, which are linear equations of the electrical and magnetic fields. If we consider periodic media, one can periodically modulate the permittivity and obtain linear equations with discrete translational symmetries. Therefore, one can construct an analogy between photonic metamaterials and solid-state physics. Following such a strategy, Haldane and Raghu first proposed topological photonics [92], which is also the first proposal of classical topological insulators.

Since analyzing the full Maxwell equations is exhausting, reduced equations are often used to discuss the topological properties of photonic metamaterials. For example, one can derive the reduced equations in ring-resonator arrays from the mode-coupling theory [166,167]. In the mode

coupling theory, the dynamics of light in the ring-resonator arrays can be approximately described by the linear coupling of clockwise and counterclockwise modes in each ring resonator. The coupling between different ring resonators originates from the evanescent light; the penetration of light to neighbor ring resonators introduces interactions. The amplitude of a linear coupling is determined from the distance between the ring resonators, and its phase factor is tuned by the length of waveguides of the resonators. The signs of the phase factors of linear couplings are opposite for clockwise and counterclockwise modes. The linear equations derived from the mode coupling theory in ring-resonator arrays usually have the time-reversal symmetry and thus one can realize photonic counterparts of the quantum spin Hall effect [165].

Previous studies on photonic metamaterials have also considered standing waves in periodic media. Such standing waves of light are described by the wave equation derived from the Maxwell equation [9–11],

$$\nabla \times \left[\boldsymbol{\mu}^{-1}(\mathbf{r})\nabla \times \mathbf{E}(\mathbf{r})\right] = \omega^2 \boldsymbol{\epsilon}(\mathbf{r})\mathbf{E}(\mathbf{r}). \tag{2.40}$$

Furthermore, if one considers the waveguides array and assumes that the light propagates along paraxial directions close to the z direction, the above equation can be regarded as a Floquet dynamics by replacing z into the effective time t'. Based on this eigenequation for the standing waves, previous studies [168] proposed that wire-like waveguide arrays can be photonic counterparts of Floquet topological insulators. In such waveguide arrays, one can periodically modulate the distance between waveguides, which determines the strength of couplings between the waveguides. Then, the periodic modulations in the z direction realize an effective Floquet system and a counterpart of a minimal model of Floquet topological insulators.

Topological photonics have been widely investigated and the examples are not restricted to those raised above. By utilizing gyromagnetic photonic crystals, one can break the time-reversal symmetry and realize photonic counterparts of the quantum anomalous Hall effect [169]. In three-dimensional systems, photonic counterparts of weak topological insulators and Weyl semimetals are also proposed [170–173].

Furthermore, non-Hermitian effects in topological photonics are also investigated. As discussed in Sec. 2.3.2, topological lasers [22, 23, 109, 136–140] are typical non-Hermitian topological devices in photonics. One can also observe the non-Hermitian skin effect in a laser array and a resonator array [174, 175]. Studies on exceptional points often utilize photonics, and associated phenomena such as interchanging of eigenvectors [26], enhanced sensitivity [163], and unidirectional invisibility [162] are proposed and observed in photonic setups.

2.4.2 Phononic metamaterials

Metamaterial science also aims to control waves of fluids such as air and water. Such fluidic waves, i.e., phononic waves are basically described by the Navier-Stokes equations,

$$\partial_t \rho + \nabla \cdot (\rho \mathbf{v}) = 0, \tag{2.41}$$

$$\partial_t \mathbf{v} + (\mathbf{v} \cdot \nabla)\mathbf{v} = -\frac{1}{\rho}\nabla P + D\nabla^2 \mathbf{v} + \mathbf{f}, \tag{2.42}$$

where ρ and $\mathbf{v}$ are the density and the velocity field, P is the pressure and $\mathbf{f}$ represents the external force. The Navier-Stokes equations are nonlinear equations. However, if we consider the fluctuations of the density and velocity fields around the steady state, one can linearize the Navier-Stokes equations and construct an analogy to the Schrödinger equations. The linearized equation reads [12]

$$\frac{1}{\rho}\nabla \cdot \rho \nabla \phi - \frac{1}{c^2}(\partial_t + \mathbf{v}_0 \cdot \nabla)^2 \phi = 0, \tag{2.43}$$

with ρ being the density and $\mathbf{v}_0$ being the velocity field of the steady state. We note that ϕ is a velocity potential and the pressure p is represented as $p = \rho(\partial_t + \mathbf{v}_0 \cdot \nabla)\phi$. We conduct the Fourier

transformation of $\Psi = \sqrt{\rho}\phi$ and rewrite the equation as

$$[(\nabla - i\mathbf{A}_{\text{eff}})^2 + V)]\Psi = 0, \tag{2.44}$$

where $\mathbf{A}_{\text{eff}}$ and V are the effective vector potential and scalar potential $\mathbf{A}_{\text{eff}} = -\omega\mathbf{v}_0/c^2$ and $V = -|\nabla \ln \rho|^2/4 - \Delta \ln \rho/2 + \omega^2/c^2$, with ω being the frequency. This equation indicates that the steady flow plays a role of an effective vector potential in phononic metamaterials.

The pioneering work of topological phononics [12] utilized cylindrical rotating objects to realize the steady flow imitating the vector potential in Chern insulators. In more detail, they arrange the rotating object at each lattice point of a triangular lattice. Such rotating materials generate the circulating flows around them, which have the same origin as the Couette flow. Then, they made an analogy between the circulating steady flows and the vector potential of Haldane's honeycomb model [53] and proposed a topological fluidic system. Backscattering-free chiral current in the proposed phononic system is confirmed from numerical simulations; they considered the source of oscillations at the edge where the fluid oscillates by the external force and calculated the dynamics of fluids.

Without the nonzero steady flow, the effective Hamiltonian derived from the hydrodynamics has the time-reversal symmetry and thus cannot construct a phononic counterpart of the quantum Hall effect. However, it is still possible to realize phononic topological insulators [176] and semimetals [177, 178] by engineering waveguides with periodic structures.

One interesting application of the topology in fluids is found in geophysics. A previous study [13] showed that the Kelvin wave and the Yanai wave have a topological origin. In particular, they analyzed the linearized hydrodynamics on a rotating sphere and revealed that it exhibits chiral boundary modes along the equator. The equatorial wave is induced by the effective magnetic field that is derived from the Collioris force. They also compared the dispersion relations of the boundary modes with those of the Kelvin wave and the Yanai wave.

2.4.3 Mechanical lattices

Spring-mass systems are typical systems that we learn in elementary lectures of classical mechanics. However, even such simple classical systems can construct analogies of topological insulators. If we consider periodically aligned mass points combined to neighbors by springs, its dynamics is described by the Newton equations

$$\frac{d^2\mathbf{r}_j}{dt^2} = -\sum_k a_{jk}(\mathbf{r}_j - \mathbf{r}_k), \tag{2.45}$$

where $\mathbf{r}_j$ is the location of mass at the site j. Since this is a linear equation with the translational symmetry, one can construct an analogy to condensed matter physics. In fact, the Fourier transformation of Eq. (2.45) leads to the eigenvalue problem in the wavenumber space, whose eigenvector and eigenvalue correspond to a normal mode and its natural frequency, for each.

Kane and Lubensky [18] proposed that a spring-mass system with the zig-zag lattice structure imitates the SSH model (cf. Sec. 2.2.2), which is a minimal one-dimensional topological insulator. Then, zero modes correspond to the floppy mode, where the mass at an edge site can be easily moved. By reflecting on the existence of topological floppy modes, they also discussed the modification of Maxwell's count [179, 180] of mechanical lattices, which is the equation between the number of zero modes and those of mass points and bonds.

One can also break the time-reversal symmetry by using external energy resources and realize the counterpart of the quantum Hall effect. Specifically, some previous studies [19] utilized gyroscopic motors attached to masses to break the time-reversal symmetry. Such gyroscopic motors generate the Lorentz force, which acts the mass perpendicularly to its velocity. Such a perpendicular force is analogical to the magnetic force and thus can realize the counterpart of the quantum Hall effect, which we can observe under the external magnetic field.

More recently, studies on mechanical metamaterials have proposed the use of active elements, where the energy is injected and nonreciprocal forces can be realized. For example, if we consider active elements with fans that can change their angles dependently on the distances between elements, we can realize distance-dependent nonreciprocal forces, which are perpendicular to the displacement between the locations of the elements [181]. Such a nonreciprocal force is termed *odd elasticity* and can be used to investigate non-Hermitian topological phenomena in mechanical lattices [182].

2.4.4 Electrical circuits

As discussed in Sec. 2.3.1, electrical circuits are flexible platforms to study topological physics, because one can realize almost arbitrary linear couplings. The dynamics of electrical circuits are determined by Kirchhoff's law, which guarantees that the sums of currents flowing in and out of a node are the same. Such conversation of currents is described as

$$I_a = \sum_b C_{ab}(V_a - V_b) + C_a V_a = \sum_b J_{ab} V_b, \tag{2.46}$$

where V_a and I_a are the voltage and input current at the node a. C_{ab} is the inverse of the impedance of the circuit element existing between a and b sites, and C_a is that between a site and the ground. If we further assume that the current resources of the input currents are capacitors with the capacitance C, Equation (2.46) reads

$$i\frac{dV_a}{dt} = \frac{1}{C}\sum_b iJ_{ab}V_b. \tag{2.47}$$

Thus, iJ_{ab} plays a role of the effective Hamiltonian of the electrical circuit.

By tuning the impedance of circuit elements, one can realize various effective Hamiltonians iJ_{ab}, which include the counterparts of topological insulators [16,17,117–119,183,184]. While common elements such as inductors, capacitors, and resistors cannot realize nonreciprocal couplings $J_{ab} \neq J_{ba}$, recent studies have also proposed negative impedance converters with current inversion (INIC) that realize the nonreciprocal coupling in electrical circuits. The INIC is the circuit in the right panel of Fig. 2.4(e). In this circuit, the input current $I_{\rm in}$ and the output current $I_{\rm out}$ are described as

$$I_{\rm out} = \frac{1}{R}(V_{\rm in} - V_{\rm out}), \tag{2.48}$$

$$I_{\rm in} = -\frac{1}{R'}(V_{\rm in} - V_{\rm out}), \tag{2.49}$$

with $V_{\rm in/out}$ being the input and output current, respectively. We can see that the signs of the linear couplings are opposite and thus can realize nonreciprocal couplings. The nonreciprocal couplings by the INICs enable us to investigate the electrical circuit realization of the quantum anomalous Hall effect [119] and non-Hermitian skin effects in electrical circuits [117,118].

2.4.5 Ultracold atoms

One can realize counterparts of topological insulators in ultracold atoms by judiciously designing the optical lattice that traps the atoms [15]. The coupling strength can be easily tuned by the depth of the harmonic potential of the optical lattice. The first demonstration of topological gapless modes in ultracold atoms utilized a honeycomb lattice [14]. By periodically oscillating the potentials made by lasers, one can realize a counterpart of a Floquet topological insulator. The Floquet-Magnus expansion of the Floquet Hamiltonian of the experimental setup becomes the Hamiltonian of the Haldane model. Since the Haldane model was thought to be a toy model that is hard to realize in condensed matter [53], this effective realization of the Haldane model was a surprise to the researchers in topological physics and thus stimulated the studies of topological

edge modes in ultracold atoms. Recent research has also investigated non-Hermitian topological phenomena such as the non-Hermitian skin effect [185,186] and the PT-symmetry breaking [187].

Since ultracold atoms are interacting bosonic systems, they provide controllable platforms to investigate the effect of many-body interactions on topological edge modes. We note that one can analyze such many-body interactions via the nonlinear equations (cf. the Gross-Pitaevskii equation in Sec. 3.1.3) obtained from their mean-field analysis, and thus ultracold atoms may also be useful to study the nonlinear topology.

2.4.6 Active matter

Studies of topological insulators have also explored possible applications in biological systems. In particular, topological active matter forms a field of research [188]. The active matter is a collection of self-driven particles that can move around by consuming the energy stored inside. Examples of active matter are abundant in biological systems, such as a school of fish [189], bacterial flows [190–192], collective motion of cells [193–195], and biological motors [196, 197]. Furthermore, one can synthesize active particles whose self-driving motions are realized by, e.g., using thermoosmotic flows [198], autophoretic processes [199], or Marangoni flow [200].

One can describe the collective motion of active matter by the hydrodynamic equations [201, 202]. The widely used hydrodynamic model of active matter is the Toner-Tu model [203, 204]

$$\partial_t \rho + \nabla \cdot (\rho \mathbf{v}) = 0, \tag{2.50}$$

$$\begin{aligned} & \partial_t \mathbf{v} + \lambda(\mathbf{v}\cdot\nabla)\mathbf{v} + \lambda_2(\nabla\cdot\mathbf{v})\mathbf{v} + \lambda_3\nabla|\mathbf{v}|^2 \\ = \;& (\alpha - \beta|\mathbf{v}|^2)\mathbf{v} - \nabla P + D_B\nabla(\nabla\cdot\mathbf{v}) + D_T\nabla^2\mathbf{v} + D_2(\mathbf{v}\cdot\nabla)^2\mathbf{v} + \mathbf{f}. \end{aligned} \tag{2.51}$$

By considering the fluctuations of the density and velocity fields from the steady state, $\delta\rho = \rho - \rho_0$ and $\delta\mathbf{v} = \mathbf{v} - \mathbf{v}_0$ (ρ_0: the density at the steady state, $\mathbf{v}_0$: the velocity at the steady state), one can linearize the Toner-Tu equation. The obtained effective Hamiltonian becomes [205, 206] [*4]

$$i\frac{d}{dt}\begin{pmatrix} \delta\rho \\ \delta v_x \\ \delta v_y \end{pmatrix} = \begin{pmatrix} -i\mathbf{v}_{\rm ss}\cdot\nabla & -i\partial_x & -i\partial_y \\ -i\partial_x & -i\lambda\mathbf{v}_{\rm ss}\cdot\nabla & 0 \\ -i\partial_y & 0 & -i\lambda\mathbf{v}_{\rm ss}\cdot\nabla \end{pmatrix}\begin{pmatrix} \delta\rho \\ \delta v_x \\ \delta v_y \end{pmatrix}, \tag{2.52}$$

where we also conduct nondimensionalization. With a little more algebra, one can obtain the Schrödinger-like equation that is similar to Eq. (2.44). Therefore, by rectifying the steady flow so that it imitates the vector potential in topological insulators, one can realize topological active matter.

Unlike passive fluids, active matter can generate steady flow without using external forces. The first proposal of topological active matter [205] utilized the circular annuli aligned on the Lieb-lattice structure. In each annulus, the active particles rotate in the clockwise or counterclckwise direction. Since the direction of motions should be the same on the boundary of the circular annuli, the direction of rotations must be alternate. From these assumptions, one can show that either the clockwise or counterclockwise rotations appear in more annuli than the other. Since the rotation of the effective vector potential corresponds to the effective magnetic field, the imbalance of the direction of the vortices induces the nonzero net vorticity, which corresponds to nonzero external magnetic fields. Therefore, the active particles in the circular annuli construct an active-matter counterpart of the quantum Hall effect.

One can also realize counterparts of the quantum Hall effect by using curved spaces [207] or self-rotating active particles [125, 208]. On curved spaces such as a sphere, active matter can exhibit cyclic steady flow along the surface. Then, such steady flow has nonzero vorticity, which induces effective magnetic fields, as in the equatorial waves discussed in Sec. 2.4.2. Meanwhile, self-rotating active particles, i.e., chiral active matter can exhibit Collioris-like forces derived from

[*4] We here ignore some dissipative terms. The full linearized equations are written in Ref. [21].

their rotation. Both the Collioris force and the Lorentz force act particles perpendicularly to their velocities, and thus the Collioris-like forces in chiral active matter lead to the effective magnetic field in topological active matter.

In our previous study [206], we proposed an active-matter counterpart of the quantum anomalous Hall effect, which does not require net effective magnetic fields. To realize such topological active matter, we consider active matter moving among pillars that are located at lattice points of a kagome lattice. Then, such pillars can rectify the steady flow (similar rectification is experimentally realized by using bacteria [192]) and thus realize the effective vector potential imitating that in a kagome-lattice model of the quantum anomalous Hall effect [209].

Previous studies [210, 211] have also realized topological edge modes in experiments of active matter. X. Yang *et al.*, [210] utilized robotic active particles that self-rotate by utilizing the attached vibrators. Such robotic rotators exhibit boundary currents, which is predicted in Ref. [125]. The other study [211] utilized neural progenitor cells, which also show the chiral collective motion. Confining neural progenitor cells in a dish, one can observe the chiral flow along the boundary. We can also calculate the power spectrum of the spatio-temporal Fourier transform of the nonlinear dynamics and obtain gapless dispersions which indicate the existence of topological edge modes. They also derive the linearized equation from the hydrodynamic model of cells, which can be considered as active nematics and have different symmetries from the Toner-Tu equation. Such analysis revealed the topological origin of the chiral edge modes similar to that in the self-rotating polar active matter [208].

Non-Hermitian effects in topological active matter have also been investigated. An experimental study [212] demonstrated that active matter in two-dimensional channels can exhibit the higher-order non-Hermitian skin effect, which is the localization to the corner of the system. Specifically, they utilized heart-shaped channels that rectify the unidirectional flow of active particles. The emergence of the non-Hermitian skin effect is also discussed in the experimental study on neural progenitor cells [211]. In our previous study on the exceptional edge modes [27], we also proposed the active-matter realization of the exceptional edge modes. There, we discussed that the mixture of clockwise and counterclockwise self-rotating particles can exhibit exceptional edge modes.

2.4.7 Stochastic processes

In classical mesoscopic systems, particles are often affected by thermal noises, which induce their Brownian motion. Such noisy systems are modeled by stochastic processes. Focusing on the dynamics of the probability distribution, one can describe the stochastic dynamics by the Fokker-Planck equation or the master equation, which is a linear equation of the probability distribution. In general, the master equation can be written as

$$\partial_t \boldsymbol{p} = W\boldsymbol{p}, \tag{2.53}$$

with $\boldsymbol{p}$ being the vector of the probability distribution and W being the rate matrix. From this equation, one can make an analogy to the Schrödinger equation by corresponding iW to the Hamiltonian H.

Since the steady state of a stochastic process corresponds to the zero eigenvector of the rate matrix W, it is desirable to define the topology around zero eigenvalue. However, the rate matrix is always gapless at the zero point, which is guaranteed by the Perron Frobenius theorem [213,214]. Therefore, one cannot directly extend the topological invariants, such as the winding number and the Chern number. Instead, recent studies [124, 126] proposed to utilize the scale transformation of the rate matrix. By using such scale transformation, one can obtain spectra that do not include the zero eigenvalue. Then, the winding number of eigenvalues that are studied in the non-Hermitian topology is extended to one-dimensional stochastic processes. The nonzero winding number corresponds to the localization of the steady state [124, 125]. Furthermore, the winding number also corresponds to the relaxation properties [126], such as the size-scaling of the relaxation

time and the emergence of the cutoff phenomena [215–218], where the relaxation does not proceed for a long time, and then the system is suddenly relaxed to the steady state.

Exploring the topology in stochastic processes at nonzero eigenvalues, one can further observe topology-induced phenomena. Early works on the topology in stochastic processes [219] discussed the extension of the Thouless pump. they concluded that the zero temperature and the adiabatic limit can reproduce the quantization of the transport. Recent studies [220,221] have also discussed the emergence of the chiral current, which resembles to those in topological insulators. Such chiral current is realized by the stochastic version of a higher-order topological insulator with nonreciprocal hoppings.

2.4.8 Others

Classical topological insulators can be also found in thermal dissipation. The dissipation of heat is described by the diffusion equation and its diffusion coefficient can be tuned by the media. Then, the periodic modulation of the diffusion coefficient can construct counterparts of typical models of topological insulators such as the SSH model [222, 223]. Since the topological edge modes have their eigenvalues in the bulk band gap, one can observe the topological property from the difference in the diffusion rate; edge-localized heat can dissipate faster in topological systems than in trivial systems. Such topological dissipation has also been observed in experiments [224].

Furthermore, the notion of topology can influence human dynamics. Specifically, a previous study [225] has shown that one can choreograph a dance that simulates the edge current in topological insulators. Such a dance can be useful to science education. Extending the notion of topology to these various systems can lead to a wide variety of potential applications, such as engineering and arts.

Chapter 3

Nonlinear dynamical systems and nonlinear topology

In this chapter, we first review examples of nonlinear systems and typical nonlinear phenomena. Then, we review recent studies on the extension of topological physics to nonlinear systems. In Sec. 3.1, we raise examples of nonlinear systems that can be platforms to study nonlinear topology. Specifically, we describe the equations of motion of those nonlinear systems. In Sec. 3.2, we introduce the basic concepts and analytical techniques in studies of nonlinear dynamical systems. In Sec. 3.3, we consider three typical nonlinear phenomena, synchronization, solitons, and chaos, and analytical tools to investigate these phenomena. Finally, we review topological phenomena unique to nonlinear systems in Sec. 3.4. We also introduce recent attempts to extend the topological invariant to nonlinear systems.

3.1 Examples of nonlinear systems

In this section, we review typical nonlinear systems. In particular, we introduce nonlinear oscillators, photonics, ultracold atoms, and (active) fluids.

3.1.1 Nonlinear oscillators

Nonlinear oscillators can be seen in various fields of science including biological systems [30–33] and engineering [34–36, 226–228]. The nonlinear oscillator sustains its self-oscillation at the balance of the injection and dissipation of energy from the circumstances. Therefore, the nonlinear oscillators exhibit unique properties that cannot be seen in linear harmonic oscillators, such as the robustness of the amplitude against external noises.

Typical examples of nonlinear oscillators are found in biological systems. For example, neurons can be modeled as nonlinear oscillators [32, 229]. The change of the action potential of a neuron exhibits a pulse-like oscillation, which is not realized by a linear oscillator. Since the collective dynamics of neurons is important to understand brain activities, nonlinear oscillators imitating neurons are often studied. Another biological example can be found in more macroscopic systems, the luminescence of a firefly [30]. Some kinds of fireflies exhibit periodic luminescence and such oscillations can be regarded as nonlinear oscillators.

Experimental studies of nonlinear oscillators have also been conducted in various setups. Metronomes are nonlinear oscillators that are useful in experimental studies due to their controllability of the frequencies and interactions [35, 230]. Chemical compounds are also useful nonlinear oscillators that are often used in demonstration in scientific events. In particular, the Belousov-Zhabotinsky reaction exhibits complex oscillatory patterns, which have attracted much interest both in the fundamental theory of nonlinear science and physical education. More surprisingly, recent experimental studies [231, 232] have also extended nonlinear oscillators into quantum regimes by using trapped ions.

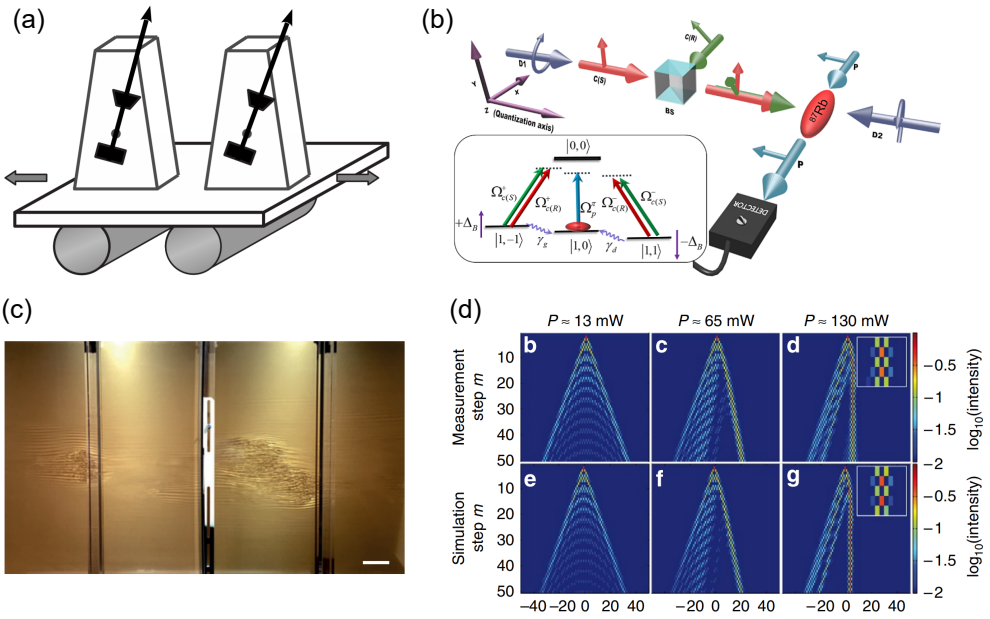

Figure 3.1: Examples of nonlinear systems and phenomena. (a) Schematic of synchronization in metronomes. Reprinted from H. Ulrichs, A. Mann, and U. Parlitz, Synchronization and chaotic dynamics of coupled mechanical metronomes. Chaos **19,** 043120 (2009) [230], with the permission of AIP Publishing. (b) Nonlinear oscillators in quantum physics. Trapped ions can behave as nonlinear oscillators. This figure is adapted from A. W. Laskar, P. Adhikary, S. Mondal, P. Katiyar, S. Vinjanampathy, and S. Ghosh, Observation of Quantum Phase Synchronization in Spin-1 Atoms. Phys. Rev. Lett. **125,** 013601 (2020) [232]. Copyright 2020 by the American Physical Society. (c) Experimental demonstration of the transition to turbulence. This figure is adapted from M. Sano and K. Tamai, A universal transition to turbulence in channel flow. Nat. Phys. **12,** 249-253 (2016) [278], Springer Nature. Copyright 2016. (d) Solitons in a photonic system. The colors of data points show the intensities of light at corresponding sites and times. One can see the propagation of localized waves. This figure is adapted from M. Wimmer *et al.*, Observation of optical solitons in PT-symmetric lattices. Nat. Commun. **6,** 7782 (2015) [241] licensed under a Creative Commons Attribution 4.0 International License (http://creativecommons.org/licenses/by/4.0/).

Models of nonlinear oscillators

One of the simple models of nonlinear oscillators is the Stuart-Landau oscillator [233]. One can describe the Stuart-Landau oscillator by using a complex-valued state variable Z as

$$\dot{Z} = (i\omega + \alpha - \beta|Z|^2)Z, \tag{3.1}$$

where ω and α are real parameters, and β is a complex-valued coefficient of the nonlinear term. This model has a circular limit cycle (cf. Sec. 3.2.1) at $\alpha > 0$, which has the constant amplitude $\sqrt{\alpha/\mathrm{Re}\,\beta}$ and the frequency $\omega + \alpha(\mathrm{Im}\,\beta/\mathrm{Re}\,\beta)$. Thus, the Stuart-Landau oscillator can model a nonlinear oscillator that self-sustains its oscillation. As we will discuss later in Sec. 3.2.2, we can generally obtain this equation by considering leading-order terms of various models of nonlinear oscillators around the parameter where the nonlinear oscillator begins to self-oscillate.

The essential feature of nonlinear oscillators is the self-sustained rotation of the phase with nonzero amplitudes. By extracting such a rotation of the phase, one can define the simplest model of nonlinear oscillators, the Kuramoto model [234,235]. In the Kuramoto model, the state variable ϕ corresponds to the phase of an oscillator that is equated modulo 2π, and its dynamics is simply defined by

$$\dot{\phi} = \omega, \tag{3.2}$$

where ω is the natural frequency of the oscillator. The Kuramoto model was first introduced to analyze the synchronization of oscillators (see Sec. 3.3.1) and the collective motion of the

Kuramoto oscillators can be described as

$$\dot{\phi}_j = \omega_j + \sum_k F_j(\phi_j, \phi_k), \tag{3.3}$$

where $F_j(\phi_j, \phi_k)$ is a doubly periodic nonlinear function of ϕ_j and ϕ_k whose periods are 2π. In particular, $F_j(\phi_j, \phi_k) = K \sin(\phi_k - \phi_j)$ is often used, which represents the attractive interaction in the case of $K > 0$.

There are more types of oscillator models, which can be more suitable to study realistic nonlinear oscillators. Van der Pol [236] proposed the nonlinear equation that models the oscillation found in an electrical circuit using vacuum tubes, which was used in radio. The van der Pol equation is described as

$$\ddot{x} + \mu(x^2 - 1)\dot{x} + x = 0, \tag{3.4}$$

with x being the state variable and $\mu \geq 0$ determines the strength of (nonlinear) dissipation. The nonlinear dissipation term $\mu(x^2 - 1)\dot{x}$ represents the property of the vacuum tubes; they act as a normal resistor at sufficiently large current, while they inject energy if the current is small. In general, the van der Pol circuit can appear in electrical circuits with nonlinear resistors. In addition, recent research [49, 237] has discussed that the dynamics of active particles can be described by the van der Pol equation.

The spikes of neurons are typical nonlinear oscillators that have attracted much interest due to their biological importance. The pioneering model to study such neuron activities is the Hodgkin-Huxley model [229], which models the time-evolution of action potentials by a nonlinear electrical circuit. While this model is much simpler than the set of the rate equations of ions involved in the spikes of neurons, it still has four variables and thus is difficult to analyze. Further simplifying the Hodgkin-Huxley model, one can obtain the Fitzhugh-Nagumo model

$$\dot{u} = c(u - u^3/3 - w), \tag{3.5}$$

$$c\dot{w} = -u - bw + a, \tag{3.6}$$

where u and w are the state variables. Since this model is two-dimensional nonlinear dynamics, one can easily extract the essential properties of the spikes of neurons. We note that the Fitzhugh-Nagumo model also includes the van der Pol oscillator as a special case at $a = b = 0$.

3.1.2 Nonlinear photonics

As discussed in Sec. 2.4.1, photonic systems are described by the Maxwell equations in materials. To be more precise, we obtain from the Maxwell equation,

$$\nabla \cdot (\epsilon_0 \mathbf{E} + \mathbf{P}) = 0 \tag{3.7}$$

where $\mathbf{E}$ and $\mathbf{P}$ are the electric field and the polarlization. We often approximate the polarization $\mathbf{P}$ by the linear function of $\mathbf{E}$, the polarization can be nonlinear for the electric field in realistic materials. Such nonlinear polarization can be described as

$$\mathbf{P} = \epsilon_0(\chi^{(1)}\mathbf{E} + \chi^{(2)}\mathbf{E}^2 + \chi^{(3)}\mathbf{E}^3 + \cdots). \tag{3.8}$$

This nonlinearity is the origin of the nonlinear optical effects in photonic metamaterials.

From the microscopic point of view, the nonlinearity of the polarization is related to the many-body interactions between photons and electrons in materials. In particular, if the numbers of photons absorbed in and emitted from the electronic band structure are different, such absorption and emission processes are regarded as inherently many-body processes, whose probability depends on the number of photons, i.e., the strength of the electric field. Therefore, the nonlinearity of the polarization can be observed.

Under the inversion symmetry, the second-order term in Eq. (3.8) must disappear, and the third-order term is the leading-order term. Such a third-order nonlinear effect is known as the Kerr

nonlinearity [37]. The Kerr nonlinearity induces the inhomogeneity of the refractive index, which can lead to the self-focusing effect of light. Self-focusing of light leads to a pulse-like standing wave of light, which resembles solitons [240, 241]. As we will discuss in Sec. 3.4.1, the interplay between such photonic solitons and topological photonics is much investigated in both theoretical and experimental studies. We note that the emergence of the soliton depends on the sign of the Kerr nonlinear term, and both the positive and negative signs are experimentally realized [242].

3.1.3 Gross-Pitaevskii equation of ultracold atoms

Ultracold atoms are basically quantum bosonic systems and thus are described by the many-body Schrödinger equation. However, such many-body systems are hard to analyze. Instead, by utilizing desirable properties of the BEC state of ultracold atoms, studies on ultracold atoms have derived and analyzed the nonlinear Schrödinger equation of a single particle, which is called the Gross-Pitaevskii equation [40, 41].

We here derive the Gross-Pitaevskii equation from the mean-field approximation of the Hamiltonian of interacting bosonic systems. The Hamiltonian of interacting bosons can be described as

$$H = \sum_i \left[\frac{\mathbf{p}_i^2}{2m} + U(\mathbf{r}_i) \right] + \sum_{i<j} V(\mathbf{r}_i, \mathbf{r}_j), \tag{3.9}$$

where $\mathbf{r}_i$ and $\mathbf{p}_i$ denotes the location and momentum of the ith particle. Then, we assume the following ansatz:

$$\Psi(\mathbf{r}_1, \cdots, \mathbf{r}_N) = \prod_{i=1}^{N} \psi(\mathbf{r}_i). \tag{3.10}$$

This ansatz reflects the fact that the BEC state is a highly coherent state, where almost all the particles are at the ground state and have the same phase. By using this ansatz, the expectation value of the energy becomes

$$\langle \Psi | H | \Psi \rangle = \sum_i \int \psi(\mathbf{r}_i)^* \left[\frac{\mathbf{p}_i^2}{2m} + U(\mathbf{r}_i) \right] \psi(\mathbf{r}_i) d\mathbf{r}_i + \sum_{i<j} \int V(\mathbf{r}_i, \mathbf{r}_j) |\psi(\mathbf{r}_i)|^2 |\psi(\mathbf{r}_j)|^2 d\mathbf{r}_i d\mathbf{r}_j, \tag{3.11}$$

which has a fourth-order term of $\psi(\mathbf{r}_i)$. To derive the nonlinear Schrödinger equation, we should conduct the variational calculation of this equation. Then, we obtain the Gross-Pitaevskii equation

$$E_{\mathrm{MB}} \psi(\mathbf{r}_i) = N \left[\frac{\mathbf{p}^2}{2m} + U(\mathbf{r}_i) \right] \psi(\mathbf{r}_i) + \frac{V' N(N-1)}{2} |\psi(\mathbf{r}_i)|^2 \psi(\mathbf{r}_i), \tag{3.12}$$

where we approximate the interaction $V(\mathbf{r}_i, \mathbf{r}_j)$ by the delta function, $V(\mathbf{r}_i, \mathbf{r}_j) = V' \delta(\mathbf{r}_i - \mathbf{r}_j)$.

3.1.4 Passive and active fluids

While we have discussed the topological edge modes in fluidic or phononic systems in Sec. 2.4.2, the hydrodynamic equation is a typical example of nonlinear dynamics. The well-known hydrodynamic equation, the Navier-Stokes equation (cf. Sec. 2.4.2),

$$\partial_t \rho + \nabla \cdot (\rho \mathbf{v}) = 0, \tag{3.13}$$

$$\partial_t \mathbf{v} + (\mathbf{v} \cdot \nabla) \mathbf{v} = -\frac{1}{\rho} \nabla P + D \nabla^2 \mathbf{v} + \mathbf{f}, \tag{3.14}$$

where ρ and $\mathbf{v}$ are the density and the velocity field, P is the pressure and $\mathbf{f}$ represents the external force. As we can see from this equation, the hydrodynamics exhibits the nonlinearity in, e.g., its space-derivative terms. In particular, when the dynamics cannot be regarded as laminar flow, one cannot ignore such a nonlinearity. Therefore, we must investigate the nonlinear effect on topological fluid and phononics.

The dynamics of active matter that has been discussed in Sec. 2.4.6 is also described by the hydrodynamic equation. The representative hydrodynamic model of active matter is the Toner-Tu model [203, 204],

$$\partial_t \rho + \nabla \cdot (\rho \mathbf{v}) = 0, \tag{3.15}$$

$$\begin{aligned} & \partial_t \mathbf{v} + \lambda(\mathbf{v}\cdot\nabla)\mathbf{v} + \lambda_2(\nabla\cdot\mathbf{v})\mathbf{v} + \lambda_3\nabla|\mathbf{v}|^2 \\ = \; & (\alpha - \beta|\mathbf{v}|^2)\mathbf{v} - \nabla P + D_B\nabla(\nabla\cdot\mathbf{v}) + D_T\nabla^2\mathbf{v} + D_2(\mathbf{v}\cdot\nabla)^2\mathbf{v} + \mathbf{f}. \end{aligned} \tag{3.16}$$

Comparing this with the Navier-Stokes equation (3.13), (3.14), the Toner-Tu model uniquely has a dissipative nonlinear term $-\beta|\mathbf{v}|^2\mathbf{v}$, which is originated from the injection and dissipation of energy in active systems. Therefore, the nonlinearity of active matter is nonnegligible in a wider range of parameters than those in passive fluids. The nonlinearity of active matter plays an important role in its phase transition from a disordered state to a flocking state (i.e., collective motion such as a school of fish). Strong nonlinear effects in active matter also induce active turbulence [191], which can be seen even in low-Raynolds-number regimes.

3.1.5 Others

Nonlinearity can be found in more familiar examples such as mechanical systems. For example, if the mass is constrained on a circular path (cf. a pendulum), the Newton equation becomes nonlinear for the location of the mass. The mechanical lattice discussed in Sec. 2.4.3 also exhibits such nonlinearity. Thus, the nonlinear effect in topological mechanics has also been studied both theoretically [243] and experimentally [244].

Another interesting example of nonlinear systems is a chemical reaction. Since the rate equation is a nonlinear equation of the concentrations of chemical species, one can assume the dynamics of a chemical reaction network as a nonlinear system. Recently, chemical reactions have attracted interest in nonequilibrium thermodynamics [245, 246] because similar inequalities can be obtained to those found in master equations of stochastic systems. Since topological properties have been investigated in master equations (cf. Sec. 2.4.7 and Refs. [124–126, 219–221]), one may also find counterparts of topological insulators in chemical reaction networks. We note that some previous studies [247, 248] have analyzed the robustness of chemical reaction networks from the view of network topology, which is different from the topology of the wavenumber space discussed in this thesis.

3.2 Introduction to nonlinear dynamical systems

In this section, we introduce the basic concepts in nonlinear dynamical systems that are necessary to understand the bulk-boundary correspondence in nonlinear systems. There are good textbooks [249, 250] to learn these basic concepts in nonlinear dynamical systems, and thus one should consult them to know the details.

3.2.1 Fixed points and limit cycles

Nonlinear dynamical systems are nonlinear time evolutions including both continuous and discrete ones. Such nonlinear dynamics are generally described as

$$\frac{d}{dt}\mathbf{x} = f(\mathbf{x}) \quad \text{(continuous)}, \tag{3.17}$$

$$\mathbf{x}(t+1) = F(\mathbf{x}(t)) \quad \text{(discrete)}, \tag{3.18}$$

where $\mathbf{x}$ represents a vector of the state variables. As discussed in the previous section, nonlinear dynamical systems are abundant in nature and thus attract much interest in mathematics and physics.

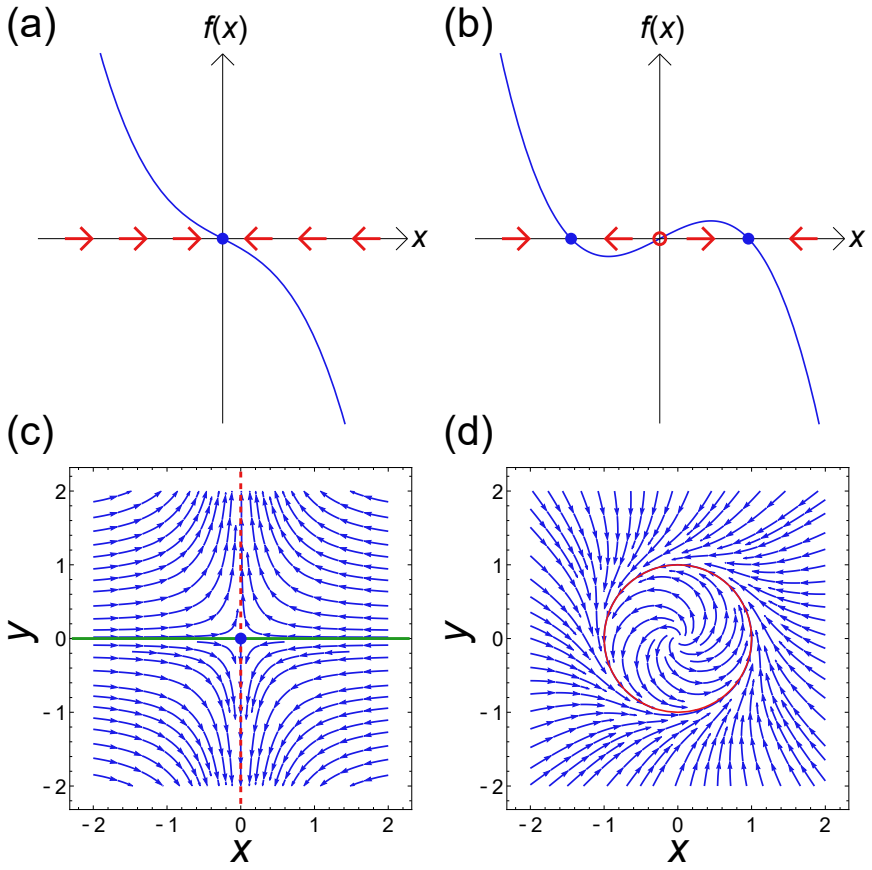

Figure 3.2: Vector fields and stability analyses. (a,b) Vector fields and pitchfork bifurcation of a one-dimensional system. The blue curves represent $f(x) = ax - x^3$ with (a) $a = -1$ and (b) $a = 1$, for each. The red arrows show the vector fields of the one-dimensional model, whose directions correspond to the signs of the function $f(x)$. The blue filled circles (the red circle) are the stable (unstable) fixed point. The pitchfork bifurcation occurs at $a = 0$ and new fixed points appear. (c) Vector field of a two-dimensional model (3.23). The blue curved arrows represent the vector field. There exists the saddle point at $(x, y) = (0, 0)$ denoted by the blue circle. The green line is the stable manifold of the fixed point, and the red dashed line is the unstable manifold. (d) Vector field of the Stuart-Landau model (3.1). We rewrite the complex state variable as $Z = x + iy$. We use the parameters $\alpha = \beta = \omega = 1$. The red circle is the limit cycle of this model.

One of the purposes of studies on nonlinear dynamical systems is to understand the geometrical properties of the state in the long time limit $t \to \infty$. If a nonlinear system is dissipative and has no conservative quantities, the dynamics should be relaxed to a steady state. There are two types of typical steady states, fixed points and limit cycles. In the following paragraph, we describe their definitions and basic properties.

First, let us consider fixed points. A fixed point is a point in the phase space at which the state variables do not change under the time evolution. By using Eqs. (3.17) and (3.18), one can define the fixed point $\mathbf{x}^*$ as

$$f(\mathbf{x}^*) = 0 \quad \text{(continuous)}, \tag{3.19}$$

$$F(\mathbf{x}^*(t)) = \mathbf{x}^*(t) \quad \text{(discrete)}. \tag{3.20}$$

The fixed points are classified by their stability. If any neighbor points approach the fixed point, it is called a stable fixed point or a sink. Otherwise, the fixed point is unstable in most cases. Further considering unstable fixed points, we can find two types; one is a fully unstable point from which any neighbor points are repelled, and the other is the fixed point some neighbor points can converge to it. The former is called a source, and the latter is a saddle point. There are also

exceptional cases that infinitely many oscillatory steady states appear around a fixed point, which is called a center.

Secondly, we consider the limit cycle, which is an isolated closed orbit. One mathematically defines the limit cycle as a closed orbit γ such that there exists a neighborhood U of γ and orbits starting from any points in U approaches γ in the limit of $t \to \infty$ or $t \to -\infty$. One can also classify the limit cycles from their stabilities as in the fixed points. We note that stable fixed points and stable limit cycles are also called attractors, which is the term including any sets of points whose neighbor points coverge.

We note that there can be more exotic steady states. Specifically, the strange attractor in chaotic systems is one example (see Sec. 3.3.2). However, the analysis of such nonperiodic steady states is much more difficult than fixed points and limit cycles.

Vector fields to analyze the stability

Since most nonlinear differential eqautions cannot be analytically solved, geometrical approaches are useful to analyze nonlinear dynamical systems. One of such geometrical approaches is a vector field, which visualizes the flow of the nonlinear dynamics. The vector field is defined as $f(\mathbf{x})$ of Eq. (3.17) in the phase space. By plotting the vector field as arrows, one can judge the stability or instability of fixed points and limit cycles.

We here raise an example of the stability analysis using the vector field in a one-dimensional dynamical system $\dot{x} = f(x)$. Figures 3.2(a) and (b) show the vector fields of such a one-dimensional dynamical system. The points at which the directions of the arrows are changed are the fixed points. One can clearly see the stability and instability of the fixed points from the directions of the arrows; if the neighbor arrows point out the fixed point, it is stable and otherwise unstable. Therefore, one can judge the stability of the fixed points without solving the differential equation.

Stable and unstable manifolds

The stability of the fixed point is judged by whether or not its neighbor points converge to the fixed point in the limit of $t \to \infty$. Thus, the set of points that converge to a fixed point also plays important roles in the analysis of the dynamical system. In fact, such a set of points is termed a *stable manifold*. More rigorously, one defines the stable manifold of a fixed point $\mathbf{x}^*$ as

$$\{\mathbf{x}' | \text{if } \mathbf{x}(0) = \mathbf{x}', \lim_{t\to\infty} \mathbf{x} = \mathbf{x}^*\}. \tag{3.21}$$

In addition, the set of points that converge to a fixed point in the limit of $t \to -\infty$,

$$\{\mathbf{x}' | \text{if } \mathbf{x}(0) = \mathbf{x}', \lim_{t\to-\infty} \mathbf{x} = \mathbf{x}^*\}, \tag{3.22}$$

has also important meanings in nonlinear dynamical systems and is termed an *unstable manifold*.

One can judge the stability of a fixed point from the dimension of the stable and unstable manifolds. For example, if the dimension of the stable manifold is the same as the dimension of the phase space, the fixed point is stable (i.e., a sink). In contrast, if the dimension of the unstable manifold is the same as the dimension of the phase space, the fixed point is a source. In the other cases, one can judge that the fixed point is a saddle point. Therefore, the stable and unstable manifolds provide us the information directly related to the stability of the fixed point. We present an example of the vector field in Fig. 3.2(c). We here consider a two-dimensional dynamical system

$$\dot{x} = -x - x^3, \quad \dot{y} = y. \tag{3.23}$$

We obtain a one-dimensional stable manifold of the fixed point at $(x, y) = (0, 0)$. Thus, we can judge that the fixed point is a saddle point.

While the stable and unstable manifolds are directly related to the stability of a fixed point, the linear stability analysis is also useful to investigate the stability of a fixed point. In fact, these

two methods have a close relation in that the dimensions of the stable and unstable manifolds of a normal fixed point become equal to the numbers of negative and positive eigenvalues obtained from the linear stability analysis, respectively. In more detail, the normal fixed point means that all the eigenvalues have nonzero real parts in the linear stability analysis around the fixed point. Such a fixed point is called hyperbolic. Then, one can obtain the linear subspace whose basis is the eigenvectors with negative (positive) real parts of the eigenvalues, which is called a stable (unstable) linear subspace. Finally, the Hartman-Grobman theorem [251,252] indicates that local structures of the orbits around the stable point and that in linear dynamics are topologically conjugate (they have similar structures in a topological sense). Therefore, the dimension of the stable (unstable) manifold is equal to that of the stable (unstable) linear subspace, which is also the same as the number of negative (positive) real parts of the eigenvalues in the linear stability analysis.

3.2.2 Bifurcation analysis

Since the existence and stability of fixed points and limit cycles play important roles, the change of them also attracts much interest in studies on nonlinear dynamical systems. Such changes in the existence and stability of fixed points and limit cycles are called bifurcations. In this section, we raise some typical examples of bifurcations.

We first consider fixed points and discuss two types of bifurcations, pitchfork bifurcations and saddle-node bifurcations. At the pitchfork bifurcation, a fixed point splits into three fixed points. Such a bifurcation can be seen in a nonlinear dynamics described by

$$\dot{x} = ax - x^3. \tag{3.24}$$

In this nonlinear dynamics, there is one fixed point at $x = 0$ for $a < 0$. Meanwhile, at $a = 0$, the pitchfork bifurcation occurs, and three fixed points $x = 0, \pm\sqrt{a}$ emerge in the parameter region, $a > 0$. We note that the pitchfork bifurcation alters the stability of the fixed point at $x = 0$ (stable at $x < 0$ and unstable at $a > 0$). Such a change in the stability of the fixed point is also universal in the pitchfork bifurcation. Another type of pitchfork bifurcation can be seen in

$$\dot{x} = ax + x^3, \tag{3.25}$$

where the stabilities of the fixed points are different from those in Eq. (3.24).

One can also observe a saddle-node bifurcation in any dimension. At the saddle-node bifurcation, two fixed points emerge. One can check the saddle-node bifurcation in a nonlinear dynamics

$$\dot{x} = a + x^2. \tag{3.26}$$

If one considers $a > 0$, the nonlinear dynamical system has no fixed points. At $a = 0$, the saddle-node bifurcation occurs, and one obtains two fixed points $\pm\sqrt{-a}$ at $a < 0$.

We note that Equations (3.24), (3.25), and (3.26) are called normal forms of the bifurcations. In general nonlinear dynamics, if we consider the leading-order terms around the bifurcation point, one obtains these normal forms. Therefore, analyzing the normal forms is useful to understand the properties of each type of bifurcation.

We next consider the bifurcation involving limit cycles. One typical example is a supercritical Hopf bifurcation, where a stable limit cycle emerges around a fixed point. The normal form of the supercritical Hopf bifurcation is

$$\dot{x} = \alpha x - \omega y - (x^2 + y^2)x, \tag{3.27}$$

$$\dot{y} = \alpha y + \omega x - (x^2 + y^2)y. \tag{3.28}$$

If one considers $\alpha < 0$, the nonlinear system exhibits one fixed point at $(x, y) = (0, 0)$ and no limit cycles. At $\alpha = 0$, the supercritical Hopf bifurcation occurs and $(x, y) = (\sqrt{\alpha}\cos\omega t, \sqrt{\alpha}\sin\omega t)$ is a stable limit cycle at $\alpha > 0$. We note that the normal form of the supercritical Hopf bifurcation

is equivalent to the Stuart-Landau equation (Eq. (3.1) in Sec. 3.1.1) via the transformation of the variables $Z = x + iy$. Since the supercritical Hopf bifurcation indicates the beginning of the self-oscillations of nonlinear oscillators, the Stuart-Landau equation can approximate the general dynamics of nonlinear oscillators at the parameter where the oscillation amplitudes are small enough. While we have considered a supercritical Hopf bifurcation, nonlinear dynamics can also exhibit a subcritical Hopf bifurcation, where an unstable limit cycle emerges.

It is noteworthy that there are more various bifurcations than those introduced in this section. Raising a few examples, fixed points can exhibit a transcritical bifurcation where the stability of two fixed points are swapped, and a coalesce of a saddle point and a limit cycle induces a homoclinic bifurcation. Discrete dynamical systems further enrich the types of bifurcations, such as a period-doubling bifurcation, which we will discuss in Sec. 3.3.2. Understanding which types of bifurcations occur is a key issue in studies of nonlinear dynamical systems.

Index theory in nonlinear dynamical systems

While studies on the quantum field theory have revealed the index theorems related to the bulk-boundary correspondence in topological insulators, nonlinear dynamical systems can also be analyzed from a view of topological indices that are different from quantum physics [253, 254]. Specifically, one can consider the following winding number [249] on a closed path C in the vector field of a two-dimensional nonlinear dynamical system $\dot{x} = f(x, y)$, $\dot{y} = g(x, y)$,

$$\nu_C = \frac{1}{2\pi} \oint_C \frac{f dg - g df}{f^2 + g^2}, \tag{3.29}$$

which counts how many times the angle of the vector field rotates. One can show that this winding number is an integer and continuous with respect to f and g. Therefore, ν_C is a topological invariant and is also unchanged under the deformation of the closed path C, until C does not cross fixed points.

Since the winding number ν_C is a topological invariant, one can calculate it from the sum of the local winding number around the fixed points encircled by C. The winding number around a fixed point is determined from the type of stability of the fixed point; if the fixed point is a sink or a source, the winding number becomes $\nu_C = 1$. If the fixed point is a saddle point, we obtain $\nu_C = -1$. These facts also restrict the possible types of bifurcations, because the winding number is also unchanged via the bifurcation. For example, in the pitchfork bifurcation, a sink does not split into a pair of sinks and a source, because the winding number is changed from $C = 1$ to $C = 3$ via such a bifurcation.

Unfortunately, the relationship between the index theory in nonlinear dynamical systems and nonlinear topology in condensed matter theory is unelucidated. In Sec. 6, we instead discuss the relationship between the stability of fixed points and nonlinear topological invariants characterizing nonlinear topological insulators. Since the winding number above is a well-investigated quantity in nonlinear dynamical systems, analyzing the nonlinear topology from the winding number of the vector field might open up a different way to establish the bulk-boundary correspondence from that in our studies.

3.3 Typical nonlinear phenomena

In this section, we review two nonlinear phenomena, synchronization and chaos, which play important roles in our studies on the nonlinear topology. We also briefly introduce other typical nonlinear phenomena, solitons and pattern formations.

3.3.1 Synchronization

One of the intriguing nonlinear phenomena is synchronization [235], which can ubiquitously appear in various types of nonlinear oscillators. Synchronization of nonlinear oscillators is defined as

a collective motion of (inhomogeneous) oscillators by their interactions. Synchronization can be classified into two classes, phase synchronization and frequency synchronization. In the phase synchronization, nonlinear oscillators exhibit almost the same phase. The frequency synchronization indicates a wider class of synchronization, where the frequencies of the oscillators are the same, while their phases can be different. Both types of synchronizations can occur even if the natural frequencies of oscillators fluctuate. We also note that coupled linear harmonic oscillators usually exhibit multi-frequency oscillations, a single-frequency collective motion is inherent to nonlinear systems.

Synchronization plays crucial roles in various physical systems. A typical example of synchronization is the flashing of fireflies [30]. Some kinds of fireflies show synchronous flashing and it is modeled as nonlinear oscillators. Synchronization can also be seen in other biological systems, such as the collective motion of cardiomyocytes [31], circadian rhythm [33], and neural activity [32]. While these biological oscillators are constituted of complex networks of biochemical reactions, one can also realize synchronization of chemical oscillators in more simple systems [255]. One can also realize the synchronization in artificial systems, including mechanical oscillators (e.g., metronomes) [35, 230], Josephson junction arrays [34], and lasers [226–228]. Stabilizing the synchronization is required in engineering, for example, to maintain a grid system by realizing the stable synchronization of electric generators [36]. While conventional studies of synchronization have focused on classical systems, recent studies have also revealed the synchronization in quantum systems such as trapped ions [231, 232].

As discussed in Sec. 3.1.1, the Kuramoto model [234, 235], the simplest model of nonlinear oscillators, was introduced to analyze the synchronization of nonlinear oscillators. Specifically, one can exactly show the transition from synchronized to disordered phases in the fully connected Kuramoto model,

$$\dot{\theta}_i = \omega_i + \frac{K}{N}\sum_j \sin(\theta_j - \theta_i). \tag{3.30}$$

To show such a phase transition, one should consider the order parameter R defined as

$$\frac{1}{N}\sum_j \exp(i\theta_j) = R\exp(i\Theta), \tag{3.31}$$

where Θ represents a kind of the averaged phase of oscillators. By substituting this to Eq. (3.30), one obtains

$$\dot{\theta}_i = \omega_i + KR\sum_j \sin(\Theta - \theta_i). \tag{3.32}$$

Finally, by self-consistently solving this equation, one can exactly confirm the phase transition in this model.

While one can solve the fully connected Kuramoto model, the network structures of realistic coupled nonlinear oscillators are more complex. There are many studies on the synchronization of nonlinear oscillators on periodic [256–260] and aperiodic [261, 262] networks. These network structures enrich the synchronized phase, such as cluster synchronization [263–265] where the nonlinear oscillators are divided into several synchronous groups that oscillate in different frequencies from the others.

Further complex synchronous behaviors can be seen in the chimera state [266]. The defining feature of the chimera state is the coexistence of synchronized and desynchronized oscillators in a homogeneous oscillator system. The chimera state is named after a creature that appears in Greek mythology and has the body of a lion and the head of a goat, whose complex features may remind us of the coexistence of synchronization and desynchronization. The chimera state was first found in one-dimensional lattice systems with long-range couplings [258, 259]. After those groundbreaking works, the chimera states are also investigated in two or more dimensions [260] and lattice systems only with short-range couplings [267, 268]. Furthermore, previous studies have also experimentally realized the chimera states in, e.g., chemical oscillators [269, 270], liquid-crystal spatial light modulators [271], and metronomes [272]. The chimera states are not only of

theoretical interest but also of potential medical importance because they can play essential roles in neural activities and be related to Parkinson's disease [273]. One can understand the mechanism of the chimera state by considering local order parameters similar to Eq. (3.31). In the chimera state, the local order parameters exhibit a spontaneous symmetry breaking of the translational symmetry due to the inhomogeneity of the initial condition and have different values depending on the location. Then, the large local order parameter strengthens the synchronization, while the small one leads to the destabilizing of the synchronized state, which induces the separation of the synchronized and desynchronized oscillators, i.e., the chimera state.

Since nonlinear oscillators are often affected by external noises from their circumstance, the robust control of the synchronization [274–276] is required to stabilize their functionality. In Chapter 4, we focus on the robustness of topological properties against disorders and propose the topological control of synchronization.

3.3.2 Chaos

Chaos is also a ubiquitous phenomenon found throughout nonlinear systems [249, 250]. The defining feature of the chaos is the high sensitivity to the initial condition. Thus, a chaotic system exhibits bounded orbits, while the orbits obtained from slightly different initial conditions behave differently in the long-time regime. Such sensitivity to the initial condition prevents us from precisely predicting the chaotic dynamics. Unfortunately, such chaotic motions are found throughout nature, such as turbulence [277, 278] of the atmosphere. Therefore, the chaos has attracted much interest in nonlinear physics. However, since condensed matter physics mainly focuses on the linear Schrödinger equation, the role of chaos in condensed matter physics is little understood.

From the point of view of attractors, chaotic systems exhibit unconventional attractors, which are named strange attractors. Such strange attractors are not points or periodic orbits and thus are different from both fixed points and limit cycles. Furthermore, strange attractors have fractal structures. Therefore, the dimensions of such attractors can be nonintegers as we will discuss below. In the following subsections, we introduce an analytical technique to measure the chaos of dynamics, named the Lyapunov analysis, and discuss the chaos transition in a one-dimensional discrete dynamical system, which is closely related to our result in Sec. 6.

Lyapunov analysis

As an indicator of the chaos, the Lyapunov exponent [279] is widely used. The Lyapunov exponent corresponds to the rate of amplification or attenuation of the deviation of the orbits from original and perturbed initial conditions. Denoting the deviation of orbits at the time t by $\boldsymbol{\delta}(t)$, the Lyapunov exponent is defined as

$$|\boldsymbol{\delta}(t)| \sim |\boldsymbol{\delta}(0)|e^{\lambda t}. \tag{3.33}$$

The positivity (negativity) of the Lyapunov exponent indicates the amplification (attenuation) of the deviation of the orbits. Therefore, the positive Lyapunov exponent implies the chaos of the system (more strictly, we need a bounded orbit to judge the chaos of the dynamics). When we consider a multi-dimensional dynamical system, the rate of amplification or attenuation can be different. Therefore, one can obtain several Lyapunov exponents whose number is equal to the dimension of the phase space. In multi-dimensional cases, the positivity of the largest Lyapunov exponent implies chaos.

To investigate the geometric structure of a strange attractor, we also use the (covariant) Lyapunov vectors [280, 281], which correspond to the direction of perturbations whose rates of amplifications or attenuations are equal to the Lyapunov exponents. The covariant Lyapunov vector corresponding to the Lyapunov exponent λ is defined as the vector $\boldsymbol{\delta}(0)$ that is amplified or attenuated as in Eq. (3.33) in the forward time evolution and as

$$|\boldsymbol{\delta}(-t)| \sim |\boldsymbol{\delta}(0)|e^{-\lambda t}, \tag{3.34}$$

in the backward time evolution. The Lyapunov vectors provide us the information on the geometry of a strange attractor, such as the directions in which the attractor is extended. A previous study [282] has utilized the Lyapunov vectors to investigate the chaotic collective motion of nonlinear oscillators and found that the behavior of the Lyapunov vectors depends on the number of nonlinear oscillators involved in the chaotic motion.

By using the Lyapunov exponents, we can also calculate the Lyapunov dimension [283] of the strange attractor, which approximates the fractal dimension of the attractor. To calculate the Lyapunov dimension, one should first sort the Lyapunov exponents λ_i in descending order. Then, the Lyapunov dimension becomes

$$D_{\mathrm{L}} = \frac{\sum_{i\leq M}\lambda_i}{|\lambda_{M+1}|} + M, \tag{3.35}$$

where M is the smallest integer that satisfies $\sum_{i\leq M+1}\lambda_i < 0$. Since the Lyapunov dimension almost corresponds to the dimension of the strange attractor, it informs us of the effective degrees of freedom of chaotic dynamics. Specifically, recent studies have revealed the chaos in chimera states [284–287] and their Lyapunov dimensions are close to the degrees of freedom of desynchronized oscillators [284, 287].

In one-dimensional dynamical systems, one can calculate the Lyapunov exponent by using a simple formula. Specifically, in the discrete dynamical system $x(t+1) = f(x(t))$, the Lyapunov exponent is calculated as

$$\lambda = \lim_{T\to\infty}\frac{1}{T}\sum_{t=1}^{T}\log|f'(x(t))|, \tag{3.36}$$

where f' represents the derivative of f. In the continuous dynamical system, one can show that the chaos cannot appear. (In fact, the chaos in continuous systems can be seen in three or more dimensions.) Since a unit vector in a one-dimensional system is unique, the Lyapunov vector is determined without calculations.

The calculations of Lyapunov exponents and vectors become difficult in higher-dimensional systems. While it is almost impossible to analytically obtain the Lyapunov exponents and vectors, numerical algorithms have been established. The algorithm to calculate the Lyapunov exponents was developed by Shimada and Nagashima [288], and its improved version [289,290] is widely used. The calculation of the covariant Lyapunov vectors is more difficult than the Lyapunov exponents and instead, the vectors obtained as the subproducts of the Shimada-Nagashima algorithm were used to approximate them. Recently, Ginelli *et al.* [280] have established a smart algorithm for the calculation of the Lyapunov vectors by modifying the Shimada-Nagashima algorithm.

The basic idea of the Shimada-Nagashima algorithm and the Ginelli algorithm is to simulate the amplification and attenuation of perturbations in all the relevant directions. We here explain how to calculate the Lyapunov exponents and vectors of the N-dimensional dynamical system $\dot{x} = f(x)$ and its orbit $\tilde{x}(t)$. Since the rate of amplification or attenuation of perturbation is obtained from the linearized matrix at each time, we first calculate the values of the Jacobian matrix of $f(x)$ for $\tilde{x}(t)$ at each t_n of the nth data set, $J_n = Jf(\tilde{x}(t_n))$. We prepare N orthogonal vectors $\{g_0^j\}_{j=1,\cdots,N}$. We apply J_n to $\{g_n^j\}_{j=1,\cdots,N}$ and obtain $\{J_n g_n^j\}_{j=1,\cdots,N}$ at each step. Then, we conduct the Gram-Schmidt transformation to the set of $\{J_n g_n^j\}_{j=1,\cdots,N}$ and obtain the next set of N orthogonal vectors $\{g_n^j\}_{j=1,\cdots,N}$. The averages of the logarithms of the rates of amplifications or attenuations of these vectors converge to the Lyapunov exponents. Practically, one can conduct the Gram-Schmidt transformation by the QR decomposition of the matrix whose rows are $\{J_n g_n^j\}_{j=1,\cdots,N}$. Then, if we write the obtained R matrix at the nth step as R_n, the Lyapunov exponents are equal to the time-averaged value of the logarithm of each diagonal element of R_n. To further obtain the Lyapunov vector, we should apply the inverse of R_n to the obtained orthogonal vectors $\{g_n^j\}_{j=1,\cdots,N}$, backward in time. By iterating this vector backward for a sufficiently large number of times, the set of vectors converge to the covariant Lyapunov vectors.

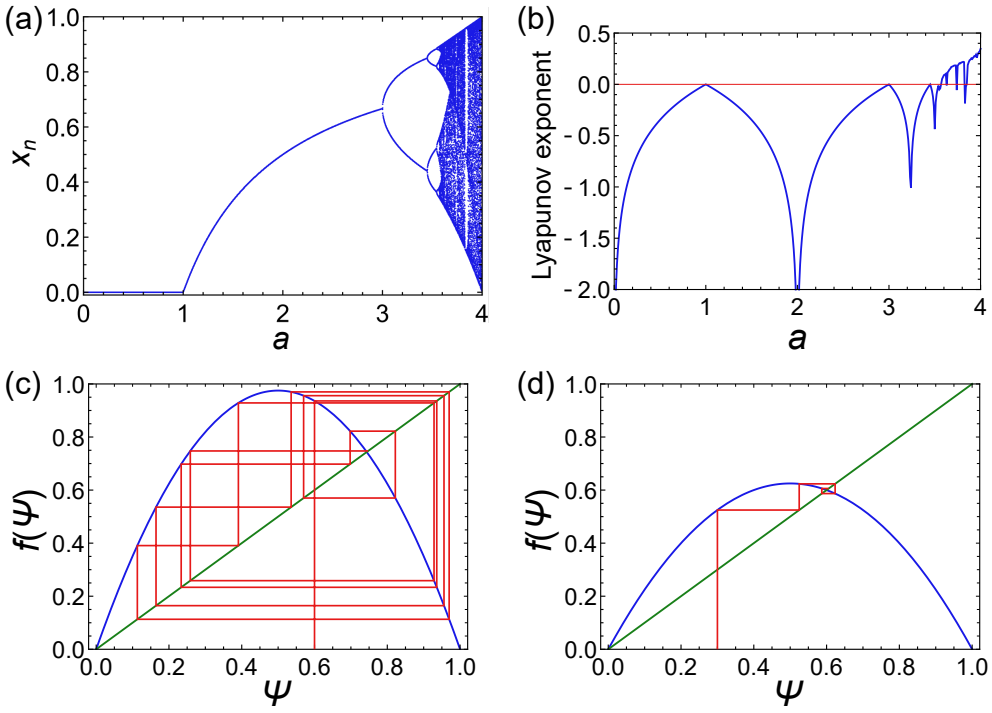

Figure 3.3: Analyses on the logistic map. (a) Bifurcation plot of the logistic map. We plot the absolute values of x_n for sufficiently large n's. We can find the period-doubling bifurcations and chaos transitions. (b) Lyapunov exponents of the logistic map. The red line separates the positive and negative Lyapunov exponents. (c) Cobweb plot at $a = 2.5$. The blue curve corresponds to $y = f(x) = ax(1 - x)$ and the green line corresponds to $y = x$. The red lines show the discrete dynamics of the logistic map. (d) Cobweb plot at $a = 3.9$. We confirm the nonperiodic orbit, which indicates the chaos.

Chaos in a one-dimensional map

Here, we consider the logistic map, which is a typical nonlinear discrete dynamical system exhibiting chaos transition, and show the existence of chaos. We also provide a tool to investigate the chaotic map. We will conduct a similar analysis on zero modes of nonlinear topological insulators in Sec. 6 to investigate the chaos in nonlinear topological edge modes.

The logistic map [42] is a one-dimensional discrete dynamical system, whose dynamics is described as

$$x_{i+1} = ax_i(1 - x_i), \tag{3.37}$$

with x_i being the state variable at the ith step. a is a positive real parameter. If we consider $a \leq 4$ and the initial condition $0 \leq x_1 \leq 1$, x_i always exists in the regime $0 \leq x_i \leq 1$, and thus we obtain nondiverging orbits. However, depending on the parameter a, the logistic map exhibits chaotic orbits that do not diverge but are neither fixed points nor limit cycles.

First, we numerically confirm the emergence of chaos in the logistic map. We start from the initial condition $x_0 = 0.1$ and calculate the discrete dynamics until it is relaxed to a steady state or a chaotic attractor. Figure 3.3(a) shows the values that the state variable takes after the relaxation. In the parameter regime $a < 3$, the logistic map converges to a fixed point. At $a = 3$, a bifurcation occurs, and the steady state becomes a limit cycle with the period $T = 2$. This type of bifurcation is called a period-doubling bifurcation. If we consider larger a, the logistic map exhibits an infinite number of period-doubling bifurcations. As we can see from Fig. 3.3, the distance between the period-doubling bifurcation points becomes smaller as a becomes larger. Finally, the period of the limit cycle becomes infinite at $a \sim 3.57$. At such a, the chaos transition occurs, and we obtain chaotic orbits for larger a. We can also find limit cycles even for $a \gtrsim 3.57$, i.e., period-doubling windows. We can also approximately calculate the Lyapunov exponents by

using the formula (3.36). We here consider the average of $\log|f'(x_i)| = \log|a(1-2x_i)|$ in the regime $5001 \leq i \leq 10000$. Figure 3.3(b) shows the numerically obtained Lyapunov exponents at different a. One can clearly confirm the chaos at $a \gtrsim 3.57$ from the positive Lyapunov exponent in this figure.

To analyze the steady states and their stability in one-dimensional nonlinear maps, one often uses the cobweb plot [249, 250]. We present examples of the cobweb plots of the logistic map in Figs. 3.3(c,d). The procedure to write the cobweb plot is as follows: (1) Draw the vertical line at $\psi_i = \psi_1$ from the bottom to the curve of $f(\psi_i)$. (2) Draw the horizontal line from the cross point of the vertical line and $f(\psi_i)$ to the line representing $f(\psi_i) = \psi_i$. (3) Draw the vertical line from the cross point of the horizontal line and the line of $f(\psi_i) = \psi_i$ to the curve $f(\psi_i)$ (4) Repeat the steps (2) and (3). By using the cobweb plot, one can visualize the dynamics in the nonlinear discrete dynamical system and clearly show that the system exhibits a stable steady state or chaotic dynamics. Figure 3.3 also reflects the chaotic and nonchaotic dynamics. In Fig. 3.3(c), we confirm the convergence to a fixed point which indicates the stability of the fixed point. In contrast, in Fig. 3.3(d), we obtain a disordered orbit, which indicates the chaos of the logistic map.

3.3.3 Other nonlinear phenomena

Nonlinearity induces more various phenomena than those discussed above. One typical example is a soliton [240,241], which is a pulse-like nonlinear wave. Solitons can preserve their shapes after their collision, even though the nonlinear systems have no superposition laws. Such solitons are abundant in nature, such as water surface waves. Solitons are understood from the balance of the dissipation and the self-focusing effect of nonlinear waves. One can obtain solitary solutions from various conservative nonlinear models. In particular, one can analytically calculate the solitary solutions in solvable models such as the Korteweg-de Vries equation [291] and the one-dimensional nonlinear Schrödinger equation.

We note that high-energy physics often discusses topological solitons [292], which are topologically protected solitonic excitations. For example, if we consider a one-dimensional chain of two-dimensional spins such as the sine-Gordon model [293], the $2n\pi$ ($n \in \mathbb{Z}$) rotation of the spins from $x = -\infty$ to $x = \infty$ cannot be continuously deformed to the state without a rotation of the spins. Therefore, such rotated states are metastable states protected by their nontrivial topology[*1]. We would like to emphasize that topological solitons utilize the topology of the real space, which is different from those analyzed in our study, i.e., the topology of the wavenumber space.

Another typical nonlinear phenomenon is pattern formation. Specifically, the Turing patterns [294] have attracted much interest in various fields of science from mathematics to biology. The Turing pattern is induced by the instability of the plane wave with a nonzero wavenumber. It is utilized to explain, e.g., the pattern formation of a tropical fish [295]. To realize the Turing pattern in biochemical systems, one needs two chemical components, inhibitor and promotor. Then, the Turing pattern is induced by the interplays between the dissipations at different rates and the nonlinear interactions of two components.

As discussed below interplays between solitons and topological materials have been explored in various studies. In contrast, the role of topology in pattern formation is much less explored than topological edge solitons and thus remains an intriguing future issue.

3.4 Nonlinear topology

In this section, we review previous studies on the extension of topological insulators to nonlinear systems. As discussed in the previous chapter, conventional studies on topological materials have assumed the linearity of the system. However, recent studies [38, 39, 296, 297] have revealed

[*1] One can define the winding number characterizing the metastable states

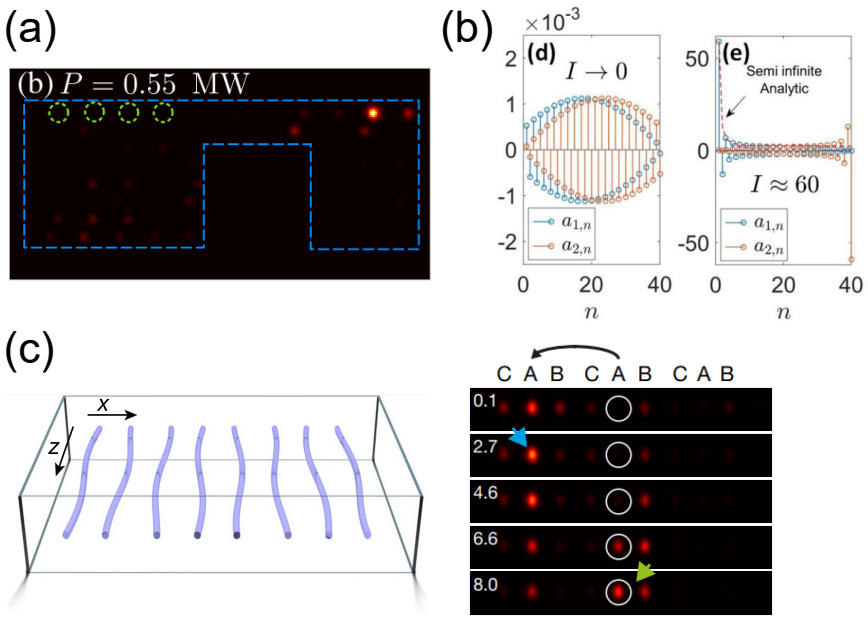

Figure 3.4: Nonlinear topological phenomena. (a) Topological edge soliton in photonic systems. This figure is adapted from D. Leykam and Y. D. Chong, Edge Solitons in Nonlinear-Photonic Topological Insulators. Phys. Rev. Lett. **117,** 143901 (2016) [44]. Copyright 2016 by the American Physical Society. (b) The nonlinearity-induced topological phase transition in the nonlinear SSH model. The left and right panels show the bulk mode and edge mode that can appear at different intensities. This figure is adapted from Y. Hadad, A. B. Khanikaev, and A. Alù, Self-induced topological transitions and edge states supported by nonlinear staggered potentials. Phys. Rev. B **93,** 155112 (2016) [46]. Copyright 2016 by the American Physical Society. (c) Photonic setup of the quantized nonlinear Thouless pumping. The one-dimensional array of waveguides (left panel) becomes a photonic topological insulator with periodic driving. Then, even under the existence of the Kerr nonlinearity, the quantized transport of the wave packet can be confirmed (right panel). This figure is adapted from M. Jürgensen, S. Mukherjee, and M. C. Rechtsman, Quantized nonlinear Thouless pumping. Nature **596,** 63–67 (2021) [302].

the potential relevance of topological band structures and their associated phenomena (i.e., edge modes) in nonlinear systems.

3.4.1 Topological solitons

The early studies on nonlinear topology investigated the nonlinear effects in photonic Floquet topological insulators [168], where the Kerr nonlinearity ubiquitously appears. Reference [43] investigated a honeycomb-lattice model with on-site Kerr nonlinear terms. They found that starting from the bulk-localized state, the model exhibits self-localized wave packets even in its bulk [300]. Such self-localized wave packets are induced by both the nontrivial bulk topology and the nonlinearity; the nonlinear term and localized intensities of the wave packets create effective holes, because the on-site nonlinearity induces large effective potentials. Then, the effective holes behave as effective boundaries at which the topological boundary modes can emerge.

A previous study on another two-dimensional photonic Floquet topological insulator [44] revealed a different type of topological solitons, i.e., topological edge solitons [298, 301]. The study also investigates the effect of the Kerr nonlinearity in topological photonics and the self-focusing effect of the Kerr nonlinearity (cf. Sec. 3.1.2) leads to the spontaneous formation of soliton-like wave packets propagating along the edge of the system. Furthermore, they discussed the possible application to the power-dependent filter, where wave packets with weak intensities cannot pass, while ones with strong intensities can pass. They also discussed the application to a nonlinear

optical switch, which can eliminate a stationary gap soliton by the collision with a topological edge soliton. The existence of the topological edge solitons has also been confirmed in experiments, in particular in photonic setups [45, 299].

The interplay between topological edge modes and solitons has also been studied in one-dimensional nonlinear systems. Specifically, the mechanical lattice was experimentally investigated [244]. The mechanical lattice imitates the SSH model in the linear perturbation regime, while the strong amplitudes of oscillations can induce nonlinear effects. Then, the propagation of the localized wave packet occurs in such a mechanical SSH system. Recent research has also discussed the topological property of such nonlinear mechanical lattices in terms of the Poincaré-Hopf index [243].

3.4.2 Nonlinear Thouless pump

As discussed in the previous chapter, the Thouless pump in periodically driven one-dimensional systems has a topological origin and is characterized by the nonzero Chern number. Very recently, the nonlinear effect on the Thouless pump has also been investigated [302–308]. In particular, the previous studies have revealed that the discretized transport in the Thouless pump remains in weakly nonlinear regimes. Such a discretized transport of the wave packet is also confirmed in a photonic metamaterial that imitates the Rice-Mele model and exhibits the Kerr nonlinearity.

Some previous studies [303, 305] also attempted to explain the discretization from the Chern number in the linear limit. They assumed that the wave packet transported by the Thouless pump is described by the superposition of linear eigenvectors as the wave packet in a linear system can be described by the linear combination of eigenvectors with almost the same weight. Then, one can show that the Chern number corresponds to the displacement of the transported wave packet as in linear systems.

However, the proof of the correspondence between the Chern number and the quantized transport of the wave packet is restricted to the weakly nonlinear regime, and thus the strong nonlinearity can alter the situation. In fact, some studies [304, 307, 308] have revealed that strong nonlinearity can fractionalize the transport of the wave packet or even prevent the Thouless pump. While the fractionalization may be related to the fractional quantum Hall effect [309, 310], the mechanism of such breakdown of the quantized nonlinear Thouless pump is unelucidated. Since the nonlinear Chern number that we will propose in Sec. 5 can reflect the nonlinear effect, it may provide insights to elucidate this breakdown of the nonlinear Thouless pump.

3.4.3 Nonlinearity-induced topological phase transition

While we have discussed the effect of the nonlinearity added to linear topological insulators, nonlinear effects can drastically change the notion of topology by altering topologically trivial systems into nontrivial ones. Such transitions of topological phases, termed *nonlinearity-induced topological phase transitions*, have also attracted much interest in studies on the nonlinear topology [46–48, 311–314]. An early work [46] analyzed the nonlinear counterpart of the SSH model with nonlinear hopping amplitudes in the intracell hopping. In such a one-dimensional system, the existence of the localized zero mode depends on the nonlinearity tuned by the amplitude of the nonlinear wave.

We here note that tuning the strength of the nonlinearity is equivalent to considering the nonlinear waves with different amplitudes if the nonlinear term has a simple form. For example, let us consider a linearly coupled lattice with the on-site Kerr nonlinearity

$$i\frac{\partial \psi_j}{\partial t} = \sum H_{jk}\psi_k + \kappa|\psi_j|^2\psi_j, \tag{3.38}$$

where ψ_j is the state variable and H_{jk} represents the linear coupling. κ corresponds to the strength of the nonlinearity. Then, if we consider the scale transformation of the state variables $\tilde{\psi}_j = c\psi_j$,

the equation reads

$$i\frac{\partial\tilde{\psi}_j}{\partial t} = \sum H_{jk}\tilde{\psi}_k + \frac{\kappa}{c^2}|\tilde{\psi}_j|^2\tilde{\psi}_j. \tag{3.39}$$

Comparing Eqs. (3.38) and (3.39), one can check that the change of the amplitude is reflected as the change of the strength of the nonlinear term $\kappa \to \kappa/c^2$. Therefore, one can identify the change in the strength of the nonlinearity to the change in the amplitudes. In this sense, the nonlinearity-induced topological phase transition also indicates the amplitude dependence of the nonlinear topological phases.

An important issue on the nonlinearity-induced topological phase transition is whether or not there exists topological invariants that can describe both the conventional topological phase and the nonlinearity-induced phase. Previous studies [47, 48] tackled this problem particularly in one-dimensional systems. They utilized nonlinear eigenvalue problems [315, 316] to define the nonlinear winding numbers that characterize the nonlinear topology in one-dimensional systems. Such nonlinear eigenvalue problems are basically defined by using a nonlinear function $f(\Psi)$ as

$$f(\Psi) = E\Psi, \tag{3.40}$$

where E and Ψ are the nonlinear eigenvalue and eigenvector, respectively (see also Sec. 5). Zhou *et al.* [48] also discussed that some unconventional nonlinear models may need the modification of the nonlinear eigenvalue problems into that deriving periodic solutions. Both the studies used the nonlinear eigenvectors and calculated the perturbation theory of them. Finally, the previous studies [48] derived the nonlinear Berry phases, which have nonlinear correction terms and are reduced to the conventional one in the linear limit. While they also numerically analyzed the bulk-boundary correspondence of the nonlinear Berry phase, it has been unclear whether or not the bulk-boundary correspondence is valid in arbitrary strength of nonlinearity.

The nonlinearity dependence of the behavior of topological edge modes has also been investigated in various setups. For example, the stability of a topological edge mode was investigated in a nonlinear Floquet topological insulator and revealed to show the transition in its lifetime [314]. Furthermore, the effect of strong nonlinearity can break the bulk-boundary correspondence by inducing strongly localized states. Such a strong localization is confirmed from the quench dynamics in both one- and two-dimensional models [301, 313].

3.4.4 Other nonlinear topological phenomena

Some recent studies [49, 317] have discussed the interplays between synchronization and topological edge modes. In particular, a previous study [49] demonstrated the existence of cluster synchronization where the edge oscillators are synchronized with a different frequency from that of the bulk ones. We note that the topological synchronized state that we will study in Chapter 4 is different from the synchronization analyzed in these recent works, since the bulk oscillators are chaotic, and thus qualitatively different behaviors can be seen in the edge and bulk oscillators.

The interplay between the non-Hermitian skin effect and the nonlinearity is also an interesting topic in the studies of nonlinear topology. Recent studies [318, 319] investigated the Hatano-Nelson model with nonlinear on-site terms and revealed that there still exist localized modes. The nonlinearity and non-Hermitian skin effects can also be of practical use to control the single-mode lasing [320].

3.4.5 Remarks on eigenvalue nonlinearity

In mathematics, the terminology, nonlinear eigenvalue problem, is also used to represent the nonlinearity in eigenvalues. In more detail, one can consider a sequence of matrices $\{H_n\}_{n=0,1,\cdots,N_{\max}}$ and a nonlinear eigenequation

$$\sum_n E^n H_n \psi = 0, \tag{3.41}$$

where E is a nonlinear eigenvalue and ψ is a nonlinear eigenvector [*2]. We note that this equation is still linear in the eigenvector ψ, while it is nonlinear in the eigenvalue E in the case of $N_{\max} \geq 2$. If $N_{\max}$ is equal to one, this eigenequation is equivalent to a (linear) generalized eigenequation [92, 321, 322]. If we further assume $H_0 = I$ (an identity matrix), the nonlinear eigenequation is reduced to a normal eigenequation.

Nonlinearity in eigenvalues can be seen in, e.g., photonics systems and mechanical metamaterials [323, 324]. Specifically, if the equation of motion is described by second- or higher-order differential equations, its Fourier transformation leads to the nonlinear terms of the frequency (or the wavenumber). Then, to obtain the normal mode with a fixed frequency, one needs to solve the nonlinear eigenvalue problem.

Recent research discusses topological edge modes under the eigenvalue nonlinearity. Specifically, Reference [325] has shown that one can predict the existence of topological edge modes by the Chern number of effective Hamiltonians that is constructed by fixing $E = E_0$, $H_{\text{eff}}(E_0) = \sum_i (E_0)^i H_i$. The bulk-boundary correspondence under the eigenvalue nonlinearity is also numerically confirmed in a nonlinear extension of the Haldane model [326]. While such nonlinear topology also remains an intriguing problem, we focus on *eigenvector* nonlinearity, which is motivated by its vast application to both classical and quantum systems.

[*2]Nonlinear eigenvalue problem is not restricted to those described as the sum of a series. In general, the nonlinear eigenvalue equation with eigenvalue nonlinearity is defined by using a matrix $H(E)$ parametrized by the nonlinear eigenvalue E as $H(E)\psi = 0$, where ψ represents the nonlinear eigenvector.

Chapter 4

Topological synchronization of nonlinear oscillators

While previous studies have revealed the existence of topological edge modes in nonlinear systems, the roles of topology in dissipative nonlinear systems have been largely unexplored compared to those in conservative systems. In particular, despite the abundance of studies on nonlinear phenomena such as synchronization and chaos, the interplays between those nonlinear phenomena and band topology have been unelucidated.

In this chapter, we reveal the role of topology in the synchronization of nonlinear oscillators by demonstrating the existence of the topological synchronized state, where the edge oscillators are synchronized while the bulk ones are chaotic. Such a topological synchronized state is realized by introducing topological linear couplings to nonlinear oscillators. To show the ubiquity of the topological synchronization, we propose and analyze several models, which utilize the linear couplings described by the Hamiltonian of exceptional edge modes (cf. Sec. 2.3.5 and Appendix A), non-Hermitian Chern insulators, and Hermitian topological insulators.

In Sec. 4.1, we will describe the definition of the topological synchronized state and the general setup of the topological synchronization. We also summarize the results of the three models analyzed in our study. In the following three sections, we will analyze three different models for each: the model using exceptional edge modes in Sec. 4.2, one using a non-Hermitian Chern insulator in Sec. 4.3, and one using Hermitian linear couplings and inhomogeneous oscillators in Sec. 4.4. In Sec. 4.5, we will propose applications of the topological synchronized state. Finally, we summarize the results and discuss the future perspectives in Sec. 4.6.

4.1 Concept of topological synchronization and summary of models

4.1.1 General setup and basic strategy to realize topological synchronized state

We here define the topological synchronized state as a coexistence of synchronized edge oscillators and desynchronized bulk ones with a topological origin. Such a topological synchronized state can be seen in periodically aligned nonlinear oscillators on a lattice, where each oscillator is linearly coupled to others on its neighbor sites. We note that some previous studies have also discussed the role of topology in periodically aligned oscillators and found cluster synchronization where the frequencies are different between edge and bulk oscillators (see Sec. 3.4.4 for the details of the previous study and Appendix B.3 for other models that we find). However, such cluster synchronization is out of the definition of the topological synchronized state, because they do not have desynchronized bulk. Compared to such cluster synchronization, the topological synchronized state considered here involves more nontrivial nonlinear effects, such as chaos in the bulk (Sec. 4.2.2) and nonlinearity-induced boundaries (Sec. 4.2.3).

Basically, one can realize the topological synchronized state by introducing linear couplings

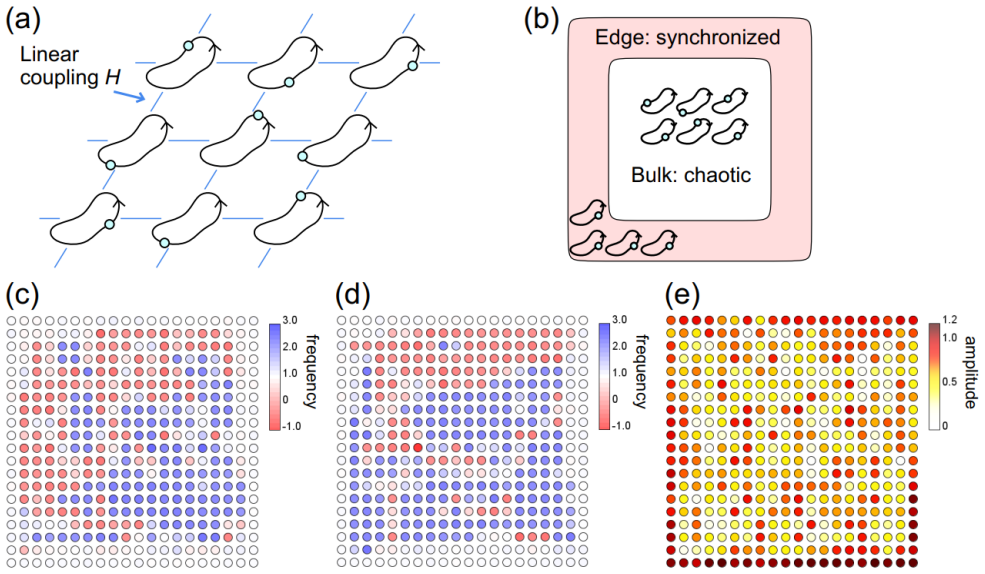

Figure 4.1: Conceptual figures of the topological synchronization and its dynamics. (a) Schematic of the models of topological synchronization. Nonlinear oscillators are linearly coupled to their neighbors. The linear coupling is described by the Hamiltonian of topological insulators. (b) Schematic of the topological synchronized state. In the topological synchronized state, the edge oscillators are synchronized while the bulk ones are chaotic. (c, d) Frequency distributions of the oscillators in our first model (4.3). We show the snapshot at the times $t = 100$ and $t = 200$ in panel (c) and (d), respectively. We confirm almost the same frequency of the edge oscillators, which indicates the synchronization of the edge oscillators. Meanwhile, the bulk ones exhibit time- and space-varying frequencies and thus are desynchronized. We use the parameters $u = -1$, $b = 0.5$, $\alpha = 0.5$, $\beta = 1$, $\omega_0 = 1$, and $\Delta\omega = 0.2$. (e) Amplitude distribution of the oscillators in our first model (4.3). This is the snapshot at $t = 100$, and we use the same parameters in panels (c) and (d). The edge oscillators exhibit larger amplitudes than the bulk ones. These figures are adapted from K. Sone, Y. Ashida, and T. Sagawa, Topological synchronization of coupled nonlinear oscillators. Phys. Rev. Research **4,** 023211 (2022) [327] licensed under a Creative Commons Attribution 4.0 International License (http://creativecommons.org/licenses/by/4.0/).

between the periodically aligned oscillators that are described by a Hamiltonian of a topological insulator. Specifically, one should utilize the topological linear coupling exhibiting lasing edge modes, where only the edge modes have positive imaginary parts of eigenvalues and thus are amplified. By using such lasing edge modes, synchronized edge oscillations are self-excited and thus realized from a wide range of initial conditions.

In our work, we consider linearly coupled Stuart-Landau oscillators [233] (see Sec. 3.1.1 for the detailed properties of Stuart-Landau oscillators) to demonstrate the existence of the topological synchronized state. We arrange M Stuart-Landau oscillators at each lattice point of a square lattice and linearly couple them to those at the same and neighbor sites. The general dynamics of such coupled Stuart-Landau oscillators is described as

$$\frac{d}{dt}\Psi_j(\mathbf{x}) = (i\omega_j(\mathbf{x}) + \alpha_j(\mathbf{x}) - \beta_j(\mathbf{x})|\Psi_j(\mathbf{x})|^2)\Psi_j(\mathbf{x}) - i\sum_{k,\mathbf{x}'} H_{jk}(\mathbf{x},\mathbf{x}')\Psi_k(\mathbf{x}'), \tag{4.1}$$

where $\mathbf{x} = (x, y)$ and $\mathbf{x}' = (x', y')$ are the location of the site and $j, k = 1, \cdots, M$ represent the index of oscillators at each site. $\Psi_j(\mathbf{x})$ is the state variable of the jth oscillator at site $\mathbf{x}$, and $\omega_j(\mathbf{x})$ is its natural frequency. To investigate the robustness of the topological synchronized state against disorders, we assume that the natural frequencies $\omega_j(\mathbf{x})$ are inhomogeneous depending on the oscillators. We also focus on the case that $\alpha_j(\mathbf{x})$ and $\beta_j(\mathbf{x})$ are real, which determines the amplitude of the self-oscillations of each oscillator. In most of the calculations below, we

Table 4.1: Summary of the properties of the models of the topological synchronized state. The checkmarks represent the existence of the topological synchronized state and the extra boundary modes at nonlinearity-induced boundaries.

Model	Topological synchronization	Protection mechanism	Coupling	Extra boundary modes
Model 1 (Eqs. (4.2), (4.3))	✓	Exceptional edge modes	Non-Hermitian	✓
Model 2 (Eq. (4.10))	✓	Conventional bulk topology	Non-Hermitian	×
Model 3 (Eqs. (4.11), (4.12))	✓ (Dependent on components)	Exceptional edge modes	Hermitian	×

consider constant $\alpha_j(\mathbf{x})$ and $\beta_j(\mathbf{x})$, while we use index-dependent α_j in Sec. 4.4 to realize the topological synchronized state with Hermitian linear couplings. Finally, $H_{jk}(\mathbf{x}, \mathbf{x}')$ determines the linear coupling introduced into the Stuart-Landau oscillators. By adopting a Hamiltonian of topological lasing edge modes as $H_{jk}(\mathbf{x}, \mathbf{x}')$, we can realize the topological synchronized state in the coupled Stuart-Landau oscillators in Eq. (4.1).

4.1.2 Summary of properties of models

In Table 4.1, we summarize the properties of the models that we analyze below. We consider three models whose linear couplings are described by different Hamiltonians of topological insulators. In the first model, we use the Hamiltonian of exceptional edge modes (Sec. 2.3.5 and Appendix A). In the second model, we consider the linear coupling whose edge modes are protected by the conventional bulk topology. Finally, we consider the model with Hermitian linear couplings and inhomogeneity of oscillators. All the models exhibit the topological synchronized state, while the last model exhibits component dependence of the synchronization of the edge oscillators. We also discussed the existence of the extra boundary modes localized at the nonlinearity-induced boundaries in the first model, while the other models do not exhibit them.

4.2 Model utilizing non-Hermitian exceptional edge modes

4.2.1 Model and its dynamics

In the first model of topological synchronization, we adopt a Hamiltonian of non-Hermitian exceptional edge modes (see Sec. 2.3.5 and Appendix A) as a linear matrix describing the linear coupling ($H_{jk}(\mathbf{x}, \mathbf{x}')$ in Eq. (4.1)). By utilizing the Hamiltonian of exceptional edge modes, we can realize the topological synchronized state in a relatively simple setup compared to other models. Furthermore, in this model, we can observe unconventional nonlinear effects, namely, extra boundary modes localized at nonlinearity-induced boundaries as discussed in Sec. 4.2.3.

In more detail, we construct the Hamiltonian of exceptional edge modes from a Hamiltonian of a Chern insulator model called the Qi-Wu-Zhang (QWZ) model [94], $H_{\mathrm{QWZ}}(\mathbf{k}) = (u + \cos k_x + \cos k_y)\sigma_z + \sin k_x \sigma_x + \sin k_y \sigma_y$ (see also Sec. 2.2.3), with σ_i $(i = x, y, z)$ being the ith component of the Pauli matrices. We prepare a layer of the QWZ model and another layer of its time-reversal counterpart H^*_{QWZ} and combine them by the non-Hermitian coupling. Finally, we obtain the Hamiltonian of exceptional edge modes used in our first model, which is described in the wavenumber space as

$$H(\mathbf{k}) = (u + \cos k_x + \cos k_y) I_2 \otimes \sigma_z + \sin k_y I_2 \otimes \sigma_y + \sin k_x \sigma_z \otimes \sigma_x + ib\sigma_x \otimes \sigma_x, \tag{4.2}$$

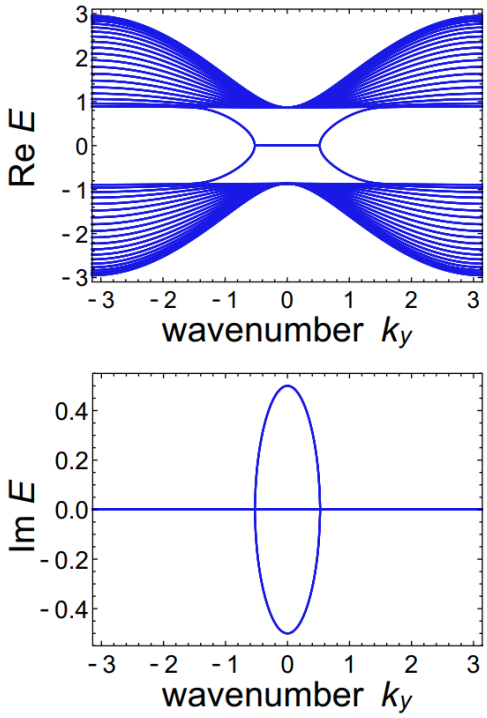

Figure 4.2: Complex dispersion relation of the Hamiltonian used in our first model (4.2). One can check the existence of the gapless edge modes with positive imaginary parts of eigenvalues. Therefore, the edge modes are amplified. We also confirm the existence of exceptional points in the gapless band, which protect the gapless edge modes from gap opening. We use the parameters $u = -1$ and $b = 0.5$. These figures are adapted from K. Sone, Y. Ashida, and T. Sagawa, Topological synchronization of coupled nonlinear oscillators. Phys. Rev. Research **4,** 023211 (2022) [327] licensed under a Creative Commons Attribution 4.0 International License (http://creativecommons.org/licenses/by/4.0/).

with I_2 being a 2×2 identity matrix. Figure 4.2 shows the complex band structure of this model, where we can confirm the existence of gapless edge modes with exceptional points in their band. Via the Fourier transformation, we can also obtain the following real-space description of the Hamiltonian:

$$\begin{aligned} H_{jk}(\mathbf{x},\mathbf{x}') &= \left(u\delta_{\mathbf{x},\mathbf{x}'} + \frac{\delta_{\mathbf{x}+\mathbf{e}_x,\mathbf{x}'} + \delta_{\mathbf{x}-\mathbf{e}_x,\mathbf{x}'} + \delta_{\mathbf{x}+\mathbf{e}_y,\mathbf{x}'} + \delta_{\mathbf{x}-\mathbf{e}_y,\mathbf{x}'}}{2}\right)(I_2 \otimes \sigma_z)_{jk} \\ &\quad + i\frac{\delta_{\mathbf{x}+\mathbf{e}_y,\mathbf{x}'} - \delta_{\mathbf{x}-\mathbf{e}_y,\mathbf{x}'}}{2}(I_2 \otimes \sigma_y)_{jk} \\ &\quad + i\frac{\delta_{\mathbf{x}+\mathbf{e}_x,\mathbf{x}'} - \delta_{\mathbf{x}-\mathbf{e}_x,\mathbf{x}'}}{2}(\sigma_z \otimes \sigma_x)_{jk} + ib\delta_{\mathbf{x},\mathbf{x}'}(\sigma_x \otimes \sigma_x)_{jk}, \end{aligned} \tag{4.3}$$

where $\delta_{\mathbf{x},\mathbf{x}'}$ represents the Kronecker delta satisfying $\delta_{\mathbf{x},\mathbf{x}'} = 1$ for $\mathbf{x} = \mathbf{x}'$ and $\delta_{\mathbf{x},\mathbf{x}'} = 0$ otherwise. $\mathbf{e}_i$ is a unit vector in the $i(= x, y)$ direction. We consider $M = 4$ oscillators at each lattice point.

We first numerically demonstrate the emergence of the topological synchronized state, i.e., the coexistence of synchronized edge oscillators and desynchronized bulk ones by calculating the dynamics of the model using the linear coupling (4.3). Figures 4.1 (c) and (d) show the snapshots of the numerically calculated dynamics. One can confirm that the edge oscillators have almost the same frequency around $\omega = 1$, which indicates the synchronization of the edge oscillators. In contrast, the bulk oscillators have inhomogeneous frequencies. Each bulk oscillator also shows time-varying frequencies. Thus, these results indicate the coexistence of synchronized edge oscillators and desynchronized bulk ones, which is the defining feature of the topological synchronized state.

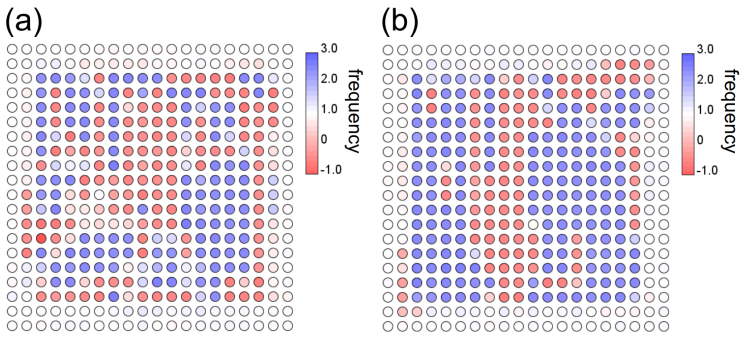

Figure 4.3: Topological synchronization under the absence of fluctuations of natural frequencies. Panels (a) and (b) are the snapshots of the frequency distributions of the first component of oscillators at $t = 100$ and $t = 200$, respectively. We can confirm the emergence of the topological synchronized state. We use the parameters $u = -1$, $b = 0.5$, $\alpha = 0.5$, $\beta = 1$, $\omega_0 = 1$, and $\Delta\omega = 0$. These figures are adapted from K. Sone, Y. Ashida, and T. Sagawa, Topological synchronization of coupled nonlinear oscillators. Phys. Rev. Research **4,** 023211 (2022) [327] licensed under a Creative Commons Attribution 4.0 International License (http://creativecommons.org/licenses/by/4.0/).

While the numerical result in Fig. 4.1 is obtained under the inhomogeneous natural frequencies $\omega_j(\mathbf{x})$, the inhomogeneity of the natural frequencies is unnecessary to realize the desynchronization of bulk oscillators. We confirm the irrelevance of the inhomogeneity of the natural frequencies by calculating the dynamics of the model under homogeneous frequency $\omega_j(\mathbf{x}) = \omega_0$. Figure 4.3 shows the numerical result, and one can still find space- and time-varying frequencies in the bulk, which indicates the desynchronization of the bulk oscillators.

Meanwhile, the synchronization of edge oscillators even under the inhomogeneous natural frequencies implies the robustness of the topological synchronized state against disorders. We further examine such robustness by calculating the dynamics under different strengths of the linear couplings and the inhomogeneity of the natural frequencies. We here quantify the synchronization of the edge oscillators by the proportions of frequency fluctuations of the edge and bulk oscillators and plot them at each strength of the linear couplings and the inhomogeneity of the natural frequencies. Figure 4.4 shows the result. We confirm that the topological synchronized state robustly appears under the sufficiently small inhomogeneity of the natural frequencies compared to the strength of the linear coupling. The transition line seems to correspond to the parameters where the strengths of the linear couplings and the inhomogeneity of the natural frequencies are balanced and thus the linear band gap can be closed. Therefore, if we consider stronger inhomogeneity of the natural frequencies than those parameters, the topology of the coupled oscillators is changed, and they exhibit a fully desynchronized state. These results support that the topological synchronized state is protected by the band topology derived from the linear coupling.

We note that the positive α is necessary to excite the bulk oscillations and realize the chaotic bulk motion. If we consider negative α, we obtain damped bulk oscillators. However, such coexistence of synchronized edge oscillators and damped bulk ones is not regarded as the topological synchronized state defined in our work, because the bulk oscillators do not exhibit desynchronized oscillations (cf. Appendix B.2). We can also numerically confirm that the topological synchronized state requires nontrivial bulk topology (cf. Fig. 4.15 in Sec. 4.5.1).

4.2.2 Lyapunov analysis

We next show the chaos in the bulk oscillators by conducting the Lyapunov analysis. As discussed in Sec. 3.3.2, the Lyapunov exponents and vectors provide information on the stability and instability of nonlinear dynamics. In this section, we show that our model exhibits positive Lyapunov exponents that indicate the chaos of the dynamics. Furthermore, we calculate the localization

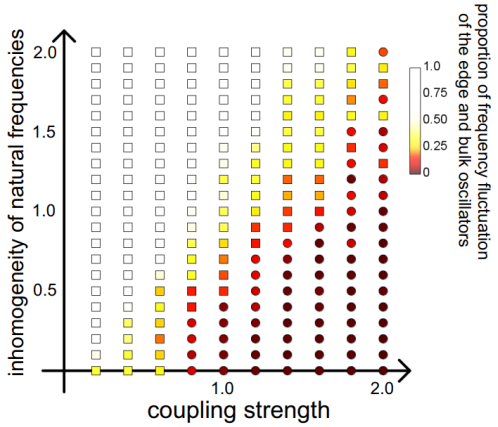

Figure 4.4: Phase diagram of the first model of topological synchronization. The color at each data point represents the ratio of frequency fluctuations of the edge and bulk oscillators. The red region represents the emergence of the topological synchronized state. We also conduct the numerical clustering of the data set and classify the data points into two classes. The circles represent the data points in the obtained cluster corresponding to the topological synchronized state. This figure is adapted from K. Sone, Y. Ashida, and T. Sagawa, Topological synchronization of coupled nonlinear oscillators. Phys. Rev. Research **4,** 023211 (2022) [327] licensed under a Creative Commons Attribution 4.0 International License (http://creativecommons.org/licenses/by/4.0/).

properties of the Lyapunov vectors and check that those corresponding to positive Lyapunov exponents are extended in the bulk, and thus the bulk oscillators exhibit chaotic motions. We note that there are two classifications of chaos in oscillator systems, phase chaos and amplitude chaos [328], and the chaos in our model corresponds to the amplitude chaos that shows phase slips via zero amplitude.

Figure 4.5(a) shows the numerically obtained Lyapunov exponents in our model using linear coupling in Eq. (4.3). About 15 percent of the Lyapunov exponents are positive, which indicates the chaotic dynamics in the model. In contrast, there are sudden decrease around the rescaled index 0.8. This decrease corresponds to the stability of the edge oscillators as is discussed below.

From the Lyapunov exponents, we can also calculate the Lyapunov dimension (see Sec. 3.3.2), which is the effective dimension of a strange attractor in chaotic dynamics. The obtained Lyapunov dimension is $D_L = 254.568$. This corresponds to almost 90 percent of the degrees of freedom of bulk oscillators $D_{\text{bulk}} = 6 \times 6 \times 4 \times 2 = 288$, where we exclude the first and second oscillators from the edge of the system, and assume 6×6 sites as bulk sites that have four oscillators with two degrees of freedom for each. Thus, the obtained Lyapunov exponents and dimension indicate that the bulk oscillators exhibit chaotic dynamics.

To further confirm the chaos in the bulk oscillators, we also calculate the Lyapunov vector. We find that the Lyapunov vectors corresponding to the large Lyapunov exponents are extended to the bulk, while those corresponding to the small exponents are localized at the edge. To quantify such edge-localization of the Lyapunov vectors, we define the index of the proportion of amplitude of the edge oscillators,

$$P_{\text{edge}} = \sum_{i \in \text{edge}} |v_i|^2, \tag{4.4}$$

where v_i is the ith component of the Lyapunov vector and the sum is taken for the components corresponding to the edge oscillators. This index takes the value $0 \leq P_{\text{edge}} \leq 1$ and is close to one if the Lyapunov vector is localized at the edge. We plot the value of the index of each Lyapunov vector in Fig. 4.5. We find the sudden increase in the index (4.4) around the rescaled index 0.8, which indicates the edge-localization of the Lyapunov vectors corresponding to the small Lyapunov vectors. We note that the rescaled index at which the sudden increase of the edge proportion occurs is almost equal to the index where the sudden decrease in the Lyapunov

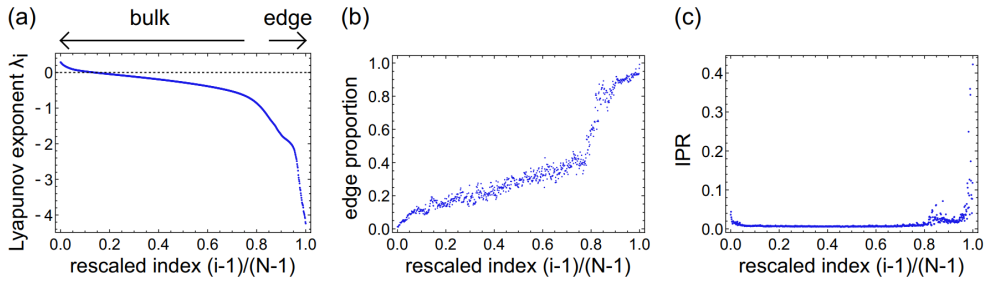

Figure 4.5: Lyapunov analysis on the first model (4.3). (a) Lyapunov exponents of the first model. We arrange the Lyapunov exponents in descending order and rescale their index so that the maximum becomes unity. The Lyapunov exponents above the dashed line are positive and thus indicate the chaos. We use the parameters $u = -1$, $b = 0.5$, $\alpha = 0.5$, $\beta = 1$, $\omega_0 = 0.2$, and $\Delta\omega = 0.2$. (b) Proportions of the edge amplitudes of the Lyapunov vectors in the first model. The steep increase around the relative index 0.8 indicates the edge localization of the Lyapunov vectors with the small Lyapunov exponents. (c) Inverse participation ratios (IPRs) of the Lyapunov vectors in the first model. The steep rise in IPRs of the last several Lyapunov vectors indicates their strong localization. These figures are adapted from K. Sone, Y. Ashida, and T. Sagawa, Topological synchronization of coupled nonlinear oscillators. Phys. Rev. Research **4,** 023211 (2022) [327] licensed under a Creative Commons Attribution 4.0 International License (http://creativecommons.org/licenses/by/4.0/).

exponents is seen in Fig. 4.5(a). Therefore, the topological synchronization is stable against the perturbation to the edge oscillators, which leads to the robust synchronization of the edge oscillators.

We also calculate the inverse participation ratio (IPR),

$$\mathrm{IPR} = \sum_i |v_i|^4, \tag{4.5}$$

to further analyze the localization properties of the Lyapunov vectors. The IPR also satisfies $0 \leq \mathrm{IPR} \leq 1$ and takes a large value when the Lyapunov vector is localized at only a few sites. Figure 4.5(c) shows the IPR of each Lyapunov vector. We confirm that almost all the Lyapunov vectors exhibit small IPR. The exceptions are those corresponding to small Lyapunov exponents, whose rescaled index is larger than 0.98. Therefore, the IPR classifies the edge-localized Lyapunov vectors into two classes, ones extended to the edge and strongly localized ones. The former corresponds to a conventional topological edge mode, while the latter can be regarded as a nonlinearity-induced strongly localized mode.

These behaviors of the Lyapunov exponents and vectors are related to the complex eigenvalues and eigenvectors of the effective Hamiltonian obtained from the linearization of the nonlinear dynamics. This connection is inferred from the fact that in the linear limit ($\beta_j(\mathbf{x}) = 0$ in Eq. (4.1)), the rate of the attenuation and amplification of the perturbation is governed by the imaginary part of the eigenvalue and the direction of the corresponding perturbation matches that of the eigenvector. To confirm the relationship between the Lyapunov analysis and the linear band structure, we derive the effective Hamiltonian via the linearization of the nonlinear dynamics and numerically calculate its band structure. The linearization of the Stuart-Landau oscillators $\dot{\Psi} = (i\omega + \alpha - \beta|\Psi|^2)\Psi$ becomes

$$\frac{d}{dt}\begin{pmatrix} \delta X \\ \delta Y \end{pmatrix} = \begin{pmatrix} i\omega + \alpha - 3\beta X_0^2 - \beta Y_0^2 & -2\beta X_0 Y_0 \\ -2\beta X_0 Y_0 & i\omega + \alpha - \beta X_0^2 - 3\beta Y_0^2 \end{pmatrix}\begin{pmatrix} \delta X \\ \delta Y \end{pmatrix}, \tag{4.6}$$

where we decompose Ψ into the real and imaginary parts, $\Psi = X + iY$, and $X_0 + iY_0$ is the complex state variable around which we conduct the linearization. The eigenvalues of this coefficient

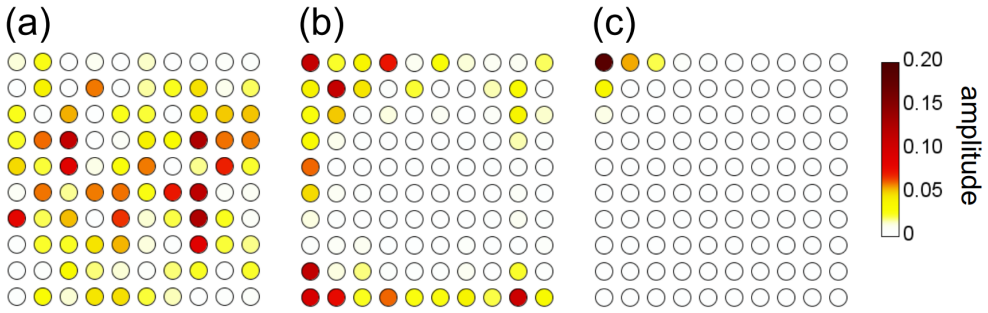

Figure 4.6: Spatial distributions of the Lyapunov vectors in the first model. We use the same parameters as in Fig. 4.5. We plot the Lyapunov vector of the index (a) $n = 50$, (b) $n = 700$, and (c) $n = 800$ for each. We confirm that the Lyapunov vectors are (a) extended in the bulk, (b) localized to the edge, and (c) strongly localized to the corner. These figures are adapted from K. Sone, Y. Ashida, and T. Sagawa, Topological synchronization of coupled nonlinear oscillators. Phys. Rev. Research **4,** 023211 (2022) [327] licensed under a Creative Commons Attribution 4.0 International License (http://creativecommons.org/licenses/by/4.0/).

matrix are $i\omega + \alpha - \beta(X_0^2 + Y_0^2)$ and $i\omega + \alpha - 3\beta(X_0^2 + Y_0^2)$. If we consider the amplitude where the linear gain α and the nonlinear loss $-\beta(X_0^2 + Y_0^2)$ are balanced, the real parts of the eigenvalues are nonpositive, which indicates that the nonlinear terms induce on-site damping effects in the linearized dynamics of the model of the topological synchronization. By adding the terms described in Eq. (4.6) to the Hamiltonian describing the linear coupling (4.3), we obtain the effective Hamiltonian of the linearized dynamics.

We first calculate the nonlinear dynamics of our model to determine the state around which the linearization is conducted, and then numerically diagonalize the effective Hamiltonian of the linearized dynamics. To calculate the dynamics, we consider a 20×20 square lattice and impose the periodic (open) boundary condition in the x (y) direction. We start from a random initial condition and use the state variables of the oscillators in the tenth row at the time $t = 200$ as the state around which we linearize the model. The dispersion relation is calculated in a ribbon geometry with 1×20 supercells. Figure 4.7 shows the obtained dispersion relation. We confirm the existence of gapless modes corresponding to topological edge modes. We also find that the gapless edge modes exhibit negative imaginary parts of eigenvalues. Therefore, the perturbations corresponding to these edge modes are attenuated. While the linearized dynamics only tells us the short-time stability and instability of the nonlinear dynamics, such short-time stability should also affect the long-time stability described by the Lyapunov exponents and vectors. Thus, corresponding to the edge modes in the linearized dynamics, the edge-localized Lyapunov vectors appear and exhibit the small Lyapunov exponents. We note that the non-Hermiticity is important to realize nonzero imaginary parts of eigenvalues of the effective Hamiltonian, which also corresponds to Lyapunov exponents. We also would like to mention the existence of eigenvectors that have the positive imaginary parts of eigenvalues. Such positive imaginary parts appear due to the repulsion of the bulk bands that are flat in the imaginary parts (cf. Fig. 4.2) induced by the nonlinear term. To realize the desired properties of linear bands, the flatness in the imaginary part and the existence of the lasing edge modes, we seem to need at least four oscillators at each lattice point.

4.2.3 Extra boundary modes localized at nonlinearity-induced boundaries

While the nonlinearity induces the chaos of the bulk oscillators in the topological synchronized state, the nonlinear effect further induces unconventional topological edge modes, namely extra edge modes localized at nonlinearity-induced boundaries. The mechanism of emerging such nonlinearity-induced boundaries is as follows; the nonlinear oscillators self-excite their oscillations and show larger amplitudes at the edge than in the bulk due to the topological synchronization (we can confirm such difference in the amplitudes in Fig. 4.1(e)). Then, the difference in amplitudes

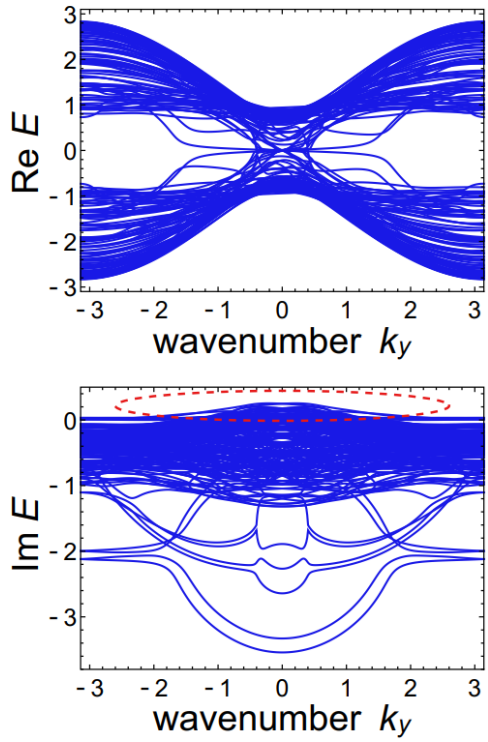

Figure 4.7: Dispersion relation of the effective Hamiltonian obtained from the linear stability analysis of the first model. While the bulk bands are gapless, we still have localized edge modes. We also confirm that the imaginary parts of the eigenvalues of the edge modes are negative, which leads to the small Lyapunov exponents of the localized Lyapunov vectors. We use the parameters $u = -1$, $b = 0.5$, $\alpha = 0.5$, $\beta = 1$, $\omega_0 = 1$, and $\Delta\omega = 0$. These figures are adapted from K. Sone, Y. Ashida, and T. Sagawa, Topological synchronization of coupled nonlinear oscillators. Phys. Rev. Research **4,** 023211 (2022) [327] licensed under a Creative Commons Attribution 4.0 International License (http://creativecommons.org/licenses/by/4.0/).

leads to stronger on-site loss terms in the effective Hamiltonian. Finally, such stronger on-site loss terms separate the oscillators into two regions that are weakly and strongly affected by the nonlinear on-site loss term, which generates the nonlinearity-induced boundaries between the regions. Similar self-induced boundaries are discussed in some previous studies [43] on conservative nonlinear topological insulators.

To explicitly demonstrate the emergence of such stronger on-site loss terms, we rewrite the nonlinear dynamics (4.1) as

$$\frac{d}{dt}\Psi_j(\mathbf{x}) = -i\sum_k \tilde{H}_{jk}(\mathbf{\Psi};\mathbf{x},\mathbf{x}')\Psi_k(\mathbf{x}'), \tag{4.7}$$

$$\tilde{H}_{jk}(\mathbf{\Psi};\mathbf{x},\mathbf{x}') = H_{jk}(\mathbf{x},\mathbf{x}') + (-\omega_j(\mathbf{x}) + i\alpha - i\beta|\Psi_j(\mathbf{x})|^2)\delta_{jk}\delta_{\mathbf{x},\mathbf{x}'}, \tag{4.8}$$

where $\tilde{H}(\mathbf{\Psi};\mathbf{x},\mathbf{x}')$ is the effective Hamiltonian that depends on the state variables and describes the time evolution at each time. The second term in this state-dependent Hamiltonian $(-\omega_j(\mathbf{x}) + i\alpha - i\beta|\Psi_j(\mathbf{x})|^2)\delta_{jk}\delta_{\mathbf{x},\mathbf{x}'}$ is the nonlinear on-site loss term and leads to the nonlinearity-induced boundaries. Since the linear coupling $H_{jk}(\mathbf{x},\mathbf{x}')$ exhibits lasing edge modes, it amplifies the edge oscillators compared to the bulk oscillators (Fig. 4.1(e)). Then, the on-site loss term $(-\omega_j(\mathbf{x})+i\alpha-i\beta|\Psi_j(\mathbf{x})|^2)\delta_{jk}\delta_{\mathbf{x},\mathbf{x}'}$ has large negative values, which more strongly attenuates the edge oscillators than the bulk ones. A previous study [329] has shown that the on-site loss terms create effective boundaries in linear systems. In a similar sense, the nonlinear oscillators also create effective boundaries between the edge and bulk oscillators and can exhibit an extra number of boundary modes localized at such effective boundaries.

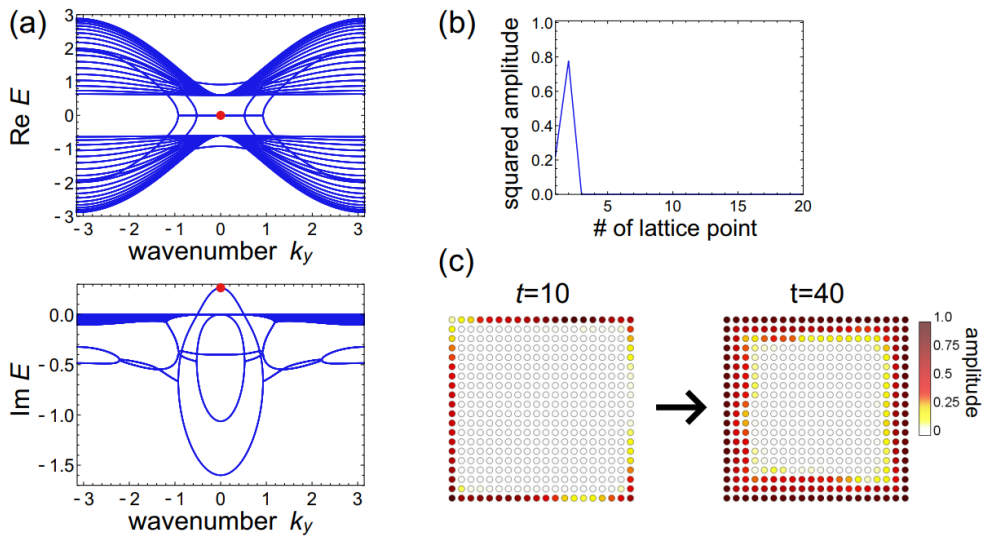

Figure 4.8: Emergence of the extra boundary modes localized at the nonlinearity-induced boundaries. (a) Dispersion relation of the state-dependent Hamiltonian (4.8). We find the double number of gapless bands (eight, doubly degenerated) compared to the original Hamiltonian (4.2). We use the parameters $u = -1$, $b = 0.8$, $\alpha = 0$, $\beta = 1$, $\omega_0 = 0$, and $\Delta\omega = 0$. (b) Spatial distribution of the extra boundary mode in the state-dependent Hamiltonian. The corresponding eigenvalue is denoted by the red circle in panel (a). (c) Dynamical demonstration of the extra boundary modes. These are the snapshots of the relative-amplitude distribution at $t = 10$ and $t = 40$. When the amplitudes are small (right figure), only the outermost oscillators exhibit large amplitudes. In contrast, after the amplitudes become larger and nonlinearity becomes comparable to the linear coupling, the second and third sites from the edge also oscillate largely, which implies the emergence of the extra boundary modes. These figures are adapted from K. Sone, Y. Ashida, and T. Sagawa, Topological synchronization of coupled nonlinear oscillators. Phys. Rev. Research **4,** 023211 (2022) [327] licensed under a Creative Commons Attribution 4.0 International License (http://creativecommons.org/licenses/by/4.0/).

To confirm the existence of such extra boundary modes, we calculate the band structure of the state-dependent Hamiltonian (4.8). We first calculate the spatial distribution of the edge modes of the linear coupling H. We here consider the 1×20 supercell structure and the periodic boundary condition in the y direction. Then, we substitute it into Eq. (4.8). Finally, we numerically diagonalize the state-dependent Hamiltonian. Figure 4.8(a) shows the obtained dispersion relation. We confirm that there are eight (doubly degenerated) gapless bands, which is double the number of the gapless modes in the Hamiltonian used to describe the linear coupling. Therefore, the state-dependent Hamiltonian exhibits extra boundary modes that cannot be seen in the original Hamiltonian. We note that such extra boundary modes have positive imaginary parts of eigenvalues and the largest amplitudes at the second site (Fig. 4.8(b)), which leads to the amplification of the second oscillators from the edge of the system.

We also numerically demonstrate the emergence of extra boundary modes by calculating the dynamics. Specifically, we start from the random initial condition with small amplitudes, where the nonlinear effects are negligible. The oscillators are self-excited and increase their amplitudes in the time evolution. At the first stage of the simulation, we obtain large amplitudes only at the outermost oscillators. However, after the increased amplitudes of the oscillators reach a critical amplitude, the nonlinear loss and the linear couplings are balanced and create effective boundaries. Then, we observe the amplification of the second and third sites from the edge, which is regarded as the emergence of the extra boundary modes localized at the nonlinearity-induced boundaries. Figure 4.8(c) shows the snapshots of the numerical simulation and the dynamical emergence of such extra boundary modes.

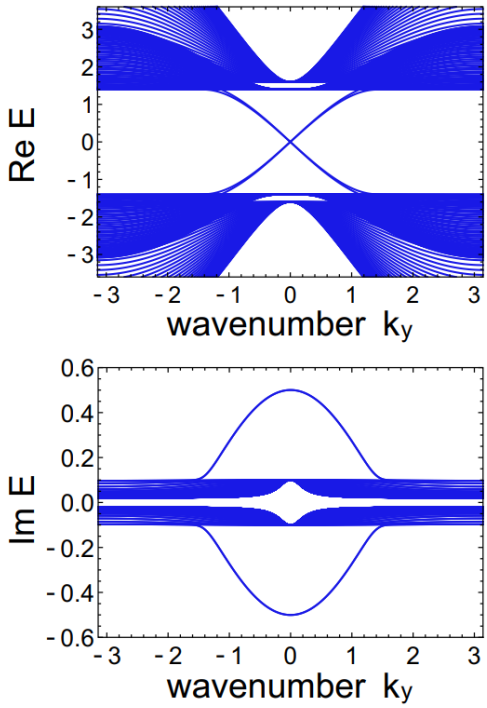

Figure 4.9: Complex band structure of the Hamiltonian used in the second model (4.10). We confirm the existence of gapless edge modes, which are protected by conventional band topology unlike the Hamiltonian used in the first model. We use the parameters $u = -1$, $u' = 0.02$, $a = 2$, and $b = 0.5$. These figures are adapted from K. Sone, Y. Ashida, and T. Sagawa, Topological synchronization of coupled nonlinear oscillators. Phys. Rev. Research **4,** 023211 (2022) [327] licensed under a Creative Commons Attribution 4.0 International License (http://creativecommons.org/licenses/by/4.0/).

We note that the emergence of the extra boundary modes at the nonlinearity-induced boundaries can also be seen in the effective Hamiltonian derived from the linearization of the dynamics (Fig. 4.7). Thus, such extra boundary modes also affect the number of the synchronized edge oscillators in the topological synchronized state; both the first and second oscillators from the edge are synchronized, which is inferred from the Lyapunov dimensions.

4.3 Model utilizing a Hamiltonian of a non-Hermitian Chern insulator

4.3.1 Model and its dynamics

In the previous section, we introduce the linear couplings described by the Hamiltonian of exceptional edge modes to the Landau-Stuart oscillators. While such a Hamiltonian has a relatively simple structure useful for implementing it to realistic nonlinear oscillators, the edge modes are not characterized by conventional topological invariants such as the Chern number. Therefore, the previous model is not suitable to clarify the relationship between the bulk topology and the topological synchronized state.

Here, we instead construct a non-Hermitian Hamiltonian of lasing edge modes with nonzero Chern numbers and utilize it to construct another model of the topological synchronized state. Specifically, we consider a non-Hermitian Hamiltonian whose wavenumber-space description is

$$H = \begin{pmatrix} aH_{\mathrm{QWZ}} + iu'I_2 & ibI_2 \\ ibI_2 & H_{\mathrm{QWZ}} - iu'I_2 \end{pmatrix}, \tag{4.9}$$

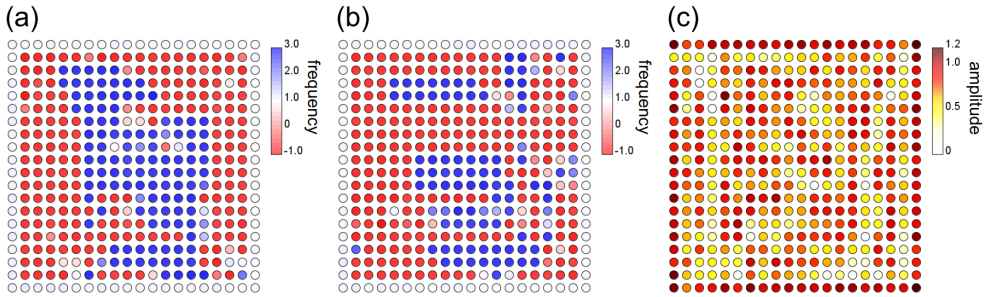

Figure 4.10: Dynamics of the topological synchronization in the second model (4.10). (a,b) Frequency distributions in the second model. We show the snapshots at the times $t = 1000$ and $t = 2000$ in panels (a) and (b), respectively. We confirm the synchronization of the edge oscillators and the desynchronization of the bulk oscillators, which indicates the topological synchronized state. We use the parameters $u = -1$, $u' = 0.02$, $a = 2$, $b = 0.5$, $\alpha = 0.5$, $\beta = 1$, $\omega_0 = 1$, and $\Delta\omega = 0.2$. (c) Amplitude distribution in the second model at $t = 1000$. We confirm the amplification of the edge oscillators. These figures are adapted from K. Sone, Y. Ashida, and T. Sagawa, Topological synchronization of coupled nonlinear oscillators. Phys. Rev. Research **4,** 023211 (2022) [327] licensed under a Creative Commons Attribution 4.0 International License (http://creativecommons.org/licenses/by/4.0/).

where H_{QWZ} is the Hamiltonian of the QWZ model [94] and I_2 is the 2×2 identity matrix. All the parameters in this Hamiltonian, a, b, and u' are real. This Hamiltonian is described in the real space as

$$\begin{aligned} H_{jk}(\mathbf{x},\mathbf{x}') \;=\; & \left(u\delta_{\mathbf{x},\mathbf{x}'} + \frac{\delta_{\mathbf{x}+\mathbf{e}_x,\mathbf{x}'} + \delta_{\mathbf{x}-\mathbf{e}_x,\mathbf{x}'} + \delta_{\mathbf{x}+\mathbf{e}_y,\mathbf{x}'} + \delta_{\mathbf{x}-\mathbf{e}_y,\mathbf{x}'}}{2}\right) \\ & \times \left[\frac{a+1}{2}(I_2 \otimes \sigma_z)_{jk} + \frac{a-1}{2}(\sigma_z \otimes \sigma_z)_{jk}\right] \\ & + i\frac{\delta_{\mathbf{x}+\mathbf{e}_y,\mathbf{x}'} - \delta_{\mathbf{x}-\mathbf{e}_y,\mathbf{x}'}}{2}\left[\frac{a+1}{2}(I_2 \otimes \sigma_y)_{jk} + \frac{a-1}{2}(\sigma_z \otimes \sigma_y)_{jk}\right] \\ & + i\frac{\delta_{\mathbf{x}+\mathbf{e}_x,\mathbf{x}'} - \delta_{\mathbf{x}-\mathbf{e}_x,\mathbf{x}'}}{2}\left[\frac{a+1}{2}(I_2 \otimes \sigma_x)_{jk} + \frac{a-1}{2}(\sigma_z \otimes \sigma_x)_{jk}\right] \\ & + ib\delta_{\mathbf{x},\mathbf{x}'}(\sigma_x \otimes I_2)_{jk} + iu'\delta_{\mathbf{x},\mathbf{x}'}(\sigma_z \otimes I_2)_{jk}, \end{aligned} \tag{4.10}$$

with σ_i being the i component of the Pauli matrices. As the Hamiltonian of the exceptional edge modes in our first model, this Hamiltonian also has two layers of the QWZ model coupled by non-Hermitian terms. Figure 4.9 shows the band structure of this Hamiltonian under the periodic (open) boundary condition in the y (x) direction. We can confirm the emergence of the gapless modes with larger imaginary parts of eigenvalues than those of the bulk modes. Therefore, this Hamiltonian also exhibits lasing edge modes.

We utilize this Hamiltonian as the coefficient matrix in Eq. (4.1) and numerically calculate the dynamics of the nonlinear oscillators. Figure 4.10 shows the snapshots of the numerical simulation. We check that the edge oscillators exhibit almost the same frequencies and thus are synchronized, while the bulk ones exhibit time- and space-varying frequencies, which implies their chaos. Therefore, the model shows the topological synchronized state.

4.3.2 Lyapunov analysis

We also conduct the Lyapunov analysis to confirm the chaos in the bulk oscillators as in our first model. Figure 4.11(a) shows the numerically obtained Lyapunov exponents. One can check the existence of positive Lyapunov exponents, which indicates the chaos.

Figure 4.11(b) and (c) present the indicators of localizations of the Lyapunov exponents, the proportions of edge amplitudes and IPRs. As in our first model, Figure 4.11(b) shows that the

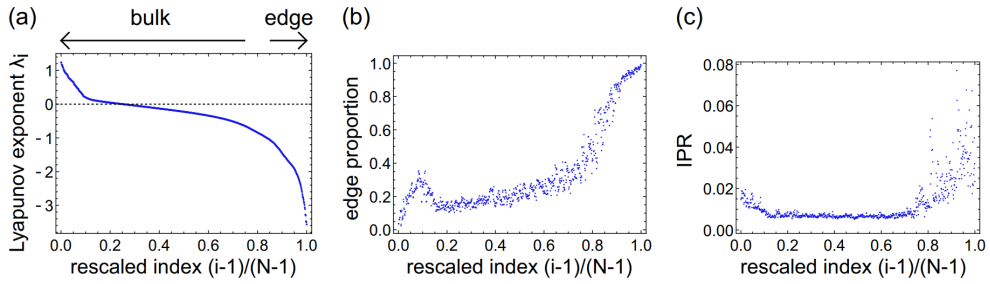

Figure 4.11: Lyapunov analysis on the second model (4.10). (a) Lyapunov exponents of the second model. We arrange the Lyapunov exponents in descending order and rescale their index so that the maximum becomes unity. The Lyapunov exponents above the dashed line are positive and thus indicate the chaos. We use the parameters $u = -1$, $b = 0.5$, $\alpha = 0.5$, $\beta = 1$, $\omega_0 = 0.2$, and $\Delta\omega = 0.2$. (b) Proportions of the edge amplitudes of the Lyapunov vectors in the second model. The steep increase around the relative index 0.8 indicates the edge localization of the Lyapunov vectors with the small Lyapunov exponents. (c) IPRs of the Lyapunov vectors in the first model. IPRs are small compared to those in the first model (Fig. 4.5), and thus there are no strongly localized Lyapunov vectors. These figures are adapted from K. Sone, Y. Ashida, and T. Sagawa, Topological synchronization of coupled nonlinear oscillators. Phys. Rev. Research **4,** 023211 (2022) [327] licensed under a Creative Commons Attribution 4.0 International License (http://creativecommons.org/licenses/by/4.0/).

Lyapunov vectors corresponding to the large Lyapunov exponents are extended to the bulk, while those corresponding to the small exponents are localized at the edge. Therefore, the Lyapunov exponents and vectors indicate the chaos in the bulk oscillators and the stable synchronization in the edge ones. Meanwhile, the behavior of IPRs is different from that in the first model; we do not obtain large IPRs even for the Lyapunov vectors corresponding to the small Lyapunov exponents. The reason of this difference can be the weakness of nonlinearity in the second model, which prevents the self-localization of nonlinear edge modes. We also find that the second model exhibits no extra boundary modes at the nonlinearity-induced boundaries due to the weakness of nonlinearity.

4.4 Model utilizing Hermitian linear couplings

4.4.1 Model and its dynamics

In the models analyzed above, we have utilized non-Hermitian Hamiltonians to describe the linear couplings. While such non-Hermiticity is important to realize desired properties of linear couplings, i.e., exhibiting lasing edge modes, non-Hermiticity may be a barrier to experimental realizations in realistic nonlinear oscillators.

Here, we find that the non-Hermiticity can be included in the inhomogeneity of the nonlinear oscillators, and the topological synchronized state is realized in inhomogeneous oscillators with Hermitian linear couplings. Specifically, we consider a Hamiltonian described in the wavenumber space as

$$\begin{aligned} H(\mathbf{k}) &= (u + \cos k_x + \cos k_y)\sigma_x \otimes \sigma_z + \sin k_y I_2 \otimes \sigma_y \\ &\quad + \sin k_x I_2 \otimes \sigma_x + ib\sigma_z \otimes \sigma_z, \end{aligned} \tag{4.11}$$

which is obtained by the unitary transformation of the Hamiltonian (4.2). The real-space description of this Hamiltonian is

$$H_{jk}(\mathbf{x}, \mathbf{x}') = \left(u\delta_{\mathbf{x},\mathbf{x}'} + \frac{\delta_{\mathbf{x}+\mathbf{e}_x,\mathbf{x}'} + \delta_{\mathbf{x}-\mathbf{e}_x,\mathbf{x}'} + \delta_{\mathbf{x}+\mathbf{e}_y,\mathbf{x}'} + \delta_{\mathbf{x}-\mathbf{e}_y,\mathbf{x}'}}{2} \right) (\sigma_x \otimes \sigma_z)_{jk}$$

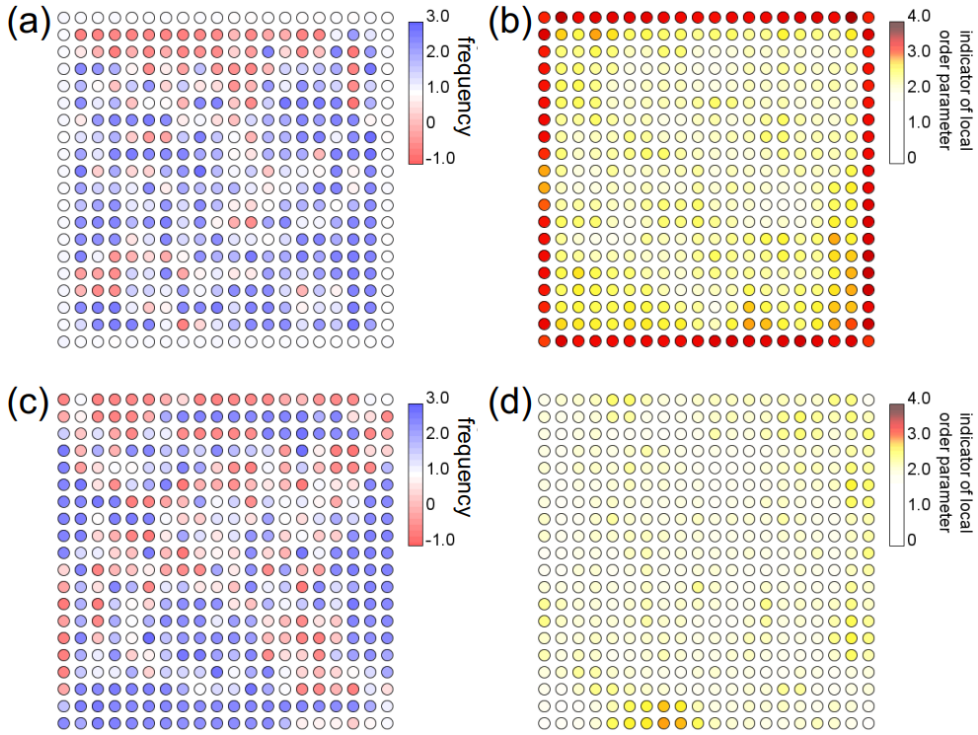

Figure 4.12: Dynamics of the topological synchronization in the third model (4.12). (a,c) Frequency distributions in the third model. We show the snapshots at the times $t = 100$. Panels (a) and (c) show the frequencies of the first and second components for each. We confirm that the edge oscillators at the first components are synchronized, while the second components are desynchronized. (b,d) Indicator of local order parameter in the third model. Panels (a) and (resp. (c)) show the values of the indicator of local order parameter (4.13) of the first and fourth (resp. second and third) components for each. Red color sites show the synchronization of the corresponding oscillators, and we can confirm the edge synchronization only in the first and fourth components of oscillators. We use the parameters $u = -1$, $b = 0.5$, $\alpha = 1$, $\beta = 1$, $\omega_0 = 1$, and $\Delta\omega = 0.2$. These figures are adapted from K. Sone, Y. Ashida, and T. Sagawa, Topological synchronization of coupled nonlinear oscillators. Phys. Rev. Research **4,** 023211 (2022) [327] licensed under a Creative Commons Attribution 4.0 International License (http://creativecommons.org/licenses/by/4.0/).

$$
\begin{aligned}
&+i\frac{\delta_{\mathbf{x}+\mathbf{e}_y,\mathbf{x}'}-\delta_{\mathbf{x}-\mathbf{e}_y,\mathbf{x}'}}{2}(I_2\otimes\sigma_y)_{jk}\\
&+i\frac{\delta_{\mathbf{x}+\mathbf{e}_x,\mathbf{x}'}-\delta_{\mathbf{x}-\mathbf{e}_x,\mathbf{x}'}}{2}(I_2\otimes\sigma_x)_{jk}+ib\delta_{\mathbf{x},\mathbf{x}'}(\sigma_z\otimes\sigma_z)_{jk},
\end{aligned}
\tag{4.12}
$$

with $\delta_{\mathbf{x},\mathbf{x}'}$ being the Kronecker delta and $\mathbf{e}_{x,y}$ being the unit vectors in the x or y direction. In this Hamiltonian, the non-Hermitian term becomes an on-site one $ib\delta_{\mathbf{x},\mathbf{x}'}(\sigma_z\otimes\sigma_z)_{jk}$. Since such an on-site term is equivalent to the change of $\alpha_i(\mathbf{x})$ in Eq. (4.1), we can assume the nonlinear oscillators with the linear terms described by this Hamiltonian as the inhomogeneous oscillators with Hermitian linear couplings.

We numerically confirm the emergence of the topological synchronized state in this inhomogeneous oscillator system. Figure 4.12 shows the snapshot of the simulation of its dynamics. Unlike the first and second models, the edge oscillators only at the first and fourth components of each edge site are synchronized in this model. The other edge oscillators and bulk ones exhibit time- and space-varying frequencies, which implies their chaotic dynamics. To directly confirm such synchronization and desynchronization of the edge oscillators, we also define the local order

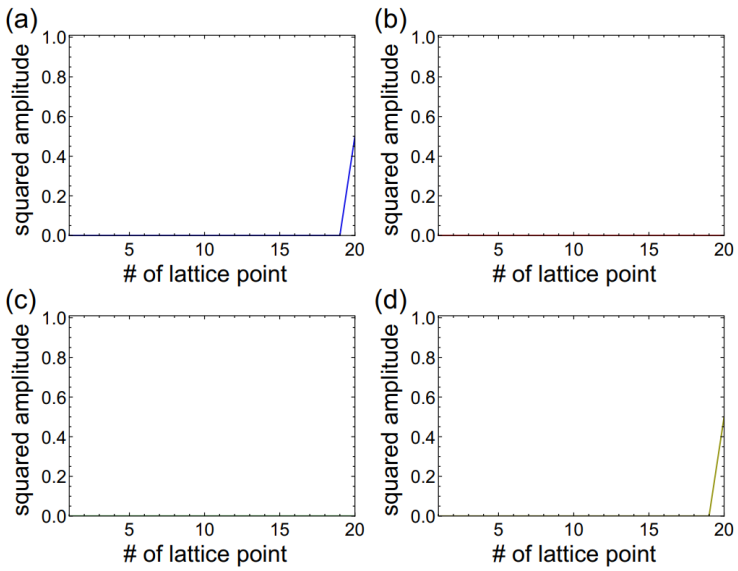

Figure 4.13: Eigenvector of the lasing edge mode of the Hamiltonian used in the third model (4.11). We show the amplitude distributions of lasing edge modes at $k = 0$ with the eigenvalue $E = ib$. Panels (a), (b), (c), and (d) show the first, second, third, and fourth components, respectively. We use the parameters $u = -1$ and $b = 0.5$. These figures are adapted from K. Sone, Y. Ashida, and T. Sagawa, Topological synchronization of coupled nonlinear oscillators. Phys. Rev. Research **4,** 023211 (2022) [327] licensed under a Creative Commons Attribution 4.0 International License (http://creativecommons.org/licenses/by/4.0/).

parameter

$$M(x,y;t) = \frac{1}{2T}\int_{t-T}^{t} dt' \sum_{k=1,4\ (k=2,3)} |\Psi_k(x,y)+\Psi_k(x+1,y)+\Psi_k(x-1,y)+\Psi_k(x,y+1)+\Psi_k(x,y-1)|. \tag{4.13}$$

This local order parameter takes a large value around synchronized oscillators. We plot the local order parameters in Fig. 4.12(b) and (d). The local order parameter clearly indicates that the first and fourth components of the edge oscillators are synchronized, while the second and third components are desynchronized.

The desynchronization of the second and third components of the edge oscillators is related to the eigenvectors of the Hamiltonian (4.11) describing the linear coupling. In fact, the lasing edge modes of the Hamiltonian have nonzero values only at the first and fourth components as shown in Fig. 4.13. Therefore, the edge oscillators only at the first and fourth components are amplified by the lasing edge modes, and their synchronized oscillations are excited.

4.4.2 Lyapunov analysis

We also conduct the Lyapunov analysis in the model utilizing Hermitian linear couplings and confirm the chaos of the bulk oscillators. Figure 4.14(a) shows the numerically obtained Lyapunov exponents. As in the other models, we obtain positive Lyapunov exponents, which indicates the chaotic dynamics.

We also plot the indicators of localization of the Lyapunov vectors and analyze the localization properties of the Lyapunov vectors. Figures 4.14(b,c) show the proportion of edge oscillators of the Lyapunov vectors. One can see that the Lyapunov vectors corresponding to the small Lyapunov exponents exhibit large values of the indicator, which indicates the existence of the edge-localized Lyapunov vectors and their relevance in the stable synchronization of the edge oscillators. We also find the increase of the IPRs at large rescaled indices while the maximum is lower than that in the first model. Therefore, we do not find strong localization in the edge-localized Lyapunov

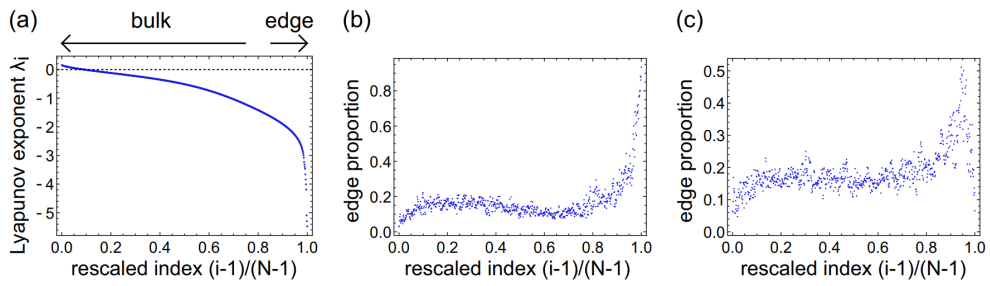

Figure 4.14: Lyapunov analysis on the third model (4.12). (a) Lyapunov exponents of the third model. We arrange the Lyapunov exponents in descending order and rescale their index so that the maximum becomes unity. The Lyapunov exponents above the dashed line are positive and thus indicate the chaos. We use the parameters $u = -1$, $b = 0.5$, $\alpha = 1$, $\beta = 1$, $\omega_0 = 0.2$, and $\Delta\omega = 0.2$. (b,c) Proportions of the edge amplitudes of the Lyapunov vectors in the first model. We plot the proportions of the edge amplitudes in the first and fourth components in panel (b) and those in the second and third components in panel (c). We find a steep increase around the relative index 0.95 in the proportions of the edge amplitudes in the first and fourth components, while there is a decrease in those in the second and third components. Therefore, the edge oscillators in the first and fourth components are synchronized, while those in the second and third components are chaotic. These figures are adapted from K. Sone, Y. Ashida, and T. Sagawa, Topological synchronization of coupled nonlinear oscillators. Phys. Rev. Research **4,** 023211 (2022) [327] licensed under a Creative Commons Attribution 4.0 International License (http://creativecommons.org/licenses/by/4.0/).

vectors compared to the first model. We can also check that extra boundary modes localized at the nonlinearity-induced boundaries disappear in this model. These differences from the first model may be induced by the weakness of the nonlinearity as discussed in the second model.

4.5 Applications

In the topological synchronized state, if the bulk oscillators stop their oscillations, new boundaries are created around them. Then, the synchronized oscillators can appear at such boundaries. We propose that such emergence of synchronized oscillators around the bulk defects can be of applicational use to realize on-demand pattern designing and detect the appearance of defective oscillators. In the last part of this section, we also propose an experimental setup to realize topological synchronization in an electrical circuit.

4.5.1 On-demand pattern designing

We first show that one can arrange synchronized oscillators in an arbitrary pattern by using the topological synchronized state. Such on-demand pattern designing can be realized by placing damped oscillators in the desired pattern. Then, the damped oscillators create effective boundaries around them and the oscillators around such effective boundaries become synchronized.

We numerically demonstrate the possibility of such on-demand pattern designing in the simulation of the oscillator dynamics. We here use the linear coupling in the first model. Figure 4.15 shows the numerically obtained synchronization pattern, where the synchronized oscillators are arranged in the shape of "UT." To explicitly show the synchronization of the oscillators around the effective boundaries, we define the local order parameter of the synchronization,

$$M(x,y;t) = \frac{1}{4T}\int_{t-T}^{t} dt' \sum_{k=1}^{4} |\Psi_k(x,y) + \Psi_k(x+1,y) + \Psi_k(x-1,y) + \Psi_k(x,y+1) + \Psi_k(x,y-1)|, \tag{4.14}$$

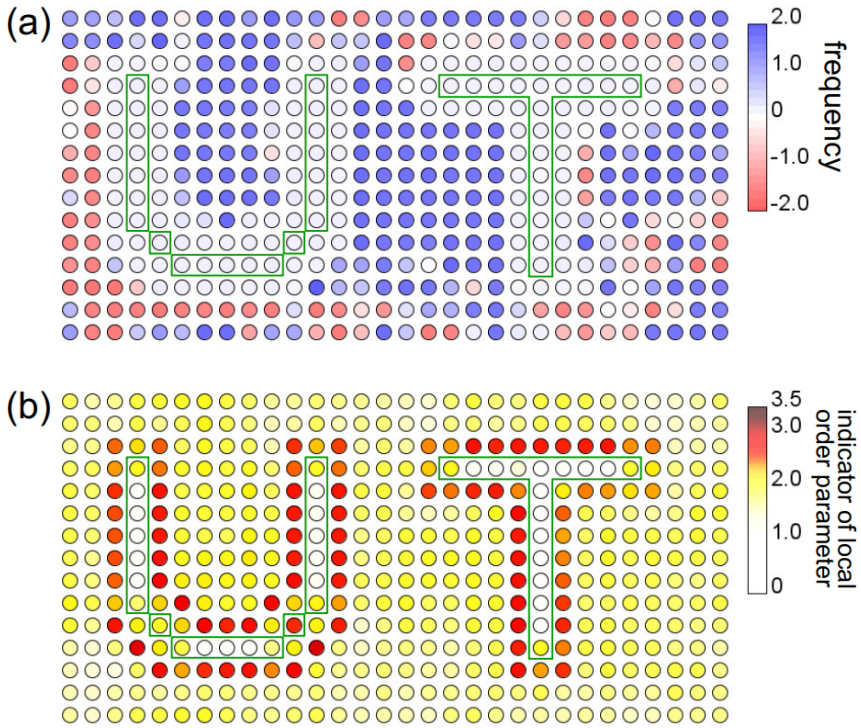

Figure 4.15: On-demand pattern designing using the topological synchronized state. (a) Frequency distribution in the on-demand pattern designing. The green boxes indicate the oscillators that are damped to realize the synchronization pattern of the shape of the characters, UT. We use the first model (4.3) and the parameters $u = -1$, $b = 0.3$, $\alpha = 0.5$, $\alpha_d = -100$, $\beta = 1$, $\omega_0 = 0.1$, and $\Delta\omega = 0.2$. (b) Indicators of local order parameters in the on-demand pattern desiging. The frequencies and indicators show that the synchronized oscillators are arranged in the desired pattern. These figures are adapted from K. Sone, Y. Ashida, and T. Sagawa, Topological synchronization of coupled nonlinear oscillators. Phys. Rev. Research **4,** 023211 (2022) [327] licensed under a Creative Commons Attribution 4.0 International License (http://creativecommons.org/licenses/by/4.0/).

where we set $T = 100$. This order parameter takes a large value around the synchronized oscillators as that in Eq. (4.13), while it does not distinguish the components of oscillators. However, in the first model, all the components of the edge oscillators are synchronized, and thus we do not need to judge which components are synchronized. Figure 4.15(b) shows the order parameters, which quantically show the synchronization of the oscillators around the effective boundaries. Therefore, these results indicate that one can realize an on-demand pattern of the synchronized oscillators by using the topological synchronization.

We note that the synchronization pattern cannot occur without using the topological properties of the nonlinear oscillators. In fact, if we consider $u = -3$ at which the linear coupling exhibits no edge modes, the synchronized pattern disappears even under the existence of the damped bulk oscillators as shown in Fig. 4.16. Therefore, the topology of the linear coupling is essential to realize the boundary-localized synchronization and the on-demand pattern designing.

4.5.2 Defect detection

Nonlinear oscillators in realistic setups can sometimes be damaged by external noises and stop their self-oscillation. Such defective oscillators may induce errors in the function of the oscillator system, and thus the detection of the defects can be useful to recover their functionality. We here propose that the topological synchronized state can be utilized in such defect detections. This is because the defective oscillators can create effective boundaries and make the neighbor

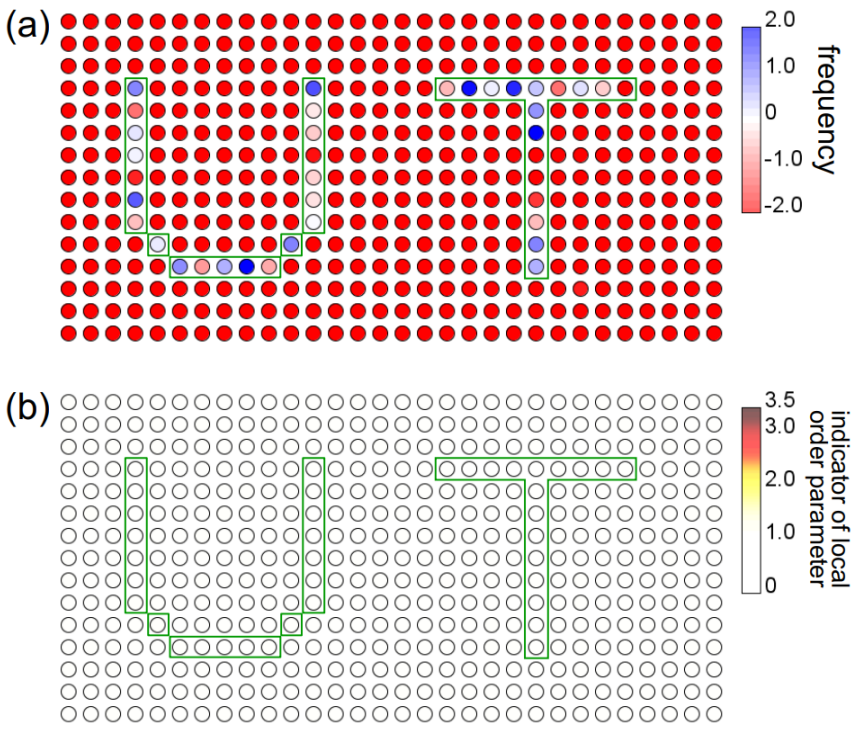

Figure 4.16: Absence of the synchronization pattern in a trivial system. (a) Frequency distribution in the on-demand pattern designing. The green boxes indicate the damped oscillators. We use the first model (4.3) and the parameters $u = -3$, $b = 0.3$, $\alpha = 0.5$, $\alpha_d = -100$, $\beta = 1$, $\omega_0 = 0.1$, and $\Delta\omega = 0.2$. (b) Indicators of local order parameters in the on-demand pattern desiging. We confirm the absence of the synchronization pattern. These figures are adapted from K. Sone, Y. Ashida, and T. Sagawa, Topological synchronization of coupled nonlinear oscillators. Phys. Rev. Research **4,** 023211 (2022) [327] licensed under a Creative Commons Attribution 4.0 International License (http://creativecommons.org/licenses/by/4.0/).

oscillators synchronized in the topological synchronized state. Thus, monitoring the appearance of the synchronized oscillators, one can judge that the oscillators surrounded by the synchronized oscillators are damaged and stop their oscillations (see Fig. 4.17(a)). Such defect detection can be advantageous because it can distinguish the defect of oscillators from the disorder of sensors that monitor the oscillator as shown in Fig. 4.17(b).

To demonstrate the possibility of such defect detection, we numerically calculate the oscillator dynamics of the first model under the periodic boundary condition and stop the oscillations of some oscillators at the time $t = 200$ by changing α into $\alpha_d = -100$. Figure 4.17(c) shows the local order parameter of synchronization after stopping the oscillations. We can confirm the emergence of the synchronized oscillators and judge the emergence of defective oscillators in the area surrounded by the synchronized oscillators. We also compare this with the situation that the sensors are broken. We assume that the broken sensors send no signals and thus the state variables of the corresponding oscillators are wrongly observed as zero. However, in such a case, one observes no synchronized oscillators. Therefore, one can distinguish the defect of oscillators from the disorder of sensors.

4.5.3 Possible experimental realization utilizing an electrical circuit

We also propose an electrical circuit that simulates the dynamics of our first model. As discussed in Sec. 2.4.4, one can derive the dynamics of voltages at each node in an electrical circuit from

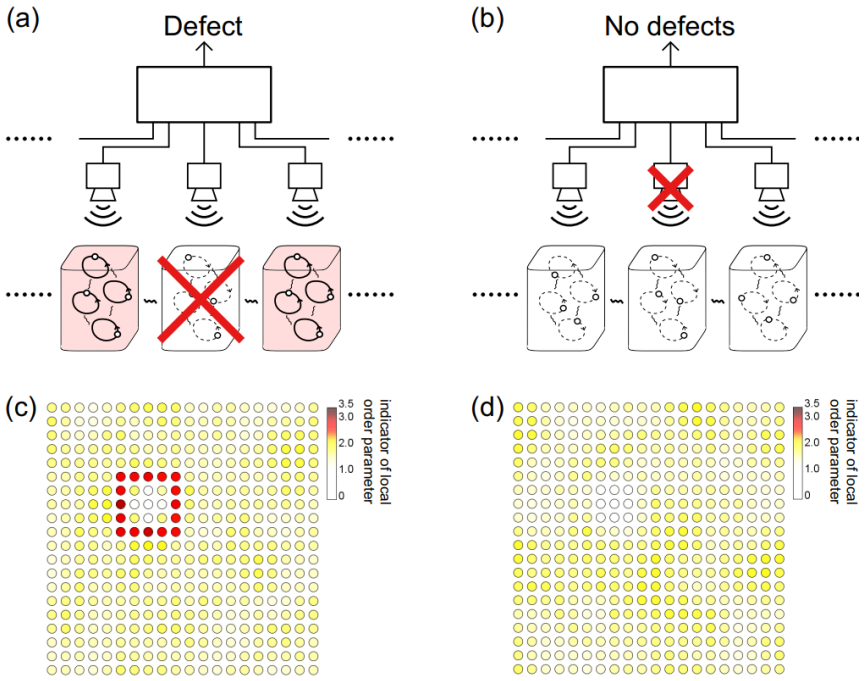

Figure 4.17: Defect detection using the topological synchronized state. (a,b) Schematics of the defect detection. The defective oscillators are detected from the synchronization of oscillators around the defect as shown in panel (a). In contrast, if the sensor is broken, we do not observe the synchronization as in panel (b). Therefore, one can distinguish the defect of oscillators and disorders in the sensors. (c) Indicators of local order parameters under the existence of defects. The oscillators surrounded by the synchronized oscillators (red sites) are disordered and stop their oscillations. We use the parameters $u = -1$, $b = 0.5$, $\alpha = 0.5$, $\alpha_d = -100$, $\beta = 1$, $\omega_0 = 0.1$, and $\Delta\omega = 0.2$. (d) Indicators of local order parameters under the existence of disordered sensors. There are no synchronized oscillators unlike in panel (c). We use the same parameters as in panel (c). These figures are adapted from K. Sone, Y. Ashida, and T. Sagawa, Topological synchronization of coupled nonlinear oscillators. Phys. Rev. Research **4,** 023211 (2022) [327] licensed under a Creative Commons Attribution 4.0 International License (http://creativecommons.org/licenses/by/4.0/).

Kirchhoff's law,

$$\frac{dV_a}{dt} = \frac{1}{C}\left[\sum_b C_{ab}(V_a - V_b) + C_a V_a\right] = \frac{1}{C}\sum_b J_{ab} V_b. \tag{4.15}$$

To realize lasing edge modes in an electrical circuit, we utilize negative impedance converters with current inversion (ICINs) [119], which can introduce nonreciprocal linear coupling ($C_{ab} \neq C_{ba}$). Figure 4.18(a) shows the electrical circuit whose dynamics is described by the Hamiltonian used in our first model. Each layer imitates the QWZ model, and resistors connecting two layers introduce the non-Hermitian coupling between them. Therefore, the effective Hamiltonian of this electrical circuit has a similar structure to that of exceptional edge modes and exhibits lasing edge modes.

The frequency dependences of the impedances of capacitors and inductors in Fig. 4.18(a) can be a barrier to directly realize the dynamics of our model of topological synchronization. Thus, we next construct a topological electrical circuit without using them. To this goal, we decompose the state variables into the real and imaginary parts $\Psi_j(\mathbf{x}) = V_{j1}(\mathbf{x}) + iV_{j2}(\mathbf{x})$. The real and imaginary couplings are converted into

$$C\Psi_j(\mathbf{x}) \quad \to \quad \begin{pmatrix} C & 0 \\ 0 & C \end{pmatrix} \begin{pmatrix} V_{j1}(\mathbf{x}) \\ V_{j2}(\mathbf{x}) \end{pmatrix}, \tag{4.16}$$

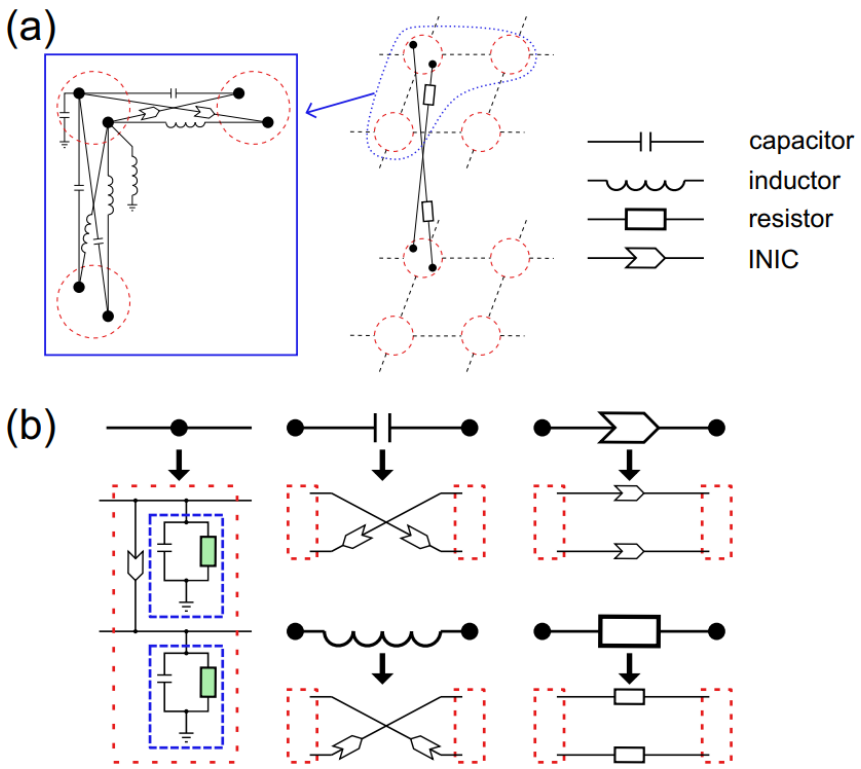

Figure 4.18: Electrical circuit realizing the topological synchronized state. (a) Electrical circuit realizing the linear coupling in the first model (4.3). The left panel shows the circuit elements realizing linear couplings encircled by the blue dashed curve in the middle panel. Each lattice point (red dashed circle) includes two nodes. We also consider the two layers of electrical circuits and couple them with the resistors. (b) Substitution rules to realize the topological synchronized state. We substitute each node in panel (a) with two coupled van der Pol circuits. We also substitute each circuit element with INICs or resistors. The red squares correspond to the pair of the van der Pol circuits in the left panel. These figures are adapted from K. Sone, Y. Ashida, and T. Sagawa, Topological synchronization of coupled nonlinear oscillators. Phys. Rev. Research **4,** 023211 (2022) [327] licensed under a Creative Commons Attribution 4.0 International License (http://creativecommons.org/licenses/by/4.0/).

$$iC\Psi_j(\mathbf{x}) \quad \to \quad \begin{pmatrix} 0 & -C \\ C & 0 \end{pmatrix} \begin{pmatrix} V_{j1}(\mathbf{x}) \\ V_{j2}(\mathbf{x}) \end{pmatrix}, \tag{4.17}$$

where C is real. These conversions can be done by the substitution of circuit elements depicted in Fig. 4.18(b).

Finally, we use van der Pol circuits [236, 330] to realize coupled nonlinear oscillators in the electrical circuit. Such a van der Pol circuit is constructed from nonlinear resistors. In fact, if the conductance of the nonlinear resistor is approximated as $\tilde{C}(V) = \alpha - \beta V^2 + \mathcal{O}(V^3)$, the dynamics of the van der Pol circuit is

$$C\frac{dV_i}{dt} = \tilde{C}(V_i)V_i + I_{\rm in} = (\alpha - \beta V_i^2)V_i + I_{\rm in} + (\text{higher-order terms}), \tag{4.18}$$

with $I_{\rm in}$ being the input current. If we ignore the higher-order term, the dynamics of the van der Pol circuit is equivalent to that of the Stuart-Landau oscillators. We introduce the van der Pol circuits to each node of the electrical circuit and obtain the electrical circuit imitating our first model.

4.6 Summary and discussions

In this chapter, we revealed the existence of the topological synchronized state of nonlinear oscillators, where the edge oscillators are synchronized, while the bulk ones are chaotic. We proposed and analyzed three models where we introduce topological linear couplings to nonlinear oscillators. The chaos of the bulk oscillators was also confirmed from the Lyapunov analysis. From the Lyapunov analysis, we also found the edge-localized Lyapunov vectors, which are the nonlinear counterparts of topological edge modes. Furthermore, we proposed applications of topological synchronization to pattern designing and defect detection. The topological synchronized state can be realized by using a topological electrical circuit with nonlinear circuit elements.

While we considered small lattice systems such as a 20×20 square lattice, the emergence of the topological synchronized state does not depend on the system size as long as one can distinguish the bulk and edge of the system. We also utilized the Stuart-Landau oscillators and the Dirichlet-type boundary conditions, the topological synchronization is also independent of the type of oscillators and the open boundary conditions (cf. the Neumann boundary condition) because of the robustness of topological properties against perturbations.

We discussed the bulk topology of the topological synchronized state from the band topology of the linear couplings. However, as we will discuss in the following chapter, one can define the nonlinear topological invariant. In fact, we can show that the nonlinear Chern number defined in Chapter 5 becomes nonzero in the second model of the topological synchronized state (Appendix B.4). Thus, identifying the correspondence between the nonlinear topological invariants and the topological synchronized state remains an intriguing future problem. By identifying the nonlinear topological invariant characterizing the topological synchronization, one can possibly extend the topological synchronization to the nonlinearity-induced transition from desynchronization to synchronization. It may also be possible to realize the topological synchronization in identical oscillators with Hermitian linear couplings.

Chapter 5

Nonlinearity-induced topological phase transition characterized by the nonlinear Chern number (removed for the future publication in a scientific journal)

This chapter is removed because the results will be published in a scientific journal in five years.

In this chapter, we propose the nonlinear extension of the Chern number that characterizes the topology of two-dimensional nonlinear systems. We also show its bulk-boundary correspondence by analyzing minimal models of nonlinear Chern insulators. In weakly nonlinear systems, we can mathematically show the bulk-boundary correspondence of the nonlinear Chern number. In a strongly nonlinear regime, we find the nonlinearity-induced topological phase transitions in two-dimensional systems and that the nonlinear Chern number can predict such nonlinearity-induced transitions. We analytically show the bulk-boundary correspondence in semi-infinite systems and numerically confirm it in finite systems in such strongly nonlinear regimes. We also propose the experimental setup to observe the nonlinear edge modes by using the quench dynamics in topological photonics.

Chapter 6

Transition from topological to chaos in the nonlinear Su-Schrieffer-Heeger model (removed for the future publication in a scientific journal)

This chapter is removed because the results will be published in a scientific journal in five years.

In this chapter, we reveal the transition from topological to chaos in zero modes of nonlinear topological insulators and discuss its relation to the breakdown of the bulk-boundary correspondence in nonlinear systems. Specifically, we analyze the nonlinear Su-Schrieffer-Heeger (SSH) model, which is a minimal model of a one-dimensional nonlinear topological insulator. We derive the dynamical system describing zero modes in the nonlinear SSH model and show that it exhibits a chaos transition. We further investigate the extended nonlinear SSH model that can show the higher nonlinear topological invariant and discuss the correspondence between the topological invariant and the dimension of the stable manifold in the dynamical system of zero modes.

Chapter 7

Conclusion and discussion

7.1 Conclusion

In this thesis, we extended the topological edge modes and their bulk-boundary correspondence to nonlinear systems. Specifically, we found the topological synchronization in nonlinear oscillators, which is a typical dissipative nonlinear system. We also proposed the nonlinear extension of topological invariants such as the Chern number and the winding number and analyzed its bulk-boundary correspondence.

In Chapter 4, we proposed the topological synchronized state where the edge oscillators are synchronized while the bulk ones are desynchronized. Such topological synchronized states are realized in periodically aligned nonlinear oscillators with linear couplings described by the Hamiltonian of topological insulators. Specifically, we proposed three models of the topological synchronized state, a model utilizing the Hamiltonian of exceptional edge modes [27], a model utilizing a non-Hermitian Chern insulator, and a model utilizing inhomogeneous oscillators and Hermitian linear couplings. The existence of the topological synchronized state indicates the ubiquity of the topological synchronized state in nonlinear oscillators. We also conducted the Lyapunov analysis of the topological synchronized state to clearly show the chaos in the bulk oscillators. We also found the edge-localized Lyapunov vectors which are nonlinear counterparts of topological edge modes. We also proposed applications of the topological synchronized state to the on-demand pattern designing, the defect detection, and the experimental setup using an electrical circuit.

(Further detailed discussions and future perspectives are included in the full thesis, while they are removed because they are related to the results that will be published in scientific journals.)

Appendix A

Exceptional edge mode and topological surface laser

In our previous study [27], we have proposed an unconventional mechanism to protect gapless edge modes in non-Hermitian systems that we name exceptional edge modes. We further extend the notion of exceptional edge modes to three-dimensional systems and reveal the existence of exceptional *surface* modes. We also propose their application to topological lasers. Such a topological surface laser can be advantageous compared to those proposed in previous studies [22, 23, 27, 109, 136–138, 140], because it needs no symmetries and judicious gains to robustly work against the existence of disorders.

In this chapter, we first review the fundamental properties of exceptional edge modes based on some minimal models analyzed in Ref. [27]. Then, we explain its extension to three-dimensional systems and possible applications to photonic systems.

A.1 Exceptional edge modes in two dimension

Exceptional edge modes are protected by the nontrivial topology of the branch-point structure around exceptional points in their dispersions. Therefore, exceptional edge modes can robustly exist against disorders even with a topologically trivial bulk. Typically, one can construct the Hamiltonian of exceptional edge modes from a Chern insulator and its time-reversal counterpart combined by non-Hermitian couplings. In the following section, we discuss the properties of exceptional edge modes based on a lattice model constructed by this strategy.

A.1.1 Toy model of the exceptional edge modes

A prototypical model of exceptional edge modes is constructed from layers of the QWZ model. We combine two layers of the QWZ model by Hermitian couplings. We also prepare their time-reversal counterparts. Finally, we combine the layers of the QWZ model and their time-reversal counterpart by non-Hermitian couplings. Denoting the Hamiltonian of the QWZ model by H_{QWZ}, the Hamiltonian of the prototypical model is described as

$$H = \begin{pmatrix} H_{\mathrm{QWZ}} & cI_2 & ia\beta\sigma_x & -i\gamma\sigma_x \\ cI_2 & H_{\mathrm{QWZ}} & i\gamma\sigma_x & ia\beta'\sigma_x \\ ia\beta\sigma_x & -i\gamma\sigma_x & H^*_{\mathrm{QWZ}} & cI_2 \\ i\gamma\sigma_x & ia\beta'\sigma_x & cI_2 & H^*_{\mathrm{QWZ}} \end{pmatrix}, \tag{A.1}$$

where I_2 is a 2×2 identity matrix, and σ_i is the ith component of the Pauli matrices. We note that this Hamiltonian has the time-reversal symmetry and thus its conventional bulk topology is classified by the $\mathbb{Z}_2$ index (see Sec. 2.1.2). However, this model has zero topological invariant and thus the exceptional edge modes are independent of the conventional bulk topology.

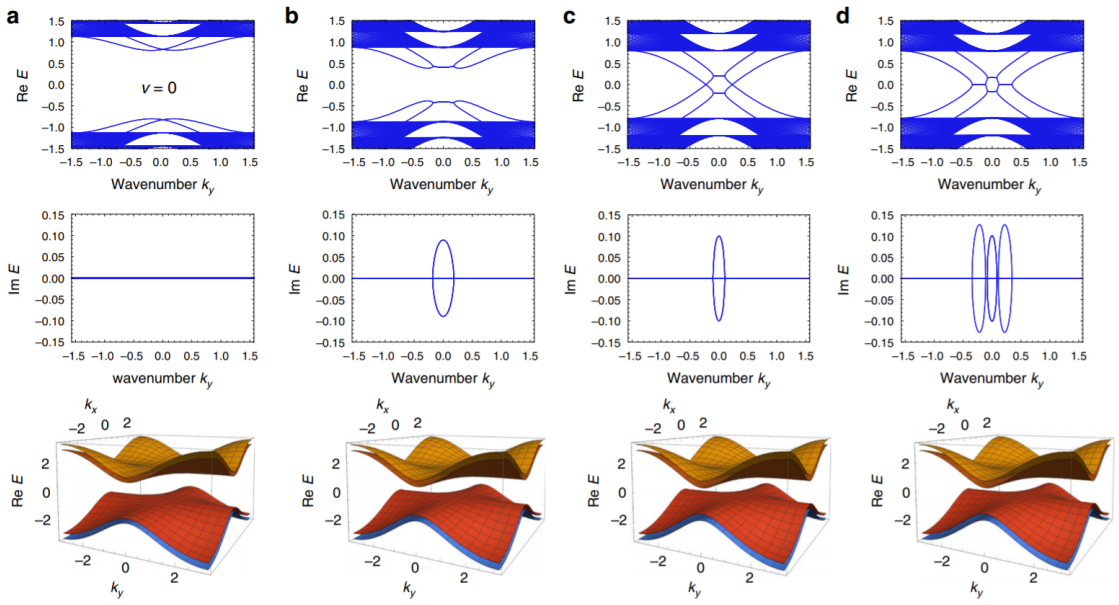

Figure A.1: Exceptional edge modes and their independence of the bulk topology. The real and imaginary parts of the eigenvalues are shown in the upper and middle panels, respectively. The bottom panels represent the bulk bands. (a) Band structure of the toy model (A.1) without non-Hermitian terms. The band is gapped and thus the bulk topology is trivial. The parameters used are $u = -1$, $c = 0.2$, $\gamma = 0.8$, and $\beta = \beta' = 0$. (b) Band structure with small non-Hermitian couplings ($\beta = 0.81$, $\beta' = 0.63$). (c) Band structure at the critical strength of the non-Hermitian coupling ($\beta = 0.9$, $\beta' = 0.7$). The gapless modes appear at this critical parameter, while the bulk bands are still gapped. Thus, the exceptional edge modes are independent of the bulk topology. (d) Band structure with stronger non-Hermitian couplings ($\beta = 0.909$, $\beta' = 0.707$). We can find exceptional points at $\mathrm{Re}\, E = 0$, which protect the gapless modes from gao opening. These figures are adapted from K. Sone, Y. Ashida, and T. Sagawa, Exceptional non-Hermitian topological edge mode and its application to active matter. *Nat. Commun.* **11,** 5745 (2020) [27] licensed under a Creative Commons Attribution 4.0 International License (http://creativecommons.org/licenses/by/4.0/).

One can confirm the independence of the conventional bulk topology by calculating the dispersion relations of the prototypical model at different strengths of non-Hermitian couplings. Figure A.1 shows the band structures under the open (periodic) boundary condition in the x (y) direction. If there are no non-Hermitian terms ($a = 0$), the bands are gapped, which indicates that the model has a trivial bulk. As the non-Hermitian term becomes larger, the upper and lower bands approach each other and the gap becomes smaller. At the critical strength of the non-Hermitian coupling, one can obtain gapless edge modes with exceptional points, i.e., exceptional edge modes. Meanwhile, the bulk bands do not close gaps. Therefore, the bulk topology is always trivial in the parameter region

A.1.2 Symmetry protection of the exceptional edge modes

Exceptional edge modes are protected by the nontrivial topology of the exceptional points in their dispersion relation. Since the edge of a two-dimensional system is regarded as a one-dimensional system, the stability of the exceptional point is determined by its topological invariant in one-dimensional systems. The classification table of exceptional points studied in a previous study [151] tells us that topologically protected exceptional points can appear under proper symmetries, such as the PT, CP, chiral symmetries, and pseudo-Hermiticity. Therefore, the exceptional edge modes can also be topologically protected under the existence of these symmetries.

More interestingly, there are degrees of freedom in the definition of the PT and CP symmetries,

and unconventional definitions of the PT and CP symmetries are essential to topologically protect the exceptional edge modes. On one hand, the conventional PT and CP symmetries are defined as

$$\begin{aligned} \text{(PT symmetry) } PTH(\mathbf{k})(PT)^{-1} &= H^*(\mathbf{k}), & \text{(A.2)} \\ \text{(CP symmetry) } CPH(\mathbf{k})(CP)^{-1} &= -H^*(\mathbf{k}), & \text{(A.3)} \end{aligned}$$

with $H(\mathbf{k})$ being the Bloch Hamiltonian. In this definition, P corresponds to the parity inversion. On the other hand, by using the mirror operators P' (resp. P'') in the y (resp. x) direction, one can define the modified PT and CP symmetries as

$$\begin{aligned} \text{(modified PT symmetry 1) } P'TH(k_x,k_y)(P'T)^{-1} &= H^*(-k_x,k_y), & \text{(A.4)} \\ \text{(modified PT symmetry 2) } P''TH(k_x,k_y)(P''T)^{-1} &= H^*(k_x,-k_y), & \text{(A.5)} \\ \text{(modified CP symmetry 1) } CP'H(k_x,k_y)(CP')^{-1} &= -H^*(-k_x,k_y), & \text{(A.6)} \\ \text{(modified CP symmetry 2) } CP''H(k_x,k_y)(CP'')^{-1} &= -H^*(k_x,-k_y). & \text{(A.7)} \end{aligned}$$

If we consider a cylindrical system with open boundaries in the x direction, the wavenumber k_x is no longer a good quantum number. Therefore, the modified PT and CP symmetries 1 are also reduced to the PT and CP symmetries in such a cylindrical system, where the band structures of the exceptional edge modes are calculated. The same reduction can occur for the modified PT and CP symmetries 2 when we consider a cylindrical system with open boundaries in the y direction.

The minimal model has both the conventional and modified PT and CP symmetries,

$$\begin{aligned} PT &= \sigma_x \otimes I_2 \otimes \sigma_z,\ PTH(\mathbf{k})(PT)^{-1} = H^*(\mathbf{k}), & \text{(A.8)} \\ P'T &= I_2 \otimes I_2 \otimes \sigma_z,\ P'TH(k_x,k_y)(P'T)^{-1} = H^*(-k_x,k_y), & \text{(A.9)} \\ P''T &= \sigma_z \otimes I_2 \otimes I_2,\ P''TH(k_x,k_y)(P''T)^{-1} = H^*(k_x,-k_y), & \text{(A.10)} \\ CP &= \sigma_z \otimes \sigma_z \otimes \sigma_y,\ CPH(\mathbf{k})(CP)^{-1} = -H^*(\mathbf{k}), & \text{(A.11)} \\ CP' &= \sigma_y \otimes \sigma_z \otimes \sigma_y,\ CP'H(k_x,k_y)(CP')^{-1} = -H^*(-k_x,k_y), & \text{(A.12)} \\ CP'' &= \sigma_x \otimes \sigma_z \otimes \sigma_x,\ CP''H(k_x,k_y)(CP'')^{-1} = -H^*(k_x,-k_y). & \text{(A.13)} \end{aligned}$$

The model also has the chiral symmetry and pesudo-Hermiticity,

$$\begin{aligned} \Gamma &= \sigma_x \otimes \sigma_z \otimes \sigma_x,\ \Gamma H(\mathbf{k})\Gamma^{-1} = -H^\dagger(\mathbf{k}), & \text{(A.14)} \\ \eta &= \sigma_z \otimes I_2 \otimes I_2,\ \eta H(\mathbf{k})\eta^{-1} = H^\dagger(\mathbf{k}). & \text{(A.15)} \end{aligned}$$

Therefore, exceptional edge modes can be protected by these symmetries.

To confirm the symmetry protection of the exceptional edge modes, we numerically calculate the dispersion relation of the exceptional edge modes under the existence of disorders in our previous study [27]. Figure A.2 shows the numerical results. In panel (b), we consider random real on-site potentials and imaginary noises in the non-Hermitian coupling. These disorders are denoted by $a(x)\{I_2,\sigma_z\}\otimes\{I_2,\sigma_z\}\otimes\{I_2,\sigma_z\}$ and $ib(x)\{\sigma_x,i\sigma_y\}\otimes\{I_2,\sigma_z\}\otimes\{\sigma_x,i\sigma_y\}$, where $a(x)$ and $b(x)$ are random real values determined from the uniform distribution ranging $[-W,W]$, and the brackets indicate that we use all the combinations made of either one in each bracket. Such disorders preserve the modified PT symmetries, while they break the conventional PT and CP symmetries. The existence of exceptional edge modes under the existence of these noises indicates that gapless edge modes can be protected by the modified PT symmetries even without the conventional PT and CP symmetries. Meanwhile, in panel (c), we consider random real coupling $b(x)\{\sigma_x,i\sigma_y\}\otimes\{I_2,\sigma_z\}\otimes\{\sigma_x,i\sigma_y\}$, which breaks all the symmetries above. Therefore, gapless edge modes disappear in this case. The disappearance of the exceptional edge modes indicates that the topological protection of the exceptional edge modes requires proper symmetries.

We can qualitatively discuss the reason why the conventional PT and CP symmetries are irrelevant to the topological protection of the exceptional edge modes from the fact that the P

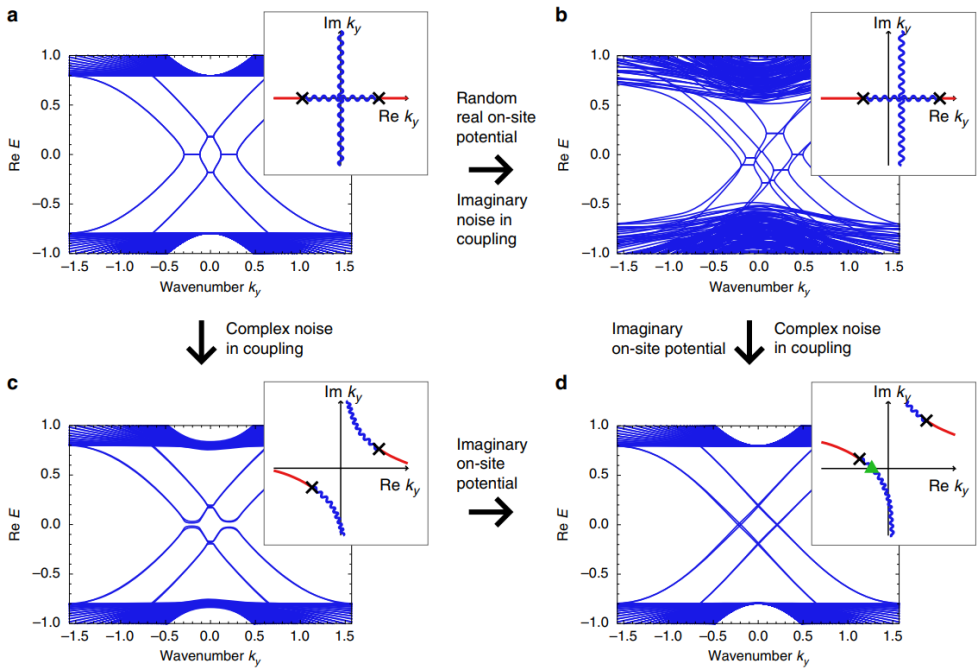

Figure A.2: Robustness of the exceptional edge modes. In the insets, black crosses are the exceptional points, blue wave curves represent the degeneracy of the real parts of eigenvalues, and the red curve represents the degeneracy of the imaginary part. The behaviors on the $\mathrm{Re}\, k_y$ axis are reflected in band structures. (a) Band structure without disorders. The parameters used are $u = -1$, $c = 0.2$, $\beta = 0.14$, $\beta' = 0.06$, and $\gamma = 0.05$. (b) Band structure under the existence of symmetry-protecting disorders. We still obtain gapless edge modes, which indicates the robustness of exceptional edge modes under the existence of symmetries. (c) Band structure under the existence of symmetry-breaking disorders. The band is gapped, and thus the topological protection of exceptional edge modes requires symmetries. (d) Gapless modes without exceptional points. The mechanism of the robustness is not fully elucidated. These figures are adapted from K. Sone, Y. Ashida, and T. Sagawa, Exceptional non-Hermitian topological edge mode and its application to active matter. *Nat. Commun.* **11,** 5745 (2020) [27] licensed under a Creative Commons Attribution 4.0 International License (http://creativecommons.org/licenses/by/4.0/).

operator maps an edge mode to another edge mode localized at the opposite side. Therefore, we must consider two exceptional points in the dispersion of the exceptional edge modes at both sides. Then, the topology of exceptional points in one-dimensional bands with the PT or CP symmetries is classified by a $\mathbb{Z}_2$ invariant,

$$\nu = \mathrm{sgn}(\det H(k_0 - \delta)H(k_0 + \delta)), \tag{A.16}$$

where k_0 is wavenumber at which the exceptional point appears, and δ is a small constant. Such a $\mathbb{Z}_2$ invariant must be trivial because the sum of the contributions from two exceptional points must be even. Therefore, the conventional PT and CP symmetries cannot protect the exceptional edge modes. In contrast, the mirror operator used in the modified PT and CP symmetries maps an edge mode to another edge mode localized at the same side and thus we can separately discuss the stabilities of the exceptional points in the dispersions of the exceptional edge modes at the right and left ends. In this case, the $\mathbb{Z}_2$ invariant can be nontrivial, and thus the modified PT and CP symmetries can protect the exceptional edge modes.

A.1.3 Topological laser utilizing exceptional edge modes

From Fig. A.1, one can see that exceptional edge modes can have large positive imaginary parts of eigenvalues even if the bulk bands have zero imaginary parts. Such characteristic complex

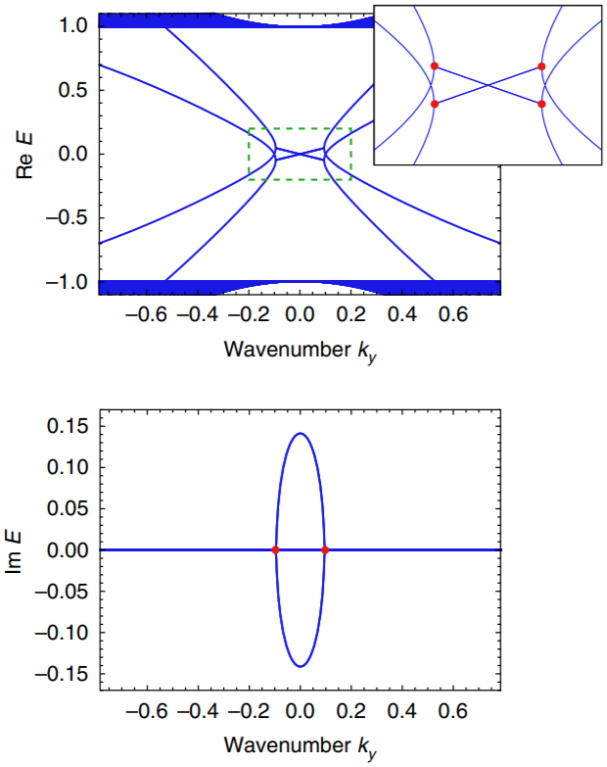

Figure A.3: Band structure of the topological laser utilizing exceptional edge modes (A.17). The red points in the inset are the exceptional points. The parameters used are $u = -1$, $\beta = 0.2$, and $\beta' = 0.1$. These figures are adapted from K. Sone, Y. Ashida, and T. Sagawa, Exceptional non-Hermitian topological edge mode and its application to active matter. *Nat. Commun.* **11,** 5745 (2020) [27] licensed under a Creative Commons Attribution 4.0 International License (http://creativecommons.org/licenses/by/4.0/).

dispersions lead to the amplification of only the edge modes. By using the amplification of the exceptional edge modes, one can realize topological lasers that can amplify the edge sites and transfer the lasing wave packet along the edge of the sample.

Specifically, if we consider the Hamiltonian

$$H = \begin{pmatrix} 2H_{\mathrm{QWZ}} & i\beta\sigma_x \\ i\beta'\sigma_x & H^*_{\mathrm{QWZ}} \end{pmatrix}, \tag{A.17}$$

with H_{QWZ} being the Hamiltonian of the QWZ model and β and β' being real parameters, we can realize the band structure in Fig. A.3. One can confirm larger imaginary parts of the eigenvalues of the exceptional edge modes than those of the bulk modes. One can also check the nonzero slope of the real parts of eigenvalues of the exceptional edge modes, which is essential to realize the unidirectional propagation of the lasing wave packet.

Figure A.4 shows the snapshots of the numerical simulation of the model (A.17). Starting from the random initial condition, the model exhibits amplified edge oscillations, which is a defining feature of topological lasers. Starting from the one-site excitaion, one can also check the unidirectional propagation of the wave packet and thus can realize a robust transport of the lasing wave packet against disorders.

Unlike some previous studies [22, 23, 137], the advantage of realizing topological lasers by the exceptional edge mode is that they need no judicious gains at the edge of the system. Such topological lasers without judicious gains have also been proposed by symmetry-protected non-Hermitian edge modes [109, 140], while they exhibit flat real dispersions and thus cannot realize the unidirectional propagation of lasing wave packets. In fact, we have shown in our previous

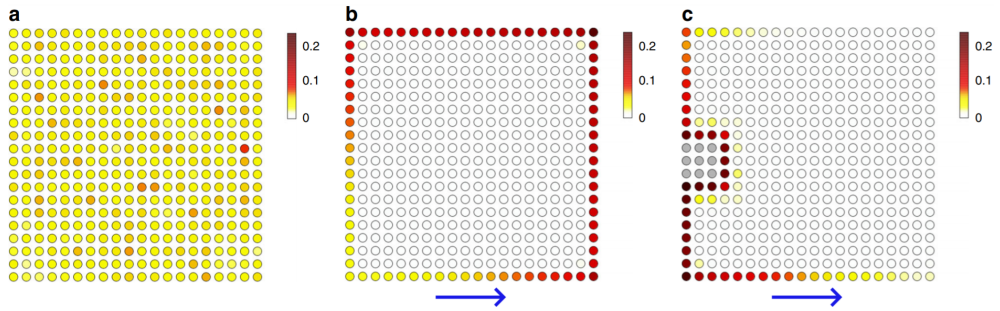

Figure A.4: Dynamics of the topological laser utilizing exceptional edge modes. The color of each site represents the relative amplitude, whose squared sum is unity. (a) Snapshot without the non-Hermiticity. We use the parameters $u = -1$ and $\beta = \beta' = 0$. We observe no lasing edge modes. (b) Spontaneous emergence of lasing edge modes from a random initial state. We use the parameters $u = -1$ and $\beta = 0.2$ $\beta' = 0.1$. (c) Backscattering-free propagation of the lasing wave packet. We use the parameters $u = -1$ and $\beta = 0.9$ $\beta' = 0.8$. The gray site represents the vacuum. The lasing wave packet avoids such a defect at the edge and propagates along the edge of the system. These figures are adapted from K. Sone, Y. Ashida, and T. Sagawa, Exceptional non-Hermitian topological edge mode and its application to active matter. *Nat. Commun.* **11,** 5745 (2020) [27] licensed under a Creative Commons Attribution 4.0 International License (http://creativecommons.org/licenses/by/4.0/).

paper [27] that exceptional edge modes are required to realize the nonzero group velocity of the lasing wave packets.

A.2 Exceptional surface modes in three dimension and topological surface laser

Exceptional edge modes in two-dimensional systems can realize topological lasers, while they require symmetries for their topological protection. Since such symmetries can be a barrier to realize topological lasers in a wide range of photonic setups, topological lasers without any symmetries can be of practical advantage.

In this section, we show that the three-dimensional extension of exceptional edge modes, i.e., exceptional surface modes can realize topological lasers with neither symmetries nor judicious gains. Specifically, we construct lattice models that exhibit gapless surface modes that have exceptional points in their bands. Such exceptional points protect the gapless surface modes from opening gaps. Since the surface of a three-dimensional system is an effectively two-dimensional system, and exceptional points can be topologically protected without symmetries in two-dimensional systems, exceptional surface modes robustly exist against disorders without the help of symmetries. We analyze the lattice models and confirm the amplification of the surface modes. We also propose a possible photonic setup to realize a topological laser using exceptional surface modes.

A.2.1 Prototypical model of exceptional mode topological surface laser

In general, one can construct a Hamiltonian of a topological laser using exceptional surface modes from that of a weak topological insulator with a non-Hermitian spin coupling. A weak topological insulator is composed of stacked layers of spin Hall systems. Then, the boundaries that are not parallel to the layers can exhibit gapless surface modes, which is the characteristic feature of the weak topological insulator (see Sec. 2.1.3). By introducing the non-Hermitian spin coupling to the weak topological insulator, one can modify the Dirac dispersion of the gapless surface modes and split the Dirac point into a pair of exceptional points. Those exceptional points can protect the gapless surface modes even if the symmetries (e.g. the time-reversal symmetries) in the original

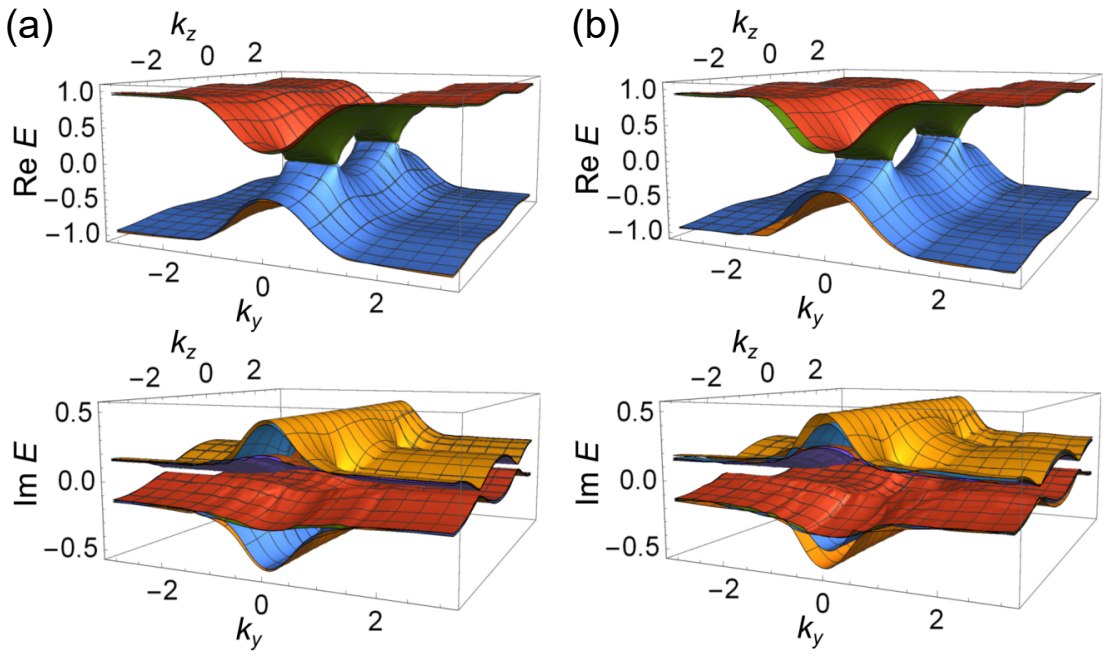

Figure A.5: Surface band structures of the toy model of a topological surface laser (A.18). (a) Surface band structure of the topological laser. We only show the four bands that are closest to the $\mathrm{Re}\, E = 0$ plane in the upper panel. We also restrict the number of bands that are shown in the lower panel to eight. We use the parameters $u = -1$, $c = 0.3$, $\gamma = 0.5$, and $W_d = W_a = 0.1$. (b) Surface band structure with all the possible noise. The noise strength is $W = 0.1$. There still exist exceptional surface modes, which indicates their robustness independent of the symmetry. These figures are adapted from K. Sone, Y. Ashida, and T. Sagawa, Exceptional mode topological surface laser. *Phys. Rev. B* **105,** 235426 (2022) [343] Copyright 2022 by the American Physical Society.

weak topological insulator are broken. Furthermore, by judiciously choosing the form of the non-Hermitian spin coupling, one can realize exceptional surface modes with larger imaginary parts of eigenvalues than those of bulk modes, which is a prerequisite for a topological laser amplifying the surface modes.

To numerically demonstrate the possibility of topological lasers protected by exceptional points, we construct and analyze a lattice model by following the above construction procedure. The Hamiltonian of the lattice model is described in the wavenumber space as

$$H(\mathbf{k}) = (u + \cos k_x + \cos k_y) I \otimes \sigma_z + \sin k_x \sigma_z \otimes \sigma_x + \sin k_y I \otimes \sigma_y + (c \cos k_z + i\gamma)\sigma_y \otimes \sigma_x, \tag{A.18}$$

where I is a 2×2 identity matrix and σ_i is the ith component of the Pauli matrices. We construct this Hamiltonian in the following procedure; we first consider the Hamiltonian of a spin Hall system $H_{\mathrm{SH}} = (u + \cos k_x + \cos k_y) I \otimes \sigma_z + \sin k_x \sigma_z \otimes \sigma_x + \sin k_y I \otimes \sigma_y$ (this spin Hall system is composed of the QWZ model [94] and its time-reversal counterpart [60]). Then, we introduce the Hermitian interlayer coupling $c \cos k_z \sigma_y \otimes \sigma_x$. Finally, we introduce the non-Hermitian spin coupling $i\gamma \sigma_y \otimes \sigma_x$ and obtain the Hamiltonian of the topological laser. We assume that all the parameters, u, c, and γ are real.

We numerically calculate the surface band structure of the lattice model (A.18) and confirm the existence of exceptional surface modes. We here impose the open boundary condition in the x direction and the periodic boundary conditions in the y and z directions. We also introduce random complex on-site potentials and noises in the spin coupling to investigate the robustness of the exceptional surface modes. Specifically, we add a random complex value whose real and imaginary parts are determined from the uniform distribution ranging $[-W_d, W_d]$ to each diagonal

term of the Hamiltonian. We also add a random real value determined from the uniform distribution ranging $[-W_a, W_a]$ to each off-diagonal term that couples the first and fourth components or the second and third ones at the same site. Figure A.5(a) shows the complex surface band structure of the lattice model. We confirm the existence of gapless modes with four exceptional points in their bands. These exceptional points protect the gapless surface modes from opening gaps under the existence of disorders. We also check that the exceptional surface modes have larger imaginary parts of eigenvalues around $k_y = 0$ than those of the bulk modes. Therefore, one can amplify only these exceptional surface modes.

We further confirm the robustness of the exceptional surface modes against disorders by numerically calculating the surface band structure under the existence of all possible on-site noises. Since the system has four sublattices, such on-site noises can be described by a 4×4 matrix depending on the site index. We determine the real and imaginary parts of each component following the uniform distribution ranging $[-W, W]$, respectively. Figure A.5(b) shows the surface band structure under the existence of these noises. One can still confirm the existence of the exceptional surface modes. Since the noises break any symmetries relevant to the topological classification of the exceptional points [151], the existence of the exceptional surface modes in Fig. A.5 indicates that exceptional surface modes can be topologically protected without symmetries.

A.2.2 Exceptional mode topological surface laser exhibiting propagating wave packets

While the prototypical model in the previous section exhibits exceptional surface modes with large imaginary parts of eigenvalues, the dispersions between the exceptional points are almost flat, which indicates that the lasing wave packets cannot propagate along the surface of the prototypical model. The propagation of the lasing wave packet is of applicational use to transfer the amplified light. Thus, we next propose the topological surface laser that exhibits propagating lasing wave packets.

Specifically, we consider the following Hamiltonian

$$\begin{aligned} H(\mathbf{k}) &= (u + \cos k_x + \cos k_y)\,(aI \otimes \sigma_z + b\sigma_z \otimes \sigma_z) + \sin k_x\,(bI \otimes \sigma_x + a\sigma_z \otimes \sigma_x) \\ &\quad + \sin k_y\,(aI \otimes \sigma_y + b\sigma_z \otimes \sigma_y) + (c\cos k_z + i\gamma)\sigma_y \otimes \sigma_x. \end{aligned} \tag{A.19}$$

This Hamiltonian has different strength of hoppings between the up and down (effective) spins, which is parameterized by b. Figure A.6(a) shows the dispersion relation of the Hamiltonian under the open boundary condition in the x direction and the periodic boundary conditions in the y and z directions. We confirm the existence of exceptional surface modes with nonzero group velocity in the y direction around $k_y = 0$, which enables the propagation of the lasing wave packets.

We also simulate the dynamics of the model (A.19) and demonstrate the propagation of the lasing wave packet. Via the inverse Fourier transformation of the Hamiltonian (A.19), we obtain the real-space description. Then, we perform the fourth-order Runge-Kutta simulation of the real-space Hamiltonian. We set the time step as $dt = 0.001$ and consider a $10 \times 10 \times 10$ cubic lattice with open boundaries in all the x, y, and z directions. We further introduce the empty sites that express the deformation of the boundary geometry. We consider the initial condition where only the surface sites at $(x, y, z) = (5, 10, z)$ with z being $1 \leq z \leq 10$ are excited. Figure A.6(b) shows a snapshot of the simulation. In this numerical simulation, we confirm that a wave packet is localized at and propagates along the surface of the system. We also check that the wave packet propagates without backscattering at the empty sites on the surface, which indicates the robustness of the exceptional surface modes against the modulation of the boundary geometry.

We can also confirm the robustness against disorders as in the prototypical model. Specifically, we introduce all the possible on-site noises as in Fig. A.5(b). Figure A.6(c) shows the snapshot of the numerical simulation. We still confirm the propagation of the lasing wave packet under the existence of the disorders. Since such disorders break any $\mathbb{Z}_2$ symmetries and translational symmetry, the robustness of the lasing wave packet against the disorders indicates that the exceptional surface modes are topologically protected even without symmetries.

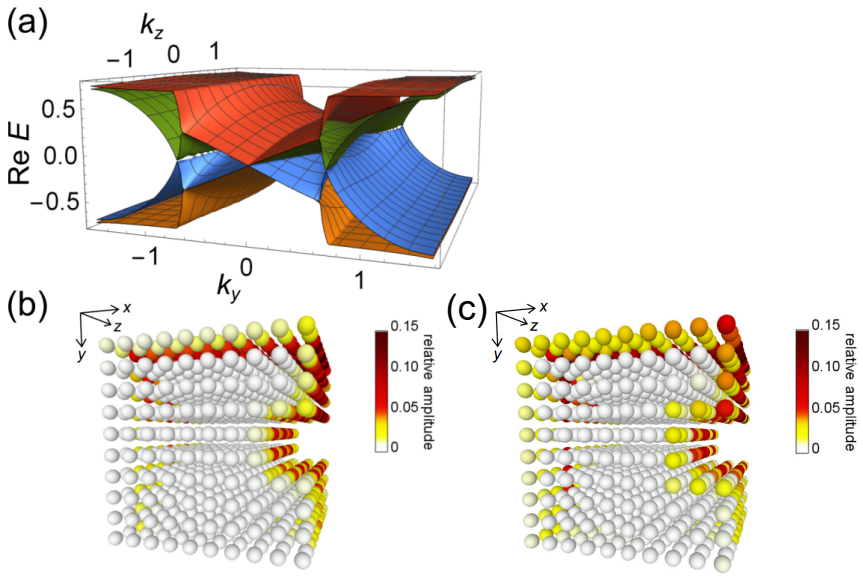

Figure A.6: Topological surface laser with propagating wave packets (A.19). (a) Real part of the surface band structure. We can confirm the nonzero slope of the dispersion relations of the surface modes, which enables the propagation of the wave packet. We use the parameters $u = -1$, $a = 1.5$, $b = 0.5$, $c = 0.2$, and $\gamma = 0.9$. (b) Dynamics of the propagation of the lasing wave packet. The color of each site represents the relative amplitude, whose squared sum is unity. (c) Robustness of the lasing wave packet against disorders. The strength of disorder is $w = 0.1$. These figures are adapted from K. Sone, Y. Ashida, and T. Sagawa, Exceptional mode topological surface laser. *Phys. Rev. B* **105,** 235426 (2022) [343] Copyright 2022 by the American Physical Society.

A.2.3 Possible photonic setup of exceptional mode topological surface laser

While in the previous sections, we have analyzed toy models of topological lasers, we also propose a more realistic setup of a topological surface laser in a photonic system. To construct a topological surface laser, we first consider a photonic counterpart of a weak topological insulator. Such a photonic weak topological insulator is realized by the accumulation of layers of ring-resonator arrays [165] that imitate the dynamics of multi-layers of quantum spin Hall systems (see Sec. 2.1.2). Specifically, we consider three types of layers of ring-resonator arrays depicted in Fig. A.7. Each layer realizes a different artificial gauge field (phases gained via the hoppings), which is determined by the length of waveguides between resonators. We note that each layer does not correspond to the layer of a quantum spin Hall system, and instead resonators aligned on a plane parallel to the xy plane realize a layer of a photonic quantum spin Hall effect.

We also realize the non-Hermitian spin coupling by introducing a waveguide segment with mirrors to each ring resonator and homogeneous gains. Such a waveguide segment is proposed in previous studies [140], and light reflected at the mirror realizes the coupling between clockwise and anti-clockwise modes, which play a role of effective spin degrees of freedom. One can also tune the phase of the non-Hermitian spin coupling by changing the length of the waveguide segment. We here realize alternate signs of the non-Hermitian spin couplings that are different between odd- and even-numbered rows by tuning the length of the waveguide segments.

Finally, we obtain the photonic system that imitates a weak topological insulator with non-Hermitian spin couplings and thus can be used as a topological surface laser. The effective Hamiltonian of the photonic system is

$$\begin{aligned} H &= \sum_{\mathbf{r},s=\pm} (a_x e^{is\phi y} \hat{c}^\dagger_{\mathbf{r},s} \hat{c}_{\mathbf{r}+\mathbf{e}_x,s} + a_y \hat{c}^\dagger_{\mathbf{r},s} \hat{c}_{\mathbf{r}+\mathbf{e}_y,s}) + \text{H.c.} \\ &\quad + \sum_{\mathbf{r}} [a_z \sin(\phi y)(\hat{c}^\dagger_{\mathbf{r},+} \hat{c}_{\mathbf{r}+\mathbf{e}_z,-} + \hat{c}^\dagger_{\mathbf{r},-} \hat{c}_{\mathbf{r}+\mathbf{e}_z,+}) + \text{H.c.} + i\beta \sin(\phi y)(\hat{c}^\dagger_{\mathbf{r},+} \hat{c}_{\mathbf{r},-} + \hat{c}^\dagger_{\mathbf{r},-} \hat{c}_{\mathbf{r},+})], \end{aligned}$$

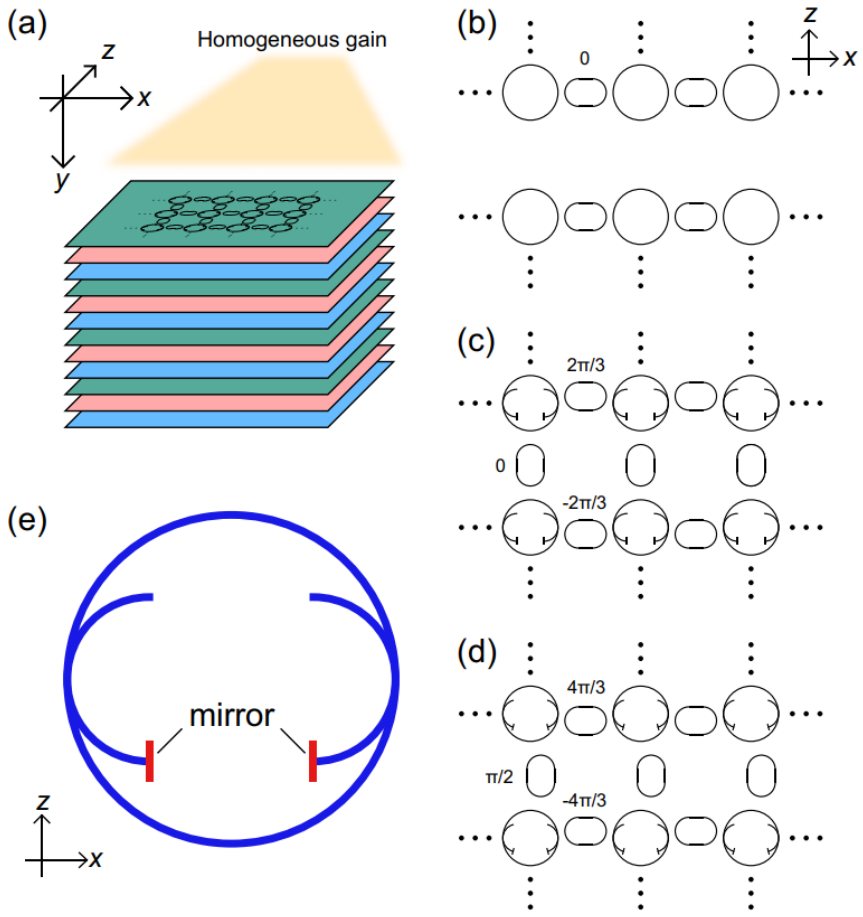

Figure A.7: Proposed experimental setup using ring-resonator arrays. (a) Overview of the proposed system. We accumulate three types of layers (depicted by layers of different colors). (b-d) Ring-resonator array on each layer. The number shows the phase factor of the corresponding linear coupling. In panels (c) and (d), we also introduce waveguides with mirrors in panel (e) into ring resonators. (e) Schematic of the waveguides with mirrors that realize the non-Hermitian coupling. These figures are adapted from K. Sone, Y. Ashida, and T. Sagawa, Exceptional mode topological surface laser. *Phys. Rev. B* **105,** 235426 (2022) [343] Copyright 2022 by the American Physical Society.

(A.20)

where $\hat{c}^{\dagger}_{\mathbf{r},s}$ and $\hat{c}_{\mathbf{r},s}$ are the bosonic creation and annihilation operators of the effective spin s at the site $\mathbf{r}$. $\mathbf{e}_i$ denotes the lattice vector in the $i = x, y, z$ direction. ϕ is the phase parameter, which we set $\phi = 2\pi/3$ (corresponding to the fact that we align three different layers). a_x, a_y, a_z, and β are real parameters that determine the hopping amplitudes.

We numerically confirm the emergence of exceptional surface modes in the Hamiltonian (A.20). Figure A.8(a) shows the surface band structure of the photonic system calculated under the open boundary condition in the x direction and the periodic boundary conditions in the y and z directions. We confirm the existence of exceptional surface modes, i.e., gapless surface modes with exceptional points in their bands. We also check that the imaginary parts of the eigenvalues of exceptional surface modes are larger than those of the bulk modes, which indicates the amplification of the exceptional surface modes.

We also simulate the dynamics of the photonic system and check the amplification of the surface sites. We here conduct the fourth-order Runge-Kutta simulation as in Fig. A.6 with the time step being $dt = 0.001$. We impose the open boundary conditions in all directions. We start from the random initial condition, where the real and imaginary part of the effective wavefunction at each

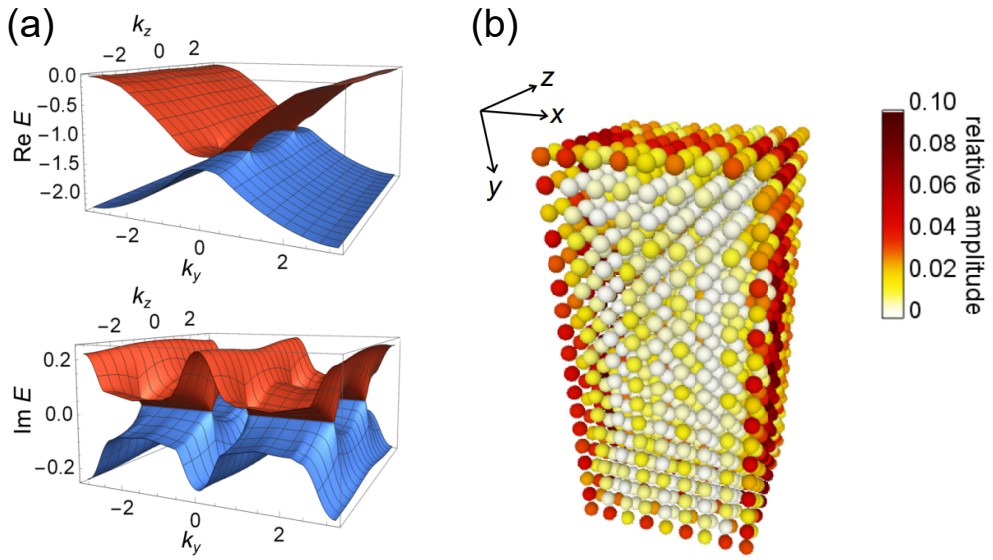

Figure A.8: Numerical demonstration of the lasing surface modes in the proposed optical system. (a) Surface band structure of the effective Hamiltonian of the proposed system (A.20). We confirm the existence of exceptional surface modes with large imaginary parts of eigenvalues. We use the parameters $a_x = a_y = 1$, $a_z = 0.1$, and $\beta = 0.5$. (b) Numerical simulation of the effective Hamiltonian. The color of each site represents the relative amplitude, whose squared sum is unity. We confirm the spontaneous amplification of surface modes. These figures are adapted from K. Sone, Y. Ashida, and T. Sagawa, Exceptional mode topological surface laser. *Phys. Rev. B* **105,** 235426 (2022) [343] Copyright 2022 by the American Physical Society.

site is randomly determined from the uniform distribution ranging $[-0.01, 0.01]$. Figure A.8(b) shows the snapshot of the simulation after the dynamics is relaxed. We confirm the amplification of the boundary sites on the surfaces that are perpendicular to the xy plane. Since the z direction is the direction of the accumulation of the layers of the quantum spin Hall system, we find no exceptional surface modes on the surface parallel to the xy plane. This result indicates that the proposed photonic system can be used as a topological surface laser.

A.2.4 No-go theorem of exceptional surface modes with a single pair of exceptional points

As a starting point of the construction of the topological lasers, we utilize weak topological insulators that have two Dirac cones in their surface band structures. Adding the non-Hermitian spin couplings, one can split those Dirac points into exceptional points and obtain four exceptional points in total. Meanwhile, one may question whether one can realize a topological surface laser starting from a strong topological insulator exhibiting one Dirac cone in its surface band. However, we find that four exceptional points are necessary to realize robust exceptional surface modes under the fully open boundary conditions. Specifically, we analytically show that if we consider exceptional surface modes with a pair of exceptional points, the gapless surface modes disappear under the fully open boundary conditions due to the non-Hermitian skin effect [102–105, 107, 159].

To show the disappearance of exceptional surface modes with only a pair of exceptional points, we consider the winding number that predicts the presence or absence of the non-Hermitian skin effect. To simplify the problem, we assume that exceptional points are located on the k_y axis of the surface bands. Then, we consider two loops on the Brillouin zone L_1 and L_2 in Fig. A.9. The winding numbers on those loops are defined as $w_{1,2} = (1/2\pi i) \int_{L_{1,2}} \partial_{k_x} \log \det H(k_x, k_y) dk_x$. This winding number is unchanged under the deformation of the integral path as long as the path does not cross the exceptional points. Thus, the difference between w_1 and w_2 is equal to the winding

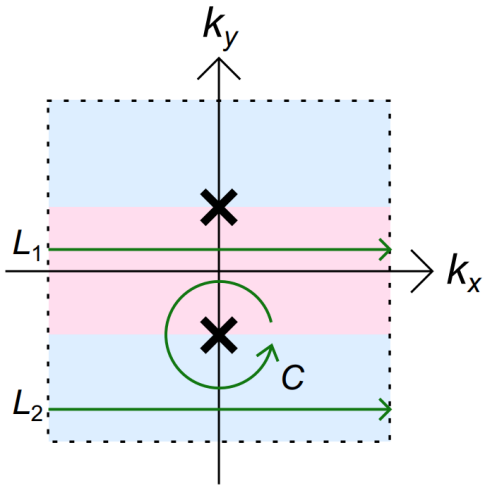

Figure A.9: Integral paths of winding numbers to show the emergence of the non-Hermitian skin effect. Since the winding number calculated on the circle C is nonzero, the winding number from L_1 or L_2 must be nonzero. The blue and red regions represent such a difference in the winding numbers. These figures are adapted from K. Sone, Y. Ashida, and T. Sagawa, Exceptional mode topological surface laser. *Phys. Rev. B* **105,** 235426 (2022) [343] Copyright 2022 by the American Physical Society.

number on the loop around an exceptional point

$$w_1 - w_2 = \frac{1}{2\pi i} \oint_C \partial_{\mathbf{k}} \log \det H(\mathbf{k}) d\mathbf{k} = w_C. \tag{A.21}$$

Meanwhile, the winding number w_C characterizes the nontrivial topology of the exceptional point [101] and thus should be nonzero if the exceptional point is topologically protected. Therefore, w_1 and/or w_2 are nonzero which indicates the emergence of the non-Hermitian skin effect. The non-Hermitian skin effect modifies the spectrum depending on the boundary condition, and the winding number of the spectrum under the open boundary condition must be zero [111]. Therefore, a single pair of exceptional points cannot remain under the fully open boundary conditions, which indicates the disappearance of the robust exceptional surface modes with only two exceptional points in their bands. These arguments imply that topological surface lasers constructed from weak topological insulators are minimal.

A.2.5 Exceptional surface modes protected by exceptional rings

While we construct topological surface lasers protected by exceptional points, we can also realize exceptional surface modes that have exceptional *rings* [344] in their surface bands. Specifically, if we consider the Hamiltonian whose wavenumber-space description is

$$H(\mathbf{k}) = (u + \cos k_x + \cos k_y) I \otimes \sigma_z + \sin k_x \sigma_z \otimes \sigma_x + \sin k_y I \otimes \sigma_y + c \sin k_z \sigma_y \otimes \sigma_x + i\beta \sigma_x \otimes \sigma_x, \tag{A.22}$$

with u, c, and β being real parameters, we can obtain such exceptional surface modes with exceptional rings. This model is also constructed from the weak topological insulator used in our prototypical model (A.18), while the non-Hermitian coupling term $i\beta\sigma_x \otimes \sigma_x$ is different from that in our prototypical model.

To confirm the existence of exceptional surface modes with exceptional rings, we numerically calculate the surface band structure under the open boundary condition in the x direction and the periodic boundary conditions in the y and z directions. Figure A.10 shows the numerical results. We can confirm the gapless surface modes with exceptional rings in their bands. These

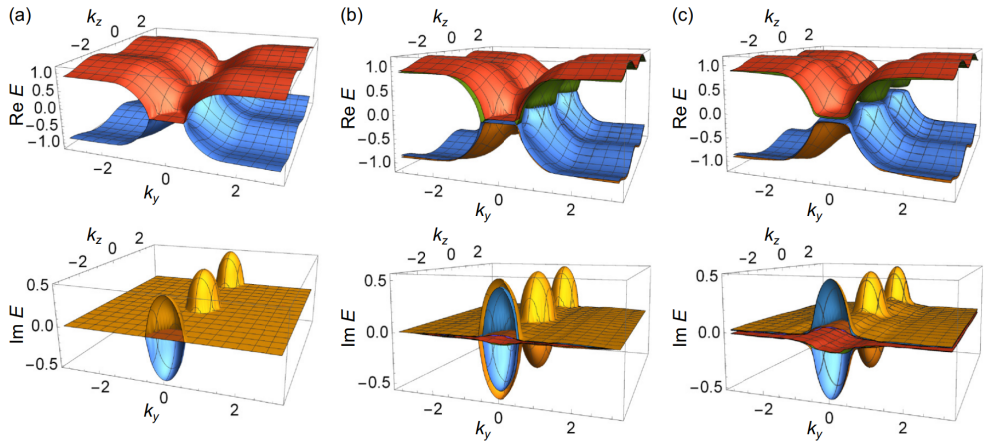

Figure A.10: Surface band structure of exceptional surface modes with exceptional rings. (a) Surface band structure without disorders. We can confirm the existence of gapless modes with exceptional rings in their bands. We use the parameters $u = -1$, $c = 0.7$, and $\beta = 0.5$. (b) Surface band structure under the existence of the on-site random potential and the imaginary random spin coupling. We can confirm the robustness of the exceptional surface modes against such symmetry-preserving disorders. The noise strengths are $w_u = 0.1$ and $W_b = 0.1$. (c) Surface band structures under the existence of the real random spin coupling. Since such a disorder breaks the symmetry, the gapless modes disappear in this case. The noise strengths are $W_u = 0.1$ and $W_a = 0.2$. These figures are adapted from K. Sone, Y. Ashida, and T. Sagawa, Exceptional mode topological surface laser. *Phys. Rev. B* **105,** 235426 (2022) [343] Copyright 2022 by the American Physical Society.

exceptional rings can protect the gapless surface modes from opening gaps under the existence of disorders.

Unlike the exceptional points in the surface bands, exceptional rings can be topologically protected only under the existence of symmetries, such as the PT, CP, chiral symmetries, and pseudo-Hermiticity [151]. Therefore, exceptional surface modes with exceptional rings can robustly exist against disorders only if the disorders preserve those symmetries, which is the case in the exceptional edge modes in two-dimensional systems. To numerically demonstrate the symmetry protection of the exceptional surface modes, we also calculate the surface band structures under the existence of disorders. Specifically, we introduce the random real on-site potential and complex noise into the spin coupling. The former is the real diagonal terms with the random value following a uniform distribution ranging $[-W_u, W_u]$. The latter couples the first and fourth components or the second and third components, and its real (imaginary) parts are determined from a uniform distribution ranging $[-W_a, W_a]$ ($[-W_b, W_b]$). Since the random real on-site potential and imaginary noise in the spin coupling preserves the PT symmetry, the exceptional surface modes remain under the existence of those disorders as shown in Fig. A.10(b). In contrast, the real noise in the spin coupling breaks the PT symmetry, adding such a noise lifts the gap in the exceptional surface modes. These results indicate that exceptional surface modes with exceptional rings are protected by the symmetries.

A.2.6 Short summary and perspectives

We here revealed that the exceptional points can protect topological surface modes in three-dimensional systems and such exceptional surface modes can be utilized as topological lasers. We also proposed a concrete photonic setup to realize the topological laser protected by the nontrivial topology of exceptional points. Unlike the previous proposals of topological lasers [22,23,27,109,137,140], the topological surface laser requires no symmetries nor judicious gains at the edge of the system, which can be of practical advantage to realize in a wide range of systems.

The existence of the exceptional edge modes and exceptional surface modes implies the breakdown of the bulk-boundary correspondence in non-Hermitian systems. Thus, it is desirable to construct the topological classification table reflecting the exceptional boundary modes. From an applicational point of view, exceptional points in surface band structures can induce non-Hermitian phenomena such as interchanging of eigenstates [26] and enhanced sensitivity [163]. Such interplays between exceptional points and topological boundary modes may broaden the applications of topological physics.

Appendix B

Supplementary Information on Chapter 4

B.1 Average of the frequencies in the topological synchronized state

We here confirm that the bulk oscillators in the topological synchronized state have inhomogeneous frequencies even if we take the average of those of the four components at each site. We simulate the dynamics of the first model (4.3) by using the Runge-Kutta method with the time step $t = 0.005$. We consider a 20×20 square lattice and impose the open boundary conditions in both x and y directions. Figure B.1 shows the snapshot of the averaged frequency distribution. We confirm that the bulk oscillators still exhibit time- and space-varying frequencies, which indicate their desynchronization.

B.2 Disappearance of topological synchronized state by damping bulk oscillators

Previous research [345] demonstrated the emergence of edge-localized oscillations. In our model, we can also realize such edge-localized oscillations by damping the bulk oscillations. Specifically, if we consider $\alpha < 0$ in our first model (cf. Eq. (4.3) in the main text), the bulk oscillators exhibit no oscillations, while the edge ones exhibit synchronized oscillations. We numerically confirm the edge-localized oscillations by simulating the dynamics of our first model of topological

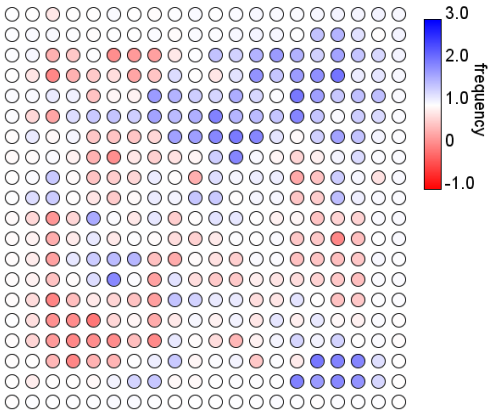

Figure B.1: Averages of the frequencies in the first model (4.3). We plot the average of the frequencies at each site at the time $t = 100$. The averaged frequencies are also inhomogeneous in the bulk. We use the parameters $u = -1$, $b = 0.5$, $\alpha = 0.5$, $\beta = 1$, $\omega_0 = 1$, and $\Delta\omega = 0.2$.

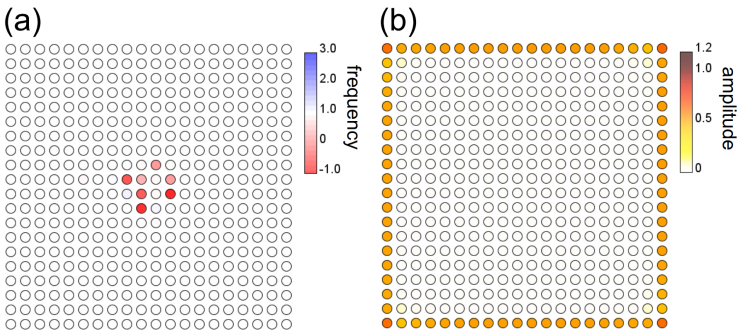

Figure B.2: Synchronization of edge oscillators and damping of bulk oscillators. (a) Frequency distribution of the first component of oscillators of the first model of topological synchronization (4.3) in a damping parameter region. We use the parameters $u = -1$, $b = 0.5$, $\alpha = -0.2$, $\beta = 1$, $\omega_0 = 1$, and $\Delta\omega = 0$. (b) The amplitude distribution of the first model in the damping parameter region. While the edge oscillators have nonzero amplitudes and are synchronized, the bulk ones are damped. These figures are adapted from K. Sone, Y. Ashida, and T. Sagawa, Topological synchronization of coupled nonlinear oscillators. Phys. Rev. Research **4,** 023211 (2022) [327] licensed under a Creative Commons Attribution 4.0 International License (http://creativecommons.org/licenses/by/4.0/).

synchronization. We use the Runge-Kutta method and set the time step as $t = 0.005$. We consider a 20×20 square lattice and impose the open boundary conditions in both x and y directions. Figure B.2 shows the snapshot of the numerical simulation. We confirm that the edge oscillators have nonzero amplitudes while the bulk ones do not oscillate. We can also confirm that the frequencies of the edge oscillators are almost the same, which indicates their synchronization.

We note that the edge-localized synchronized state observed in this numerical calculation is not classified into the topological synchronized state proposed in our study. This is because the bulk oscillators do not exhibit desynchronized oscillations. Since the bulk oscillators in the topological synchronized state can further exhibit chaotic dynamics, the topological synchronized state reveals nontrivial interplays between the band topology and the nonlinear effect.

B.3 Cluster synchronization using topological linear couplings

Previous research [49] also discussed the synchronized state where the edge and bulk oscillators have different frequencies. We here demonstrate a similar cluster synchronization by using linear couplings described by the Hamiltonian of lasing edge modes that is different from those used in the main text. Specifically, we consider the following Hamiltonian,

$$\begin{aligned} H(\mathbf{k}) &= (u + \cos k_x + \cos k_y)\sigma_z \\ &\quad +(\sin k_y + i\gamma \cos k_y)\sigma_y + \sin k_x \sigma_x. \end{aligned} \tag{B.1}$$

Figure B.3 shows the band structure of the edge modes of this Hamiltonian. We confirm the existence of lasing edge modes. Meanwhile, the bulk bands have also large imaginary parts of eigenvalues. This leads to the stability of bulk oscillators and their synchronization.

We numerically simulate the model using the linear couplings described by the Hamiltonian (B.1) as in Fig. 4.1. Figure B.4 shows the snapshots of the frequency distributions. We confirm both the edge and bulk oscillators are synchronized, while the right edge oscillators have different frequencies from the others. Therefore, the cluster synchronization is realized in this model. However, since the bulk oscillators are synchronized and thus are not chaotic, the cluster synchronization in this model is not the topological synchronized state defined in our study.

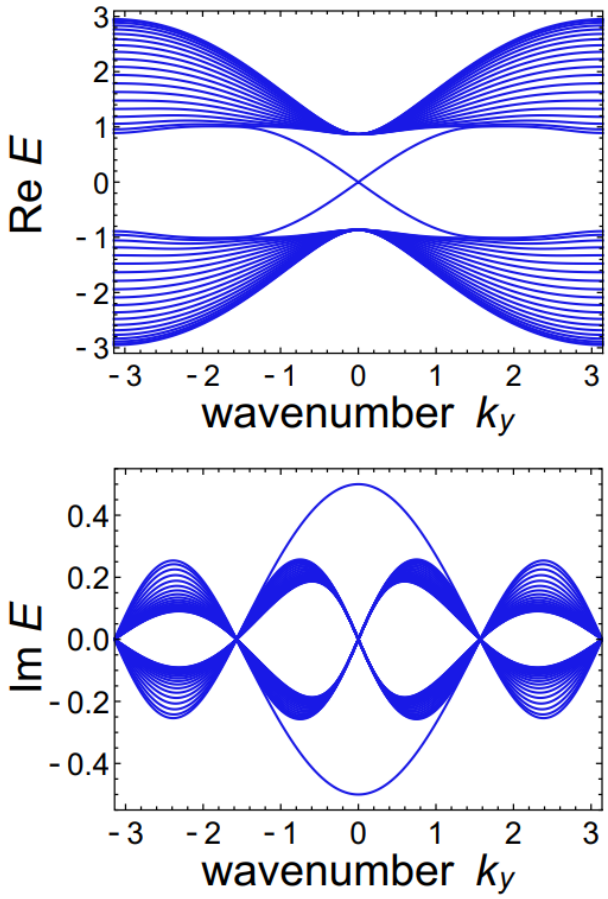

Figure B.3: Band structure of the Hamiltonian used in the model of cluster synchronization (B.1). We confirm the gapless edge modes with larger imaginary parts of eigenvalues than those of bulk modes. We use the parameters $u = -1$ and $\gamma = 0.5$. These figures are adapted from K. Sone, Y. Ashida, and T. Sagawa, Topological synchronization of coupled nonlinear oscillators. Phys. Rev. Research **4,** 023211 (2022) [327] licensed under a Creative Commons Attribution 4.0 International License (http://creativecommons.org/licenses/by/4.0/).

B.4 Nonlinear Chern number of the second model of topological synchronization

We numerically calculate the nonlinear eigenvectors (cf. Sec. 5) of the second model of topological synchronization using the Hamiltonian (4.9) and the associated nonlinear Chern number. Figure B.5 shows the nonlinear Chern number at $u = -1$, $u_i = 0.02$, $a = 2$, $b = 0.5$, $\alpha = \beta = 1$, and different amplitudes w. We confirm that in this parameter region, we always obtain the nonlinear Chern number $C_{\mathrm{NL}} = \pm 1$ (there are two degenerated bands for each). Since the maximum amplitude considered here is larger than that observed in the numerical simulation in Fig, 4.10, it may be possible to expect that the nonzero nonlinear Chern number characterizes the topological synchronized state. However, the time- and space-varying amplitudes break the assumptions that we impose to derive the nonlinear Chern number, and thus the bulk-boundary correspondence in this dissipative system still remains a future problem.

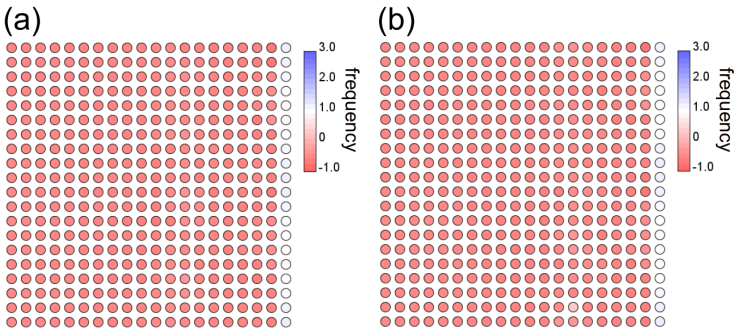

Figure B.4: Cluster synchronization exhibiting a cluster localized to the right edge. We show the snapshots at $t = 1000$ and $t = 2000$ in panels (a) and (b), respectively. We confirm that the oscillators at the right edge have different frequencies from the others. However, both the edge and bulk oscillators are synchronized, this cluster synchronization is not regarded as the topological synchronized state defined in our study. We use the parameters $u = -1$, $\gamma = 0.5$, $\alpha = 0.5$, $\beta = 1$, $\omega_0 = 1$, and $\Delta\omega = 0.2$. These figures are adapted from K. Sone, Y. Ashida, and T. Sagawa, Topological synchronization of coupled nonlinear oscillators. Phys. Rev. Research **4,** 023211 (2022) [327] licensed under a Creative Commons Attribution 4.0 International License (http://creativecommons.org/licenses/by/4.0/).

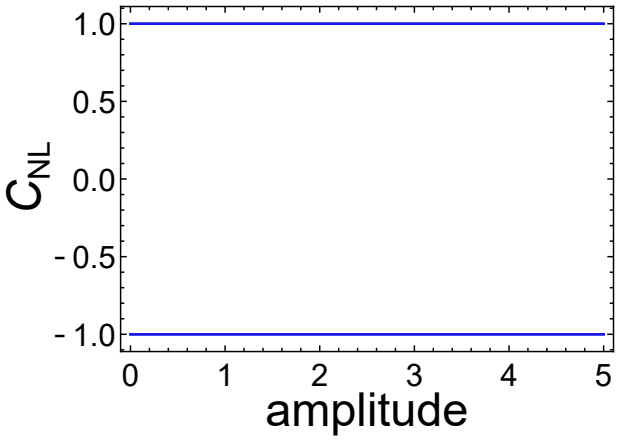

Figure B.5: Nonlinear Chern number of the second model (4.9). We obtain the nonlinear Chern numbers ± 1 from two bands for each. The nonlinear Chern numbers are independent of the amplitude in this parameter regime. We use the parameters $u = -1$, $u_i = 0.02$, $a = 2$, $b = 0.5$, and $\alpha = \beta = 1$.

Appendix C

Supplementary information on Chapter 5 (removed for the future publication in a scientific journal)

This chapter is removed because the results will be published in a scientific journal in five years.

Appendix D

Supplementary information on Chapter 6 (removed for the future publication in a scientific journal)

This chapter is removed because the results will be published in a scientific journal in five years.

Acknowledgement

First, I am very grateful to my supervisor, Prof. Takahiro Sagawa, for the fruitful discussions and dedicated support in my research. His helpful comments have improved the quality of my works and made them attractive papers. I also have learned a lot from him on the methods of research, academic writing, presentations, and career development.

I am also very grateful to my collaborators, Prof. Yuto Ashida, Prof. Motohiko Ezawa, Prof. Zongping Gong, Mr. Taro Sawada, and Dr. Nobuyuki Yoshioka. In particular, Prof. Yuto Ashida has supported my studies since I was an undergraduate student, and provided the first opportunity to study topological physics. Dr. Nobuyuki Yoshioka has also greatly supported my research as the assistant professor in Sagawa group. I thank him for valuable comments on both physics and a reseach life.

I also thank the current and previous members of Sagawa group. They help me to have a good research life in my Ph.D course. I am very grateful to Mrs. Sachiko Seto for supporting me with paperworks.

I am grateful to my thesis committee, Prof. Zongping Gong, Prof. Hosho Katsura, Prof. Eiji Saitoh, and Prof. Haruki Watanabe for their valuable comments. I also thank Prof. Takahiro Morimoto and Prof. Shin-ichi Sasa for helpful discussions on my papers. I am also grateful to Prof. Kyogo Kawaguchi, Dr. Daiki Nishiguchi, and Prof. Kazumasa Takeuchi for valuable comments on my studies including ones that I did in my master course.

Finally, I appreciate the financial support from World-leading Innovative Graduate Study Program for Materials Research, Information, and Technology (MERIT-WINGS) of the University of Tokyo and JSPS KAKENHI Grant Number JP21J20199.

References

[1] M. Z. Hasan and C. L. Kane, Colloquium: Topological insulators. *Rev. Mod. Phys.* **82,** 3045–3067 (2010).

[2] X. L. Qi and S. C. Zhang, Topological insulators and superconductors. *Rev. Mod. Phys.* **83,** 1057–1110 (2011).

[3] Y. Ando, Topological Insulator Materials. *J. Phys. Soc. Jpn.* **82,** 102001 (2013).

[4] K. v. Klitzing, G. Dorda, and M. Pepper, New Method for High-Accuracy Determination of the Fine-Structure Constant Based on Quantized Hall Resistance. *Phys. Rev. Lett.* **45,** 494–497 (1980).

[5] D. J. Thouless, M. Kohmoto, M. P. Nightingale, and M. D. Nijs, Quantized Hall Conductance in a Two-Dimensional Periodic Potential. *Phys. Rev. Lett.* **49,** 405–408 (1982).

[6] L. Fu, C. L. Kane, and E. J. Mele, Topological Insulators in Three Dimensions. *Phys. Rev. Lett.* **98,** 106803 (2007).

[7] C. L. Kane and E. J. Mele, Z_2 Topological Order and the Quantum Spin Hall Effect. *Phys. Rev. Lett.* **95,** 146802 (2005).

[8] C. L. Kane and E. J. Mele, Z_2 Quantum Spin Hall Effect in Graphene. *Phys. Rev. Lett.* **95,** 226801 (2005).

[9] A. B. Khanikaev *et al.*, Photonic topological insulators. *Nat. Mater.* **12,** 233–239 (2013).

[10] L. Lu, J. D. Joannopoulos, and M. Soljačić, Topological photonics. *Nat. Photonics* **8,** 821–829 (2014).

[11] T. Ozawa *et al.*, Topological photonics. *Rev. Mod. Phys.* **91,** 015006 (2019).

[12] Z. Yang *et al.*, Topological Acoustics. *Phys. Rev. Lett.* **114,** 114301 (2015).

[13] P. Delplace, J. B. Marston, and A. Venaille, Topological origin of equatorial waves. *Science* **358,** 1075–1077 (2017).

[14] G. Jotzu *et al.*, Experimental realization of the topological Haldane model with ultracold fermions. *Nature* **515,** 237–240 (2014).

[15] N. R. Cooper, J. Dalibard, and I. B. Spielman, Topological bands for ultracold atoms. *Rev. Mod. Phys.* **91,** 015005 (2019).

[16] J. Ningyuan, C. Owens, A. Sommer, D. Schuster, and J. Simon, Time- and Site-Resolved Dynamics in a Topological Circuit. *Phys. Rev. X* **5,** 021031 (2015).

[17] V. V. Albert, L. I. Glazman, and L. Jiang, Topological Properties of Linear Circuit Lattices. *Phys. Rev. Lett.* **114,** 173902 (2015).

[18] C. L. Kane and T. C. Lubensky, Topological boundary modes in isostatic lattices. *Nat. Phys.* **10,** 39–45 (2014).

[19] L. M. Nash *et al.*, Topological mechanics of gyroscopic metamaterials. *Proc. Natl. Acad. Sci. USA* **112,** 14495–14500 (2015).

[20] S. D. Huber, Topological mechanics. *Nat. Phys.* **12,** 621–623 (2016).

[21] Y. Ashida, Z. Gong, and M. Ueda, Non-Hermitian Physics. *Adv. Phys.* **69,** 249–435 (2021).

[22] G. Harari *et al.*, Topological insulator laser: Theory. *Science* **359,** 1230 (2018).

[23] M. A. Bandres *et al.*, Topological insulator laser: Experiments. *Science* **359,** 1231 (2018).

[24] Z. Gong *et al.*, Topological Phases of Non-Hermitian Systems. *Phys. Rev. X* **8,** 031079 (2018).

[25] T. Kato, Perturbation Theory for Linear Operators, Springer, New York, 1966.

[26] C. Dembowski, *et al.*, Experimental Observation of the Topological Structure of Exceptional Points. *Phys. Rev. Lett.* **86,** 787–790 (2001).

[27] K. Sone, Y. Ashida, and T. Sagawa, Exceptional non-Hermitian topological edge mode and its application to active matter. *Nat. Commun.* **11,** 5745 (2020).

[28] S. H. Strogatz, Nonlinear Dynamics and Chaos - With Applications to Physics, Biology, Chemistry and Engineering (Addison-Wesley, Reading, MA, 1994).

[29] J. A. Acebrón, L. L. Bonilla, V. C. J. Pérez, Ritort, F., & Spigler, R. The Kuramoto model: A simple paradigm for synchronization phenomena. *Rev. Mod. Phys.* **77,** 137–185 (2005).

[30] J. Buck, Synchronous rhythmic flashing of fireflies. II. *Quart. Rev. Biol.* **63,** 265–289 (1988).

[31] C. H. Luo, and Y. Rudy, A model of the ventricular cardiac action potential. Depolarization, repolarization, and their interaction. *Circ. Res.* **68,** 1501–1526 (1991).

[32] J. Fell and N. Axmacher, The role of phase synchronization in memory processes. *Nat. Rev. Neurosci.* **12,** 105–118 (2011).

[33] C. Dibner, U. Schibler, and U. Albrecht, The Mammalian Circadian Timing System: Organization and Coordination of Central and Peripheral Clocks. *Annu. Rev. Physiol.* **72,** 517–549 (2010).

[34] K. Wiesenfeld, P. Colet, and S. H. Strogatz, Synchronization Transitions in a Disordered Josephson Series Array. *Phys. Rev. Lett.* **76,** 404–407 (1996).

[35] J. Pantaleone, Synchronization of metronomes. *Am. J. Phys.* **70,** 992-1000 (2002).

[36] F. Blaabjerg, R. Teodorescu, M. Liserre, and A. V. Timbus, Overview of Control and Grid Synchronization for Distributed Power Generation Systems. *IEEE Trans. Ind. Electron.* **53,** 1398–1409 (2006).

[37] R. W. Boyd, Nonlinear Optics, Academic, Cambridge, 2003.

[38] D. Smirnova, D. Leykam, Y. Chong, and Y. Kivshar, Nonlinear topological photonics. *Appl. Phys. Rev.* **7,** 021306 (2020).

[39] Y. Ota *et al.*, Active topological photonics. *Nanophotonics* **9,** 547–567 (2020).

[40] E. P. Gross, Structure of a quantized vortex in boson systems. *Il Nuovo Cimento* **20,** 454 - 477 (1961).

[41] L. P. Pitaevskii, Vortex lines in an imperfect Bose gas. *Sov. Phys. JETP* **13,** 451–454 (1961).

[42] R. May, Simple mathematical models with very complicated dynamics. *Nature* **261,** 459--467 (1976).

[43] Y. Lumer, Y. Plotnik, M. C. Rechtsman,and M. Segev, Self-Localized States in Photonic Topological Insulators. *Phys. Rev. Lett.* **111,** 243905 (2013).

[44] D. Leykam and Y. D. Chong, Edge Solitons in Nonlinear-Photonic Topological Insulators. *Phys. Rev. Lett.* **117,** 143901 (2016).

[45] Z. Zhang *et al.*, Observation of edge solitons in photonic graphene. *Nat. Commun.* **11,** 1902 (2020).

[46] Y. Hadad, A. B. Khanikaev, and A. Alù, Self-induced topological transitions and edge states supported by nonlinear staggered potentials. *Phys. Rev. B* **93,** 155112 (2016).

[47] T. Tuloup, R. W. Bomantara, C. H. Lee, and J. Gong, Nonlinearity induced topological physics in momentum space and real space. *Phys. Rev. B* **102,** 115411 (2020).

[48] D. Zhou, D. Z. Rocklin, M. Leamy, and Y. Yao, Topological invariant and anomalous edge modes of strongly nonlinear systems. *Nat. Commun.* **13,** 3379 (2022).

[49] T. Kotwal *et al.*, Active topolectrical circuits. *Proc. Natl. Acad. Sci. U.S.A.* **118,** e2106411118 (2021).

[50] R. B. Laughlin, Quantized Hall conductivity in two dimensions. *Phys. Rev. B* **23,** 5632(R) (1981).

[51] Y. Hatsugai, Edge states in the integer quantum Hall effect and the Riemann surface of the Bloch function. *Phys. Rev. B* **48,** 11851 (1993).

[52] Y. Hatsugai, Chern number and edge states in the integer quantum Hall effect. *Phys. Rev. Lett.* **71,** 3697 (1993).

[53] F. D. M. Haldane, Model for a Quantum Hall Effect without Landau Levels: Condensed-Matter Realization of the "Parity Anomaly". *Phys. Rev. Lett.* **61,** 2015–2018 (1988).

[54] C.-Z. Chang *et al.*, Experimental Observation of the Quantum Anomalous Hall Effect in a Magnetic Topological Insulator. *Science* **340,** 167–170 (2013).

[55] Q. Niu, D. J. Thouless, and Y.-S. Wu, Quantized Hall conductance as a topological invariant. *Phys. Rev. B* **31,** 3372–3377 (1985).

[56] J. Bellissard, A. van Elst, and H. Schulz-Baldes, The Non-Commutative Geometry of the Quantum Hall Effect. *J. Math. Phys.* **35,** 5373 (1994).

[57] M. B. Hastings and T. A. Loring, Almost Commuting Matrices, Localized Wannier Functions, and the Quantum Hall Effect. *J. Math. Phys.* **51,** 015214 (2010).

[58] H. Katsura and T. Koma, The noncommutative index theorem and the periodic table for disordered topological insulators and superconductors. *J. Math. Phys.* **59,** 031903 (2018).

[59] B. A. Bernevig and S. C. Zhang, Quantum Spin Hall Effect. *Phys. Rev. Lett.* **96,** 106802 (2006).

[60] B. A. Bernevig, T. L. Hughes, and S. C. Zhang, Quantum Spin Hall Effect and Topological Phase Transition in HgTe Quantum Wells. *Science* **314,** 1757–1761 (2006).

[61] A. Kitaev, Periodic table for topological insulators and superconductors. *AIP Conference Proceedings* **1134,** 22-30 (2009).

[62] S. Ryu, A. P. Schnyde, A. Furusaki, and A. W. W. Ludwig, Topological insulators and superconductors: tenfold way and dimensional hierarchy. *New J. Phys.* **12,** 065010 (2010).

[63] A. Altland and M. R. Zirnbauer, Nonstandard Symmetry Classes in Mesoscopic Normal-Superconducting Hybrid Structures. *Phys. Rev. B* **55,** 1142 (1997).

[64] C. Nayak, S. H. Simon, A. Stern, M. Freedman, and S. D. Sarma, Non-Abelian anyons and topological quantum computation. *Rev. Mod. Phys.* **80,** 1083–1159 (2008).

[65] J. Alicea, Y. Oreg, G. Refael, F. von Oppen, and M. P. A. Fisher, Non-Abelian statistics and topological quantum information processing in 1D wire networks. *Nat. Phys.* **7,** 412–417 (2008).

[66] H. Song, S.-J. Huang, L. Fu, and M. Hermele, Topological phases protected by point group symmetry. *Phys. Rev. X* **7,** 011020 (2017).

[67] J. Kruthoff, J. de Boer, J. van Wezel, C. L. Kane, and R.-J. Slager, Topological classification of crystalline insulators through band structure combinatorics. *Phys. Rev. X* **7,** 041069 (2017).

[68] H. C. Po, A. Vishwanath, and H. Watanabe, Symmetry-based indicators of band topology in the 230 space groups. *Nat. Commun.* **8,** 50 (2017).

[69] Z. Ringel, Y. E. Kraus, and A. Stern, Strong side of weak topological insulators. *Phys. Rev. B* **86,** 045102 (2012).

[70] X. Wan, A. M. Turner, A. Vishwanath, and S. Y. Savrasov, Topological semimetal and Fermi-arc surface states in the electronic structure of pyrochlore iridates. *Phys. Rev. B* **83,** 205101 (2011).

[71] N. P. Armitage, E. J. Mele, and A. Vishwanath, Weyl and Dirac semimetals in three-dimensional solids. *Rev. Mod. Phys.* **90,** 015001 (2018).

[72] S. Matsuura, P. Y. Chang, A. P. Schnyder, and S. Ryu, Protected boundary states in gapless topological phases. *New J. Phys.* **15,** 065001 (2013).

[73] X.-L. Qi, T. L. Hughes, and S.-C. Zhang, Topological field theory of time-reversal invariant insulators. *Phys. Rev. B* **78,** 195424 (2008).

[74] V. Gurarie, Single-particle Green' s functions and interacting topological insulators. *Phys. Rev. B* **83,** 085426 (2011).

[75] A. M. Essin and V. Gurarie, Bulk-boundary correspondence of topological insulators from their respective Green's functions. *Phys. Rev. B* **84,** 125132 (2011).

[76] L. Fidkowski and A. Kitaev, Effects of interactions on the topological classification of free fermion systems. *Phys. Rev. B* **81,** 134509 (2010).

[77] L. Fidkowski and A. Kitaev, Topological phases of fermions in one dimension. *Phys. Rev. B* **83,** 075103 (2011).

[78] F. D. M. Haldane, Continuum dynamics of the 1-D Heisenberg antiferromagnet: Identification with the O(3) nonlinear sigma model. *Phys. Lett. A* **93,** 464–468 (1983).

[79] X. Chen, Z.-C. Gu, Z.-X. Liu, and X.-G. Wen, Symmetry-Protected Topological Orders in Interacting Bosonic Systems. *Science* **338,** 1604–1606 (2012).

[80] X. Chen, Z.-C. Gu, Z.-X. Liu, and X.-G. Wen, Symmetry protected topological orders and the group cohomology of their symmetry group. *Phys. Rev. B* **87,** 155114 (2013).

[81] A. Vishwanath and T. Senthil, Physics of Three-Dimensional Bosonic Topological Insulators: Surface-Deconfined Criticality and Quantized Magnetoelectric Effect. *Phys. Rev. X* **3,** 011016 (2013).

[82] A. Kapustin, Symmetry Protected Topological Phases, Anomalies, and Cobordisms: Beyond Group Cohomology. arXiv:1403.1467 (2014).

[83] A. Kapustin, Bosonic Topological Insulators and Paramagnets: a view from cobordisms. arXiv:1404.6659 (2014).

[84] A. Kapustin, R. Thorngren, A. Turzillo, and Z. Wang, Fermionic symmetry protected topological phases and cobordisms. *J. High Energy Phys.* **2015,** 1–21 (2015).

[85] T. O. Strandberg, C. M. Canali, and A. H. MacDonald, Calculation of Chern number spin Hamiltonians for magnetic nano-clusters by DFT methods. *Phys. Rev. B* **77,** 174416 (2008).

[86] S. Dongbin *et al.*, Unraveling materials Berry curvature and Chern numbers from real-time evolution of Bloch states. *Proc. Natl. Acad. Sci. USA* **116,** 4135–4140 (2019).

[87] W. Magnus, On the exponential solution of differential equations for a linear operator. *Communications on pure and applied mathematics* **7,** 649 (1954).

[88] T. Oka and H. Aoki, Photovoltaic Hall effect in graphene. *Phys. Rev. B* **79,** 081406(R) (2009).

[89] T. Kitagawa, E. Berg, M. Rudner, and E. Demler, Topological characterization of periodically driven quantum systems. *Phys. Rev. B* **82,** 235114 (2010).

[90] M. S. Rudner, N. H. Lindner, E. Berg, and M. Levin, Anomalous Edge States and the Bulk-Edge Correspondence for Periodically Driven Two-Dimensional Systems. *Phys. Rev. X* **3,** 031005 (2013).

[91] J. K. Asbóth, O. László, and P. András, A short course on topological insulators. *Lecture notes in physics* **919,** 166 (2016)

[92] F. D. M. Haldane and S. Raghu, Possible Realization of Directional Optical Waveguides in Photonic Crystals with Broken Time-Reversal Symmetry. *Phys. Rev. Lett.* **100,** 013904 (2008).

[93] W. P. Su, J. R. Schrieffer, and A. J. Heeger, Soliton excitations in polyacetylene. *Phys. Rev. B* **22,** 2099 (1980).

[94] X. L. Qi, Y. S. Wu, and S. C. Zhang, Topological quantization of the spin Hall effect in two-dimensional paramagnetic semiconductors. *Phys. Rev. B* **74,** 085308 (2006).

[95] M. J. Rice and E. J. Mele, Elementary Excitations of a Linearly Conjugated Diatomic Polymer. *Phys. Rev. Lett.* **49,** 1455 (1982).

[96] R. Jackiw and C. Rebbi, Solitons with fermion number 1/2. *Phys. Rev. D* **13,** 3398 (1976).

[97] Y. C. Hu and T. L. Hughes, Absence of topological insulator phases in non-Hermitian PT-symmetric Hamiltonians. *Phys. Rev. B* **84,** 153101 (2011).

[98] K. Esaki, M. Sato, K. Hasebe, and M. Kohmoto, Edge states and topological phases in non-Hermitian systems. *Phys. Rev. B* **84,** 205128 (2011).

[99] T. E. Lee, Anomalous Edge State in a Non-Hermitian Lattice. *Phys. Rev. Lett.* **116,** 133903 (2016).

[100] D. Leykam, K. Y. Bliokh, C. Huang, Y. D. Chong, and F. Nori, Edge Modes, Degeneracies, and Topological Numbers in Non-Hermitian Systems. *Phys. Rev. Lett.* **118,** 040401 (2017).

[101] H. Shen, B. Zhen, and L. Fu, Topological Band Theory for Non-Hermitian Hamiltonians. *Phys. Rev. Lett.* **120,** 146402 (2018).

[102] F. K. Kunst, E. Edvardsson, J. C. Budich, and E. J. Bergholtz, Biorthogonal Bulk-Boundary Correspondence in Non-Hermitian Systems. *Phys. Rev. Lett.* **121,** 026808 (2018).

[103] Y. Xiong, Why does bulk boundary correspondence fail in some non-hermitian topological models. *J. Phys. Commun.* **2,** 035043 (2018).

[104] S. Yao and Z. Wang, Edge States and Topological Invariants of Non-Hermitian Systems. *Phys. Rev. Lett.* **121,** 086803 (2018).

[105] C. H. Lee and R. Thomale, Anatomy of skin modes and topology in non-Hermitian systems. *Phys. Rev. B* **99,** 201103 (2019).

[106] S. Longhi, Probing non-Hermitian skin effect and non-Bloch phase transitions. *Phys. Rev. Research* **1,** 023013 (2019).

[107] K. Yokomizo and S. Murakami Non-Bloch Band Theory of Non-Hermitian Systems. *Phys. Rev. Lett.* **123,** 066404 (2019).

[108] H. Zhou and J. Y. Lee Periodic table for topological bands with non-Hermitian symmetries. *Phys. Rev. B* **99,** 235112 (2019).

[109] K. Kawabata, K. Shiozaki, M. Ueda, and M. Sato, Symmetry and Topology in Non-Hermitian Physics. *Phys. Rev. X* **9,** 041015 (2019).

[110] D. S. Borgnia, A. J. Kruchkov, and R. J. Slager, Non-Hermitian Boundary Modes and Topology. *Phys. Rev. Lett.* **124,** 056802 (2020).

[111] N. Okuma, K. Kawabata, K. Shiozaki, and M. Sato, Topological Origin of Non-Hermitian Skin Effects. *Phys. Rev. Lett.* **124,** 086801 (2020).

[112] K. Zhang, Z. Yang, and C. Fang, Correspondence between Winding Numbers and Skin Modes in Non-Hermitian Systems. *Phys. Rev. Lett.* **125,** 126402 (2020).

[113] A. Ruschhaupt, F. Delgado, and J. G. Muga, Physical realization of PT-symmetric potential scattering in a planar slab waveguide. *J. Phys. A* **38,** L171–L176 (2005).

[114] R. El-Ganainy, K. G. Makris, D. N. Christodoulides, & Z. H. Musslimani, Theory of coupled optical PT-symmetric structures. *Opt. Lett.* **32,** 2632–2634 (2007)

[115] C. E. Rüter *et al.*, Observation of parity-time symmetry in optics. *Nat. Phys.* **6,** 192–195 (2010).

[116] A. Regensburger *et al.*, Parity-time synthetic photonic lattices. *Nat. Phys.* **6,** 167–171 (2012).

[117] M. Ezawa, Non-Hermitian boundary and interface states in nonreciprocal higher-order topological metals and electrical circuits. *Phys. Rev. B* **99,** 121411 (2019).

[118] T. Helbig *et al.*, Generalized bulk-boundary correspondence in non-Hermitian topolectrical circuits. *Nat. Phys.* **16,** 747–750 (2020).

[119] T. Hofmann, T. Helbig, C. H. Lee, M. Greiter, and R. Thomale, Chiral Voltage Propagation and Calibration in a Topolectrical Chern Circuit. *Phys. Rev. Lett.* **122,** 247702 (2019).

[120] H. Xu, D. Mason, L. Jiang, and J. G. E. Harris, Topological energy transfer in an optomechanical system with exceptional points. *Nature* **537,** 80–83 (2016).

[121] H. Jing, Ş. K. Özdemir, H. Lü, and F. Nori, High-order exceptional points in optomechanics. *Sci. Rep.* **7,** 3386 (2017).

[122] W. Zhu *et al.*, Simultaneous Observation of a Topological Edge State and Exceptional Point in an Open and Non-Hermitian Acoustic System. *Phys. Rev. Lett.* **121,** 124501 (2018).

[123] Z. Zhang, M. R. López, Y. Cheng, X. Liu, and J. Christensen, Non-Hermitian Sonic Second-Order Topological Insulator. *Phys. Rev. Lett.* **122,** 195501 (2019).

[124] A. Murugan and S. Vaikuntanathan, Topologically protected modes in non-equilibrium stochastic systems. *Nat. Commun.* **8,** 13881 (2017).

[125] K. Dasbiswas, K. K. Mandadapu, and S. Vaikuntanathan, Topological localization in out-of-equilibrium dissipative systems. *Proc. Natl. Acad. Sci. USA* **115,** 9031–9040 (2018).

[126] T. Sawada, K. Sone, R. Hamazaki, Y. Ashida, and T. Sagawa, Role of Topology in Relaxation of One-Dimensional Stochastic Processes. *Phys. Rev. Lett.* **132,** 046602 (2024).

[127] Y. Ashida, S. Furukawa, and M. Ueda, Parity-time-symmetric quantum critical phenomena. *Nat. Commun.* **8,** 15791 (2017).

[128] J. Li *et al.*, Observation of parity-time symmetry breaking transitions in a dissipative Floquet system of ultracold atoms. *Nat. Commun.* **10,** 855 (2019).

[129] M. S. Rudner and L. S. Levitov, Topological Transition in a Non-Hermitian Quantum Walk. *Phys. Rev. Lett.* **102,** 065703 (2009).

[130] L. Xiao *et al.*, Observation of topological edge states in parity-time-symmetric quantum walks. *Nat. Phys.* **13,** 1117–1123 (2017).

[131] L. Xiao *et al.*, Non-Hermitian bulk-boundary correspondence in quantum dynamics. *Nat. Phys.* **16,** 761–766 (2020).

[132] K. Mochizuki, D. Kim, N. Kawakami, and H. Obuse, Bulk-edge correspondence in nonunitary Floquet systems with chiral symmetry. *Phys. Rev. A* **102,** 062202 (2020).

[133] H. Feshbach, Unified theory of nuclear reactions. *Ann. Phys.* **5,** 357–390 (1958).

[134] V. Gorini, A. Kossakowski, and E. C. G. Sudarshan, Completely positive dynamical semigroups of N-level systems, *J. Math. Phys.* **17,** 821 (1976).

[135] G. Lindblad, On the generators of quantum dynamical semigroups, *Commun. Math. Phys.* **48,** 119 (1976).

[136] P. St-Jean *et al.*, Lasing in topological edge states of a one-dimensional lattice. *Nat. Photonics* **11,** 651–656 (2017).

[137] B. Bahari *et al.*, Nonreciprocal lasing in topological cavities of arbitrary geometries. *Science* **358,** 636–640 (2017).

[138] M. Parto *et al.*, Edge-Mode Lasing in 1D Topological Active Arrays. *Phys. Rev. Lett.* **120,** 113901 (2018).

[139] Y. V. Kartashov and D. V. Skryabin, Two-Dimensional Topological Polariton Laser. *Phys. Rev. Lett.* **122,** 083902 (2019).

[140] A. Y. Song *et al.*, $\mathcal{PT}$-Symmetric Topological Edge-Gain Effect. *Phys. Rev. Lett.* **125,** 033603 (2020).

[141] N. Hatano and D. R. Nelson, Localization Transitions in Non-Hermitian Quantum Mechanics. *Phys. Rev. Lett.* **77,** 570–573 (1996).

[142] K. Kawabata, N. Okuma, and M. Sato, Non-Bloch band theory of non-Hermitian Hamiltonians in the symplectic class. *Phys. Rev. B* **101,** 195147 (2020).

[143] T. Hofmann *et al.*, Reciprocal skin effect and its realization in a topolectrical circuit. *Phys. Rev. Research* **2,** 023265 (2020).

[144] M. M. Denner *et al.*, Exceptional Topological Insulators. *Nat. Commun.* **12,** 5681 (2021).

[145] K. Yokomizo and S. Murakami, Non-Bloch bands in two-dimensional non-Hermitian systems. *Phys. Rev. B* **107,** 195112 (2023).

[146] H.-Y. Wang, F. Song, and Z. Wang, Amoeba formulation of the non-Hermitian skin effect in higher dimensions. arXiv:2212.11743 (2022).

[147] H. Hu, Non-Hermitian band theory in all dimensions: uniform spectra and skin effect. arXiv:2306.12022 (2023).

[148] D. Bernard and A. LeClair, A Classification of Non-Hermitian Random Matrices. in *Statistical Field Theories* (eds. A. Cappelli and G. Mussardo) 207-214 (Springer, Dordrecht, 2002).

[149] D. Bernard and A. LeClair, A classification of 2D random Dirac fermions. *J. Phys. A: Math. Gen.* **35**, 2555-2567 (2002).

[150] R. Okugawa, R. Takahashi, and K. Yokomizo, Non-Hermitian band topology with generalized inversion symmetry. *Phys. Rev. B* **103,** 205205 (2021).

[151] K. Kawabata, T. Bessho, and M. Sato, Classification of Exceptional Points and Non-Hermitian Topological Semimetals. *Phys. Rev. Lett.* **123,** 066405 (2019).

[152] C. M. Bender and S. Boettcher, Real Spectra in Non-Hermitian Hamiltonians Having PT Symmetry. *Phys. Rev. Lett.* **80,** 5243–5246 (1998).

[153] A. Mostafazadeh Pseudo-Hermiticity versus PT symmetry: The necessary condition for the reality of the spectrum of a non-Hermitian Hamiltonian. *J. Math. Phys.* **43,** 205–214 (2002).

[154] R. El-Ganainy *et al.*, Non-Hermitian physics and PT symmetry. *Nat. Phys.* **14,** 11–19 (2018).

[155] R. Okugawa and T. Yokoyama, Topological exceptional surfaces in non-Hermitian systems with parity-time and parity-particle-hole symmetries. *Phys. Rev. B* **99,** 041202 (2019).

[156] J. C. Budich, J. Carlström, F. K. Kunst, and E. J. Bergholtz, Symmetry-protected nodal phases in non-Hermitian systems. *Phys. Rev. B* **99,** 041406 (2019).

[157] E. Persson, I. Rotter, H.-J. Stöckmann, and M. Barth, Observation of Resonance Trapping in an Open Microwave Cavity. *Phys. Rev. Lett.* **85,** 2478–2481 (2000).

[158] K. Yokomizo and S. Murakami, Topological semimetal phase with exceptional points in one-dimensional non-Hermitian systems. *Phys. Rev. Research* **2,** 043045 (2020).

[159] S. Longhi, Probing non-Hermitian skin effect and non-Bloch phase transitions. *Phys. Rev. Research* **1,** 023013 (2019).

[160] L. Xiao *et al.*, Observation of Non-Bloch Parity-Time Symmetry and Exceptional Points. *Phys. Rev. Lett.* **126,** 230402 (2021).

[161] S. Longhi $\mathcal{PT}$-symmetric laser absorber. *Phys. Rev. A* **82,** 031801 (2010).

[162] Z. Lin *et al.*, Unidirectional Invisibility Induced by $\mathcal{PT}$-Symmetric Periodic Structures. *Phys. Rev. Lett.* **106,** 213901 (2011).

[163] Z. Liu *et al.*, Metrology with $\mathcal{PT}$-Symmetric Cavities: Enhanced Sensitivity near the $\mathcal{PT}$-Phase Transition. *Phys. Rev. Lett.* **117,** 110802 (2016).

[164] M. Hafezi, E. A. Demler, M. D. Lukin, and J. M. Taylor, Robust optical delay lines with topological protection, *Nat. Phys.* **7,** 907 (2011).

[165] M. Hafezi, S. Mittal, J. Fan, A. Migdall, and J. M. Taylor, Imaging topological edge states in silicon photonics, *Nat. Photonics* **7,** 1001 (2013).

[166] S. Fan, W. Suh, and J. D. Joannopoulos, Temporal coupled mode theory for the Fano resonance in optical resonators, *J. Opt. Soc. Am. A* **20,** 569 (2003).

[167] H. A. Haus and W. Huang, Coupled-mode theory, *Proc. IEEE* **79,** 1505 (1991)

[168] M. C. Rechtsman *et al.*, Photonic Floquet topological insulators. *Nature* **496,** 196–200 (2013).

[169] Z. Wang, Y. Chong, J. D. Joannopoulos, and M. Soljačić Observation of unidirectional backscattering-immune topological electromagnetic states. *Nature* **461,** 772 - 775 (2009).

[170] L. Lu *et al.*, Experimental observation of Weyl points. *Science* **349,** 622–624 (2013).

[171] A. Slobozhanyuk, *et al.*, Three-dimensional all-dielectric photonic topological insulator, *Nat. Photonics* **11,** 130 (2017).

[172] L. Lu, H. Gao, and Z. Wang, Topological one-way fiber of second Chern number, *Nat. Commun.* **9,** 5384 (2018).

[173] Y. Yang *et al.*, Realization of a three dimensional photonic topological insulator, *Nature* **565,** 622 (2019).

[174] X. Zhu *et al.*, Photonic non-Hermitian skin effect and non-Bloch bulk-boundary correspondence. *Phys. Rev. Research* **2,** 013280 (2020).

[175] Y. G. N. Liu *et al.*, Complex skin modes in non-Hermitian coupled laser arrays. *Light Sci. Appl.* **2,** 013280 (2022).

[176] C. He *et al.*, Acoustic topological insulator and robust one-way sound transport. *Nat. Phys.* **12,** 1124–1129 (2016).

[177] M. Xiao, W. J. Chen, W. Y. He, and C. T. Chan, Synthetic gauge flux and Weyl points in acoustic systems. *Nat. Phys.* **11,** 920–924 (2015).

[178] F. Li, X. Huang, J. Lu, J. Ma, and Z. Liu, Weyl points and Fermi arcs in a chiral phononic crystal. *Nat. Phys.* **14,** 30–34 (2018).

[179] J. C. Maxwell, On the calculaton of the equilibrium stiffness of frames. *Phil. Mag.* **27,** 294–299 (1865).

[180] C. R. Calladine, Buckminster Fuller's 'tensegrity' structures and clerk Maxwell's rules for the construction of stiff frames. *Int. J. Solids Struct.* **14,** 161–172 (1978).

[181] C. Scheibner *et al.*, Odd elasticity. *Nat. Phys.* **16,** 475–480 (2020).

[182] C. Scheibner, W. T. M. Irvine, and V. Vitelli, Non-Hermitian Band Topology and Skin Modes in Active Elastic Media. *Phys. Rev. Lett.* **125,** 118001 (2020).

[183] C. H. Lee *et al.*, Topolectrical Circuits. *Commun. Phys.* **1,** 39 (2018).

[184] S. Imhof *et al.*, Topolectrical-circuit realization of topological corner modes. *Nat. Phys.* **14,** 925–929 (2018).

[185] L. Li, C. H. Lee, and J. Gong, Topological Switch for Non-Hermitian Skin Effect in Cold-Atom Systems with Loss. *Phys. Rev. Lett.* **124,** 250402 (2020).

[186] Q. Liang *et al.*, Dynamic Signatures of Non-Hermitian Skin Effect and Topology in Ultracold Atoms. *Phys. Rev. Lett.* **129,** 070401 (2022).

[187] Y. Takasu *et al.*, PT-symmetric non-Hermitian quantum many-body system using ultracold atoms in an optical lattice with controlled dissipation. *Prog. Theor. Exp. Phys.* **2020,** 12A110 (2020).

[188] S. Shankar, A. Souslov, M. J. Bowick, M. C. Marchetti, and V. Vitelli, Topological active matter. *Nat. Rev. Phys..* **4,** 380–398 (2022).

[189] T. Vicsek and A. Zafeiris, Collective motion. *Phys. Rep.* **517,** 71–140 (2012).

[190] A. Sokolov, I. S. Aranson, J. O. Kessler, and R. E. Goldstein, Concentration Dependence of the Collective Dynamics of Swimming Bacteria. *Phys. Rev. Lett.* **98,** 158102 (2007).

[191] H. H. Wensink *et al.*, Meso-scale turbulence in living fluids. *Proc. Natl. Acad. Sci. USA* **109,** 14308–14313 (2012).

[192] D. Nishiguchi, I. S. Aranson, A. Snezhko, and A. Sokolov, Engineering bacterial vortex lattice via direct laser lithography. *Nat. Commun.* **9,** 4486 (2018).

[193] J. Brugués and D. Needleman, Physical basis of spindle self-organization. *Proc. Natl. Acad. Sci. USA* **111,** 18496–18500 (2014).

[194] T. B. Saw *et al.*, Topological defects in epithelia govern cell death and extrusion. *Nature* **544,** 212–216 (2017).

[195] K. Kawaguchi, R. Kageyama, and M. Sano, Topological defects control collective dynamics in neural progenitor cell cultures. *Nature* **545,** 327–331 (2017).

[196] V. Schaller, C. Weber, C. Semmrich, E. Frey, and A. R. Bausch, Polar patterns of driven filaments. *Nature* **467,** 73–77 (2010).

[197] Y. Sumino *et al.*, Large-scale vortex lattice emerging from collectively moving microtubules. *Nature* **483,** 448–452 (2012).

[198] K. Kroy, D. Chakraborty, and F. Cichos, Hot microswimmers. *Eur. Phys. J. Spec. Top.* **225,** 2207–2225 (2016).

[199] S. Michelin and E. Lauga, Autophoretic locomotion from geometric asymmetry. *Eur. Phys. J. E* **38,** 7 (2015).

[200] S. Nalata *et al.*, Self-Rotation of a Camphor Scraping on Water: New Insight into the Old Problem. *Langmuir* **13,** 4454–4458 (1997).

[201] M. C. Marchetti *et al.*, Hydrodynamics of soft active matter. *Rev. Mod. Phys.* **85,** 1143–1189 (2013).

[202] M. Bär, R. Großmann, S. Heidenreich, and F. Peruani, Self-Propelled Rods: Insights and Perspectives for Active Matter. *Annu. Rev. Condens. Matter Phys.* **11,** 441–466 (2020).

[203] J. Toner and Y. Tu, Long-Range Order in a Two-Dimensional Dynamics XY model: How Birds Fly Together. *Phys. Rev. Lett.* **75,** 4326 (1995).

[204] J. Toner and Y. Tu, Flocks, herds, and schools: A quantitative theory of flocking. *Phys. Rev. E* **58,** 4828–4858 (1998).

[205] A. Souslov, B. C. van Zuiden, D. Bartolo, and V. Vitelli, Topological sound in active-liquid metamaterials. *Nat. Phys.* **13,** 1091-1094 (2017).

[206] K. Sone and Y. Ashida, Anomalous Topological Active Matter. *Phys. Rev. Lett.* **123,** 205502 (2019).

[207] S. Shankar, M. J. Bowick, and M. C. Marchetti, Topological Sound and Flocking on Curved Surfaces. *Phys. Rev. X* **7,** 031039 (2017).

[208] A. Souslov, K. Dasbiswas, M. Fruchart, S. Vaikuntanathan, and V. Vitelli, Topological Waves in Fluids with Odd Viscosity. *Phys. Rev. Lett.* **122,** 128001 (2019).

[209] K. Ohgushi, S. Murakami, and N. Nagaosa, Spin anisotropy and quantum Hall effect in the kagomé lattice: Chiral spin state based on a ferromagnet. *Phys. Rev. B* **62,** R6065 (2000).

[210] X. Yang, C. Ren, K. Cheng, and H. P. Zhang, Robust boundary flow in chiral active fluid. *Phys. Rev. E* **101,** 022603 (2020).

[211] L. Yamauchi, T. Hayata, M. Uwamichi, T. Ozawa, and K. Kawaguchi, Chirality-driven edge flow and non-Hermitian topology in active nematic cells. arXiv:2008.10852 (2020).

[212] L. S. Palacios *et al.*, Guided accumulation of active particles by topological design of a second-order skin effect. *Nat. Commun.* **12,** 4691 (2021).

[213] N. G. van Kampen, Stochastic Processes in Physics and Chemistry. Elsevier, New York, 1992.

[214] R. Bhatia, Matrix Analysis. Springer, New York, 1997.

[215] P. Diaconis, Proc. Natl. Acad. Sci. U.S.A. 93, 1659 (1996).

[216] D. A. Levin and Y. Peres, Markov Chains and Mixing Times (American Mathematical Society, 2009).

[217] T. Haga, M. Nakagawa, R. Hamazaki, and M. Ueda, *Phys. Rev. Lett.* **127,** 070402 (2021).

[218] T. Mori and T. Shirai, *Phys. Rev. Lett.* **125,** 230604 (2020).

[219] N. A. Sinitsyn and I. Nemenman, *EPL* **77,** 58001 (2007).

[220] E. Tang, J. Agudo-Canalejo, and R. Golestanian, Topology Protects Chiral Edge Currents in Stochastic Systems. *Phys. Rev. X* **11,** 031015 (2021).

[221] P. Mehta and J. Rocks, Thermodynamic origins of topological protection in nonequilibrium stochastic systems. arXiv:2206.07761 (2022).

[222] T. Yoshida and Y. Hatsugai, Bulk-edge correspondence of classical diffusion phenomena. *Sci. Rep.* **11,** 888 (2021).

[223] S. Makino, T. Fukui, T. Yoshida, and Y. Hatsugai, Edge states of a diffusion equation in one dimension: Rapid heat conduction to the heat bath. *Phys. Rev. E* **105,** 024137 (2022).

[224] H. Hu *et al.*, Observation of Topological Edge States in Thermal Diffusion. *Adv. Mater.* **34,** 2202257 (2022).

[225] M. Du *et al.*, Chiral edge waves in a dance-based human topological insulator. arXiv:2301.08356 (2023).

[226] T. Sugawara, M. Tachikawa, T. Tsukamoto, and T. Shimizu, Observation of synchronization in laser chaos. *Phys. Rev. Lett.* **72,** 3502–3505 (1994).

[227] J. P. Goedgebuer, L. Larger, and H. Porte, Optical Cryptosystem Based on Synchronization of Hyperchaos Generated by a Delayed Feedback Tunable Laser Diode. *Phys. Rev. Lett.* **80,** 2249–2252 (1998).

[228] G. Kozyreff, A. G. Vladimirov, and P. Mandel, Global Coupling with Time Delay in an Array of Semiconductor Lasers. *Phys. Rev. Lett.* **85,** 3809–3812 (2000).

[229] A. L. Hodgkin and A. F. Huxley, A quantitative description of membrane current and its application to conduction and excitation in nerve. *J. Physiol.* **117,** 500–544 (1952).

[230] H. Ulrichs, A. Mann, and U. Parlitz, Synchronization and chaotic dynamics of coupled mechanical metronomes. *Chaos* **19,** 043120 (2009).

[231] T. E. Lee and H. R. Sadeghpour, Quantum Synchronization of Quantum van der Pol Oscillators with Trapped Ions. *Phys. Rev. Lett.* **111,** 234101 (2013).

[232] A. W. Laskar *et al.*, Observation of Quantum Phase Synchronization in Spin-1 Atoms. *Phys. Rev. Lett.* **125,** 013601 (2020).

[233] J. Stuart, On the non-linear mechanics of wave disturbances in stable and unstable parallel flows Part 1. The basic behaviour in plane Poiseuille flow. *J. Fluid Mech.* **9,** 353–370 (1960).

[234] Y. Kuramoto, in: *International Symposium on on Mathematical Problems in Theoretical Physics, Lecture Notes in Physics,* Vol. 39 (ed. Araki, H.) 420 (Springer, New York, 1975).

[235] J. A. Acebrón, L. L. Bonilla, V. C. J. Pérez, Ritort, F., & Spigler, R. The Kuramoto model: A simple paradigm for synchronization phenomena. *Rev. Mod. Phys.* **77,** 137–185 (2005).

[236] B. Van der Pol, On "relaxation-oscillations". *Philos. Mag.* **2,** 978 (1926).

[237] P. Romanczuk, M. Bär, W. Ebeling, B. Lindner, and L. Schimansky-Geier, Active Brownian particles. *Eur. Phys. J. Spec. Top.* **202,** 1–162 (2012).

[238] R. Fitzhugh, Impulses and Physiological States in Theoretical Models of Nerve Membrane. *Biophys. J.* **1,** 445–466 (1961).

[239] J. Nagumo, S. Arimoto, and S. Yoshizawa, An Active Pulse Transmission Line Simulating Nerve Axon. *Proc. IRE* **50,** 2061-2070 (1962).

[240] F. Lederer, Discrete solitons in optics. *Phys. Rep.* **463,** 1–126 (2008).

[241] M. Wimmer *et al.*, Observation of optical solitons in PT-symmetric lattices. *Nat. Commun.* **6,** 7782 (2015).

[242] G. A. Swartzlander, D. R. Andersen, J. J. Regan, H. Yin, and A. E. Kaplan, Spatial dark-soliton stripes and grids in self-defocusing materials. *Phys. Rev. Lett.* **66,** 1583–1586 (1991).

[243] P.-W. Lo *et al.*, Topology in Nonlinear Mechanical Systems. *Phys. Rev. Lett.* **127,** 076802 (2021).

[244] B. G. Chen, N. Upadhyaya, and V. Vitelli, Nonlinear conduction via solitons in a topological mechanical insulator. *Proc. Natl. Acad. Sci. USA* **111,** 13004–13009 (2014).

[245] R. Rao and M. Esposito, Nonequilibrium Thermodynamics of Chemical Reaction Networks: Wisdom from Stochastic Thermodynamics. *Phys. Rev. X* **6,** 041064 (2016).

[246] K. Yoshimura and S. Ito, Thermodynamic Uncertainty Relation and Thermodynamic Speed Limit in Deterministic Chemical Reaction Networks. *Phys. Rev. Lett.* **127,** 160601 (2021).

[247] T. Okada and A. Mochizuki, Law of Localization in Chemical Reaction Networks. *Phys. Rev. Lett.* **117,** 048101 (2016).

[248] Y. Hirono, T. Okada, H. Miyazaki, and Y. Hidaka, Structural reduction of chemical reaction networks based on topology. *Phys. Rev. Research* **3,** 043123 (2021).

[249] S. H. Strogatz, *Nonlinear Dynamics and Chaos - With Applications to Physics, Biology, Chemistry and Engineering* Addison-Wesley, Reading, MA, 1994.

[250] M. W. Hirsch, S. Smale, R. L. Devaney, Differential Equations, Dynamical Systems, and an Introduction to Chaos. Academic Press, Cambridge 2012.

[251] D. Grobman, Homeomorphisms of systems of differential equations, *Dokl. Akad., Nauk.* **128,** 880–881(1959).

[252] P. Hartman, A Lemma in the theory of structural stability of differential equations, *Proc. Amer. Math. Soc.,* **11** 610–620 (1960).

[253] M. F. Atiyah and I. M. Singer, The Index of Elliptic Operators: I. *Ann. Math.* **87,** 484–530 (1968).

[254] C. Callias, Axial anomalies and index theorems on open spaces. *Commun. Math. Phys.* **62,** 213–234 (1978).

[255] I. Z. Kiss, Y. Zhai, and J. L. Hudson, Emerging Coherence in a Population of Chemical Oscillators. *Science* **296,** 1676–1678 (2002).

[256] H. Sakaguchi, S. Shinomoto, and Y. Kuramoto, Local and Grobal Self-Entrainments in Oscillator Lattices. *Prog. Theor. Phys.* **77,** 1005–1010 (1987).

[257] H. Hong, H. Park, and M. Y. Choi, Collective synchronization in spatially extended systems of coupled oscillators with random frequencies. *Phys. Rev. E* **72,** 036217 (2005).

[258] Y. Kuramoto and D. Battogtokh, Coexistence of Coherence and Incoherence in Nonlocally Coupled Phase Oscillators. *Nonlinear Phenom. Complex. Syst.* **5,** 380 (2002).

[259] D. M. Abrams and S. H. Strogatz, Chimera States for Coupled Oscillators. *Phys. Rev. Lett.* **93,** 174102 (2004).

[260] S. Shima and Y. Kuramoto, Rotating spiral waves with phase-randomized core in nonlocally coupled oscillators. *Phys. Rev. E* **69,** 036213 (2004).

[261] X. F. Wang and G. Chen, Synchronization in small-world dynamical networks. *Int. J. Bifurcat. Chaos* **12,** 187–192 (2002).

[262] M. Barahona and L. M. Pecora, Synchronization in Small-World Systems. *Phys. Rev. Lett.* **89,** 054101 (2002).

[263] C. Zhou and J. Kurths, Hierarchical synchronization in complex networks with heterogeneous degrees. *Chaos* **16,** 015104 (2006).

[264] L. M. Pecora, F. Sorrentino, A. M. Hagerstrom, R. E. Murphy, and R. Roy, Cluster synchronization and isolated desynchronization in complex networks with symmetries. *Nat. Commun.* **5,** 4079 (2014).

[265] Y. S. Cho, T. Nishikawa, and A. E. Motter, Stable Chimeras and Independently Synchronizable Clusters. *Phys. Rev. Lett.* **119,** 084101 (2017).

[266] M. J. Panaggio and D. M. Abrams, Chimera states: coexistence of coherence and incoherence in networks of coupled oscillators. *Nonlinearity* **28,** R67–R87 (2015).

[267] C. R. Laing, Chimeras in networks with purely local coupling. *Phys. Rev. E* **92,** 050904 (2015).

[268] M. G. Clerc, S. Coulibaly, M. A. Ferré, M. A. García-Ñustes, and R. G. Rojas, Chimera-type states induced by local coupling. *Phys. Rev. E* **93,** 052204 (2016).

[269] M. R. Tinsley, S. Nkomo, and K. Showalter, Chimera and phase-cluster states in populations of coupled chemical oscillators. *Nat. Phys.* **8,** 662–665 (2012).

[270] J. F. Totz, J. Rode, M. R. Tinsley, K. Showalter, and H. Engel, Spiral wave chimera states in large populations of coupled chemical oscillators. *Nat. Phys.* **14,** 282–285 (2018).

[271] A. M. Hagerstrom *et al.*, Experimental observation of chimeras in coupled-map lattices. *Nat. Phys.* **8,** 658–661 (2012).

[272] E. A. Martens, S. Thutupalli, A. Fourrière, and O. Hallatschek, Chimera states in mechanical oscillator networks. *Proc. Natl. Acad. Sci. USA* **110,** 10563–10567 (2013).

[273] S. Majhi, B. K. Bera, D. Ghosh, and M. Perc, Chimera states in neuronal networks: A review. *Phys. Life Rev.* **28,** 100–121 (2019).

[274] J. Sieber, O. E. Omel'chenko, and M. Wolfrum, Controlling Unstable Chaos: Stabilizing Chimera States by Feedback. *Phys. Rev. Lett.* **112,** 054102 (2014).

[275] T. Isele, J. Hizanidis, A. Provata, and P. Hövel, Controlling chimera states: The influence of excitable units. *Phys. Rev. E* **93,** 022217 (2016).

[276] Y. Zhang, Z. G. Nicolaou, J. D. Hart, R. Roy, and A. E. Motter, Critical Switching in Globally Attractive Chimeras. *Phys. Rev. X* **10,** 011044 (2020).

[277] J. -P. Eckmann, Roads to turbulence in dissipative dynamical systems. *Rev. Mod. Phys.* **53,** 643–654 (1981).

[278] M. Sano and K. Tamai, A universal transition to turbulence in channel flow. *Nat. Phys.* **12,** 249–253 (2016).

[279] V. Oseledets, A multiplicative ergodic theorem. Characteristic Ljapunov, exponents of dynamical systems. *Trans. Moscow. Math. Soc.* **19,** 197–231 (1968).

[280] F. Ginelli, *et al.*, Characterizing Dynamics with Covariant Lyapunov Vectors. *Phys. Rev. Lett.* **99,** 130601 (2007).

[281] F. Ginelli, H. Chaté, R. Livi, and A. Politi, Covariant Lyapunov vectors. *J. Phys. A* **46,** 254005 (2013).

[282] K. A. Takeuchi, F. Ginelli, and H. Chaté, Lyapunov Analysis Captures the Collective Dynamics of Large Chaotic Systems. *Phys. Rev. Lett.* **103,** 154103 (2009).

[283] J. L. Kaplan and J. A. Yorke, *in Functional Differential Equations and Approximation of Fixed Points*, Lecture Notes in Mathematics Vol. 730 (Springer-Verlag, Berlin, 1979), pp. 204–227.

[284] M. Wolfrum, O. E. Omel'chenko, S. Yanchuk, and Y. L. Maistrenko, Spectral properties of chimera states. *Chaos* **21,** 013112 (2011).

[285] M. Wolfrum and O. E. Omel'chenko, Chimera states are chaotic transients. *Phys. Rev. E* **84,** 015201 (2011).

[286] A. E. Botha, Characteristic distribution of finite-time Lyapunov exponents for chimera states. *Sci. Rep.* **6,** 29213 (2016).

[287] K. Höhlein, F. P. Kemeth, and K. Krischer, Lyapunov spectra and collective modes of chimera states in globally coupled Stuart-Landau oscillators. *Phys. Rev. E* **100,** 022217 (2019).

[288] I. Shimada and T. A. Nagashima, Numerical Approach to Ergodic Problem of Dissipative Dynamical Systems. *Prog. Theor. Phys.* **61,** 1605–1616 (1979).

[289] G. Benettin, L. Galgani, A. Giorgilli, and J. M. Strelcyn, Lyapunov Characteristic Exponents for smooth dynamical systems and for hamiltonian systems; a method for computing all of them. Part 1: Theory. *Meccanica* **15,** 9–20 (1980).

[290] J. -P. Eckmann and D. Ruelle, Ergodic theory of chaos and strange attractors. *Rev. Mod. Phys.* **57,** 617–656 (1985).

[291] D. J. Korteweg and G. de Vries, On the change of form of long waves advancing in a rectangular canal, and on a new type of long stationary waves. *Philos. Mag,* **39,** 422–443 (1895).

[292] N. Manton and P. Sutcliffe. Topological solitons. Cambridge University Press, Cambridge, 2004.

[293] R. Hirota, Exact Solution of the Sine-Gordon Equation for Multiple Collisions of Solitons. J. Phys. Soc. Japan **33,** 1459–1463 (1972).

[294] A. M. Turing, The chemical basis of morphogenesis. *Bull. Math. Biol.* **52,** 153–197 (1990).

[295] S. Kondo and R. Asai, A reaction-diffusion wave on the skin of the marine angelfish Pomacanthus. *Nature* **376** 765–768 (1995).

[296] F. Zangeneh-Nejad and R. Fleury, Nonlinear Second-Order Topological Insulators. *Phys. Rev. Lett.* **123,** 053902 (2019).

[297] D. Leykam, E. Smolina, A. Maluckov, S. Flach, and D. A. Smirnova, Probing Band Topology Using Modulational Instability. *Phys. Rev. Lett.* **126,** 073901 (2021).

[298] S. K. Ivanov, Y. V. Kartashov, L. J. Maczewsky, A. Szameit, and V. V. Konotop, Edge solitons in Lieb topological Floquet insulator. *Opt. Lett.* **45,** 1459–1462 (2020).

[299] S. Mukherjee and M. C. Rechtsman, Observation of Unidirectional Solitonlike Edge States in Nonlinear Floquet Topological Insulators. *Phys. Rev. X* **11,** 041057 (2021).

[300] R. Li, *et al.*, Topological bulk solitons in a nonlinear photonic Chern insulator. *Commun. Phys.* **5,** 275 (2022).

[301] M. Ezawa, Nonlinearity-induced chiral solitonlike edge states in Chern systems. *Phys. Rev. B* **106,** 195423 (2022).

[302] M. Jürgensen, S. Mukherjee, and M. C. Rechtsman, Quantized nonlinear Thouless pumping. *Nature* **596,** 63–67 (2021).

[303] Q. Fu, P. Wang, Y. V. Kartashov, V. V. Konotop, and F. Ye, Nonlinear Thouless Pumping: Solitons and Transport Breakdown. *Phys. Rev. Lett.* **128,** 154101 (2022).

[304] Q. Fu, P. Wang, Y. V. Kartashov, V. V. Konotop, and F. Ye, Two-dimensional nonlinear Thouless pumping of matter waves. *Phys. Rev. Lett.* **129.** 183901 (2022).

[305] M. Jürgensen and M. C. Rechtsman, Quantized nonlinear Thouless pumping. *Phys. Rev. Lett.* **128,** 113901 (2022).

[306] N. Mostaan, F. Grusdt, and N. Goldman, Quantized topological pumping of solitons in nonlinear photonics and ultracold atomic mixtures. *Nat. Commun.* **13,** 5997 (2022).

[307] M. Jürgensen, S. Mukherjee, C. Jörg, and M. C. Rechtsman, Quantized fractional Thouless pumping of solitons. *Nat. Phys.* **19,** 420–426 (2023).

[308] T. Tuloup, R. W. Bomantara, and J. Gong, Breakdown of quantization in nonlinear Thouless pumping. *New J. Phys,* **25,** 083048 (2023).

[309] D. C. Tsui, H. L. Stormer, and A. C. Gossard, Two-dimensional magnetotransport in the extreme quantum limit. *Phys. Rev. Lett.* **48,** 1559–1562 (1982).

[310] K. I. Bolotin, F. Ghahari, M. D. Shulman, H. L. Stormer, and P. Kim, Observation of the fractional quantum Hall effect in graphene. *Nature* **462,** 196–199 (2009).

[311] A. Darabi, and M. J. Leamy, Tunable Nonlinear Topological Insulator for Acoustic Waves. *Phys. Rev. Appl.* **12,** 044030 (2019).

[312] L. J. Maczewsky, *et al.*, Nonlinearity-induced photonic topological insulator. *Science* **370,** 701–704 (2020).

[313] M. Ezawa, Nonlinearity-induced transition in the nonlinear Su-Schrieffer-Heeger model and a nonlinear higher-order topological system. *Phys. Rev. B* **104,** 235420 (2021).

[314] K. Mochizuki, K. Mizuta, and N. Kawakami, Fate of topological edge states in disordered periodically driven nonlinear systems. *Phys. Rev. Res.* **3,** 043112 (2021).

[315] R. W. Bomantara, W. Zhao, L. Zhou, and J. Gong, Nonlinear Dirac cones. *Phys. Rev. B* **96,** 121406 (2017).

[316] F. Li, J. Wang, D. Cui, K. Xue, and X. X. Yi, Bloch band structures and linear response theory of nonlinear systems. arXiv:2210.13776 (2022).

[317] C. W. Wächtler and G. Platero, Topological synchronization of quantum van der Pol oscillators. *Phys. Rev. Res.* **5,** 023021 (2023).

[318] C. Yuce, Nonlinear non-Hermitian skin effect. *Phys. Lett. A* **408,** 127484 (2021).

[319] M. Ezawa, Dynamical nonlinear higher-order non-Hermitian skin effects and topological trap-skin phase. *Phys. Rev. B* **105,** 125421 (2022).

[320] B. Zhu *et al.*, Anomalous Single-Mode Lasing Induced by Nonlinearity and the Non-Hermitian Skin Effect. *Phys. Rev. Lett.* **129,** 013903 (2022).

[321] R. Shindou, R. Matsumoto, S. Murakami, and J. Ohe, Topological chiral magnonic edge mode in a magnonic crystal. *Phys. Rev. B* **87,** 174427 (2013).

[322] T. Isobe, T. Yoshida, and Y. Hatsugai, Topological band theory of a generalized eigenvalue problem with Hermitian matrices: Symmetry-protected exceptional rings with emergent symmetry. *Phys. Rev. B* **104,** L121105 (2021).

[323] V. Kuzmiak, A. A. Maradudin, and F. Pincemin, Photonic band structures of two-dimensional systems containing metallic components. *Phys. Rev. B* **50,** 16835 (1994).

[324] H. Huang, C. Sun, and G. Huang, On the negative effective mass density in acoustic metamaterials. *International Journal of Engineering Science* **47,** 610 (2009).

[325] T. Isobe, T. Yoshida, and Y. Hatsugai, Bulk-edge correspondence for nonlinear eigenvalue problems. arXiv:2310.12577 (2023).

[326] S. Cheng, Y. Jiang, and G. Xianlong, Bulk-edge correspondence for the nonlinear eigenvalues problem of the Haldane model. arXiv:2311.14229 (2023).

[327] K. Sone, Y. Ashida, and T. Sagawa, Topological synchronization of coupled nonlinear oscillators. *Phys. Rev. Research* **4,** 023211 (2022).

[328] B. I. Shraiman, A. Pumir, W. van Saarloos, P. C. Hohenberg, H. Chaté, and M. Holen, Spatiotemporal chaos in the one dimensional complex Ginzburg-Landau equation, *Physica D* **57,** 241 (1992).

[329] H. Zhao *et al.*, Non-Hermitian topological light steering. *Science* **365,** 1163–1166 (2019).

[330] B. B. Johnson, S. V. Dhople, and A. O. Hamadeh, and P. T. Krein, Synchronization of Parallel Single-Phase Inverters With Virtual Oscillator Control. *IEEE Trans. Circuits Syst. I Regul. Pap.* **61,** 834-844 (2014).

[331] K. Sone, M. Ezawa, Y. Ashida, N. Yoshioka, and T. Sagawa, Nonlinearity-induced topological phase transition characterized by the nonlinear Chern number. arXiv:2307.16827 (2023).

[332] T. Fukui, Y. Hatsugai, and H. Suzuki, Chern Numbers in Discretized Brillouin Zone: Efficient Method of Computing (Spin) Hall Conductances. *J. Phys. Soc. of Jpn.* **74,** 1674–1677 (2005).

[333] K. G. Wilson, Confinement of quarks. *Phys. Rev. D* **10,** 2445–2459 (1974).

[334] K. G. Wilson, Quarks and Strings on a Lattice, Springer, Boston, MA, 1977.

[335] R. Fletcher, Practical methods of optimization. John Wiley and Sons, New York, 1987.

[336] C. Broyden, A class of methods for solving nonlinear simultaneous equations. *Math. Comput.* **19,** 577–593 (1965).

[337] K. Sone, M. Ezawa, Z. Gong, T. Sawada, N. Yoshioka, and T. Sagawa Transition from Topological to Chaos in the Nonlinear Su-Schrieffer-Heeger Model. in preparation.

[338] T. D. Rogers and D. C. Whitley, Chaos in the cubic mapping. *Mathematical Modelling* **4,** 9 (1983).

[339] H. Skjolding, B. Branner-Jørgensen, P. L. Christiansen, and H. E. Jensen, Bifurcations in Discrete Dynamical Systems with Cubic Maps. *SIAM Journal on Applied Mathematics* **43,** 520 (1983).

[340] M. Maffei, A. Dauphin, F. Cardano, M. Lewenstein, and P. Massignan, Topological characterization of chiral models through their long time dynamics. *New J. Phys.* **20,** 013023 (2018).

[341] B. Perez-Gonźalez, M. Bello, A. Gómez-León, and G. Platero, Interplay between long-range hopping and disorder in topological systems. *Phys. Rev. B* **99,** 035146 (2019).

[342] H.-C. Hsu and T.-W. Chen, Topological Anderson insulating phases in the long-range Su-Schrieffer-Heeger model. *Phys. Rev. B* **102,** 205425 (2020).

[343] K. Sone, Y. Ashida, and T. Sagawa, Exceptional mode topological surface laser. *Phys. Rev. B* **105,** 235426 (2022).

[344] Y. Xu, S.-T. Wang, and L.-M. Duan, Weyl Exceptional Rings in a Three-Dimensional Dissipative Cold Atomic Gas. *Phys. Rev. Lett.* **118,** 045701 (2017).

[345] C. W. Wächtler, V. M. Bastidas, G. Schaller, and W. J. Munro, Dissipative nonequilibrium synchronization of topological edge states via self-oscillation, Phys. Rev. B 102, 014309 (2020).

[346] J. C. Eilbeck, P. S. Lomdahl, and A. C. Scott, The discrete self-trapping equation. *Physica D* **16,** 318-338 (1985).